Charge state manipulation of silicon-based donor spin qubits



Roberto Lo Nardo

Mansfield College

A thesis submitted for the degree of Doctor of Philosophy

at the University of Oxford

Hilary Term 2015

Charge state manipulation of silicon-based donor spin qubits

Roberto Lo Nardo
Mansfield College
Hilary Term 2015

Abstract of a thesis submitted for the degree of Doctor of Philosophy

Spin properties of donor impurities in silicon have been investigated by electron spin resonance (ESR) techniques for more than sixty years. These studies gave us a contribution towards understanding some of the physics of doped semiconductor materials in general, which is the platform for much of our current technology. Despite the fact that donor electron and nuclear spins have been researched for so long, ESR studies of their properties are still giving us interesting insights. With the introduction of the concept of quantum information in the 1980s, some properties of donor spins in silicon, that were known from the fifties (such as long relaxations), have been reinterpreted for their potential application in this field. Since then, incredible experimental results have been achieved with magnetic resonance control, including manipulation and read-out of individual spins. However, some open questions are still to be answered before the realisation of a spin-based silicon quantum architecture will be achieved. Currently, ESR studies still contribute to help answering some of those questions. In this thesis, we demonstrate electrical and optical methods for donor charge state manipulation measured by ESR. Recent experiments have demonstrated that coherence time of nuclear spins may be enhanced by manipulating the state of donors from neutral to singly charged. We investigate electric field ionisation/neutralisation of arsenic donors in a silicon SOI device measured by ESR. Below ionisation threshold, we also measure the hyperfine Stark shift of arsenic donors spins in silicon. These results have, for instance, implications on how fast individual addressability of donor spins may be achieved in certain quantum computer architectures. Here, we also study optical-driven charge state manipulation of selenium impurities in silicon. Selenium has two additional electrons when it replaces an atom in the silicon crystal (i.e. double donor). The electronic properties of singly-ionised selenium make it potentially advantageous as spin qubit, compared to the more commonly studied group-V donors. For instance, we find here that the electron spin relaxation and coherence times of selenium are up to two orders of magnitude longer than phosphorus at the same temperature. Finally, we demonstrate that it is possible to bring selenium impurity in singly-charged state and subsequently re-neutralise them leaving a potential long-lived ^{77}Se nuclear spin.

Acknowledgements

When I look back at the last three years of my life, I see a *long* journey that I made it through only thanks to a lot of people. First, I would like to express my gratitude to my supervisors John Morton and Simon Benjamin. In particular, the understanding and support that I have received from John Morton has been far beyond his academic duties. I would thank Volker Lang, Stefanie Simmons and Cheuk Lo for inspiring and teaching me most of the technical skills I have learned. I am also very grateful to every one else in the group, Gary Wolfowicz, Anasua Chatterjee, John Mansir, Salahuddin Nur, Philipp Ross, Naitik Panjwani, Jarrid Pla and Matias Urdampilleta for bearing me for all this time. A particular thanks goes to Gary Wolfowicz, with whom I spent the most time in the lab and has been the most *patient* with me. I also would like to thank all the people I have been working with. Christopher Kay and Enrico Salvatori have been a great company in the F10 lab for so many hours. I also thank Joseph Smith for spending a few weekends measuring ESR spectra with me. Finally, I would like to express my gratitude to all collaborators of these years: Thomas Schenkel, Stephen Lyon, Alexei Tyryshkin and Mike Thewalt.

Contents

Abstract i

Acknowledgements iii

1. Introduction 1

2. Silicon-based spin quantum computers 7
2.1. Donor spins as qubits 8
2.2. Relaxation of donor spins 11
2.3. Towards donor spin quantum computers 14
2.4. Conclusions 21

3. Donor electron spins in silicon 23
3.1. Electronic levels 25
3.2. Population of electronic levels in thermal equilibrium 32
3.3. Electron and nuclear spin Hamiltonian 40
3.4. Stark shift of donors in silicon 46
3.5. Electron spin relaxation and decoherence 50

4. Electron spin resonance 55
4.1. The phenomenon of spin resonance 56
4.2. Time evolution of a spin system 58
4.3. Measurement of spin relaxation and coherence 61
4.4. ESR setup 64

5. Electric field ionisation and Stark Shift of arsenic donors 67
5.1. Materials and characterisation 69

5.2. Stark shift of resonance frequency 78
5.3. Electric field induced donor ionisation and neutralisation 82
5.4. Conclusions 88

6. Spin relaxation of selenium donors in silicon 89
6.1. Materials characterisation 91
6.2. Electron spin relaxation 104
6.3. Electron spin coherence 108
6.4. Nuclear spin coherence 110
6.5. Conclusions 114

7. Optical charge state manipulation in selenium doped silicon 115
7.1. DA recombination dynamics in compensated selenium doped silicon . 117
7.2. Materials and methods 119
7.3. A spin echo study of DA recombination dynamics 122
7.4. Conclusions 130

8. Conclusions 131

A. The rotating frame 135

B. Theory of DA recombination dynamics in selenium doped silicon 139

Bibliography 145

CHAPTER 1

Introduction

Research in quantum information and computation aims to realise a new computational architecture that encodes and processes information using quantum two-level systems, namely *qubits* [DiV95]. The importance this technology is to introduce a new and more powerful platform for computation that differs on a fundamental level from our current technology. The advantage of quantum computation was already identified in the early eighties [Deu85] and since then, properties of different physical systems have been explored for their potential applications as hardware for this *new* technology [LJL+10].

In the last twenty-five years, there has been a remarkable advance in the experimental development of quantum mechanical systems that exploit different degrees

of freedom as qubits. Among them, electron and nuclear spins of donor impurities in silicon have been extensively studied with incredibly promising results [MMEL11, ABD+13].

For instance, manipulation and control of individual spins has been already achieved by integrating donors into nanoelectronic devices [MPZ+10, PTD+12, PTD+13] and spin coherence as long as seconds for electrons [WTG+13] and hours for nuclei [SSS+13] has been demonstrated. However, a number of scientific challenges are still to be solved for the application of such technology into a scalable quantum computer, such as demonstrating the interaction between spin qubits, local-addressability and long-lived storage of quantum information.

At present, extensive research attention focuses on understanding the basic physics related to those technological challenges. The work of this thesis aims to give a contribution towards this direction exploring different approaches for controlling the charge state of donors, using optical and electrical methods. Manipulation of the charge state of donors in silicon has been identified as a strategy for controlling interaction between qubits [KMD+00] and it has been already used to enhance nuclear spin coherence by suppressing the hyperfine interaction between the donor electron and nuclear spins [SSS+13, DHSB12].

The natural interaction between electron and nuclear spins is one of key advantages of donor-based spin quantum information and allows one to exploit their complementary proprieties. Nuclear spins have very long coherence times (*hours*) because of their strong isolation from the environment but they are also difficult to control. Electron spins can be easily manipulated but their relaxation time is usually shorter (*seconds*). On the other hand, the hyperfine interaction provides a way for the nuclear spin to couple more strongly to its environment which results in a reduction

of its coherence time [DHSB12].

Recent experiments have demonstrated that nuclear spin coherence can be enhanced by removing the hyperfine interaction with electron spin by placing the donor in a singly charged state (D^+) [DHSB12]. The nuclear spin coherence of ionised phosphorus donors can be very long even at room-temperature but its measurement and initialisation require the interaction with electron spins and are limited to cryogenic temperatures [SSS+13].

In this thesis, we investigate two strategies for donor charge state manipulation. The first is the application of an electric field for donor ionisation. The electric field has been suggested for donor ionisation and local addressability of individual impurities since the Kane proposal in 1998 [Kan98]. Here, we study the effect of electric field on arsenic donors in a Si-SOI device designed for electron spin resonance measurements.

The second method is the optical illumination of selenium impurities in silicon. Chalcogen impurities (S, Se, Te) in silicon are *deep* double donors and therefore they have three available states: D^0, D^+ and D^{++}. Neutral selenium, for instance, has two bound electrons and forms a spin-singlet ground state with a binding energy of 307 meV. Singly-ionised selenium, has one unpaired electron, has an ionisation energy of 593 meV and is thermally ionised only above $\sim$ 300 K [GJL82]. Because the ionisation energies of selenium impurities are much larger with respect to shallow donors, optical sources at the corresponding frequencies ($\sim 2-5$ μm) are already commercially available making attractive the optical charge control of deep donors.

This thesis is structured as follows:

Chapter 2 introduces the field of silicon-based spin quantum computers. In particu-

lar, we describe the key ideas and advantages behind the application of donor spins as qubits and the technological requirements for the realisation of such architectures. We also underline the main experimental results pointing out their scientific importance as well as the challenges that still remain open.

Chapter 3 reviews the theoretical background of donor spins in silicon. In this Chapter we discuss the electronic proprieties of donors and their charge state at thermal equilibrium derived from Fermi-Dirac statistics. Moreover, we review the theory of donor electron and nuclear spins, including the solution of their spin Hamiltonian and the contributions to relaxation and decoherence.

Chapter 4 describes the basic principals of electron spin resonance (ESR). In particular, we introduce the physical phenomena of spin resonance, ESR experimental techniques and the instrumentation used in this thesis.

Chapter 5 exploits electric-field induced ionisation as a strategy for controlling the charge state of arsenic donors in 28-silicon. We develop parallel-plate capacitor-like devices for the application of a uniform electric field. Our device geometry allows us to demonstrate the electric field induced ionisation-recombination of donors measured by electron spin resonance. By applying an electric field below the ionisation threshold, we also measure the Stark shift of the donor spin resonance frequency.

Chapter 6 introduces the proprieties of selenium impurities in silicon and the electron spin resonance characterisation of the samples used in following Chapters. Here we also report the timescale of electron and nuclear spin relaxation (T_1) and decoherence (T_2) and their mechanisms. We find that the electron spin relaxation of selenium can be up two order of magnitude longer then phosphorus at a given temperature.

Chapter 7 investigates the effect of optical illumination on selenium impurities as a

strategy for controlling their charge state. Illuminating the sample with above band gap illumination we generate non-equilibrium charge states of the donors and the acceptors that is found to be as long as *minutes*, demonstrating a mechanism for placing the donor in the neutral state. Finally, we demonstrate that the thermal equilibrium charge state can be reached faster by selectively ionising the neutral impurities by optical means.

CHAPTER 2

Silicon-based spin quantum computers

Manipulation and control of qubits, while preserving at all time their quantum coherence are some of the key requirements for the realisation of a quantum computer architecture. This Chapter is dedicated to introduce those requirements together with the different scientific and technological challenges related to fulfil them.

In particular, we focus on electron and nuclear spins in silicon, underlining their main advantages that make them suitable as qubits and the main experimental results obtained integrating them into electronic devices. For instance, we discuss spin relaxation times, single-spin control and read-out. Special attention is also paid to those aspects that still remain open, such as scalability and interaction of qubits and those that are related to the manipulation of charge state of donors.

2.1. Donor spins as qubits

The first basic requirement for the realisation of a quantum computer is a quantum two-level system with a coherence time which is long compared to its evolution time. Therefore, relaxation and coherence properties of different physical systems have been extensively investigated to identify potential candidates as qubit. Among them, the spin of electrons and nuclei of different paramagnetic elements and molecules is a quantum degree of freedom that provides a natural quantum system particularly suitable for qubits.

Since the beginning of the research in quantum information, a large spectrum of different spin systems has been explored for such applications. For instance, studies have been included quantum dots in semiconductor materials [NKNV07], donors in silicon [MTB$^+$08], crystal defects such as nitrogen vacancies in diamonds [HSM06] and molecules and atoms incarcerated in C_{60} fullerenes that have unpaired electrons [BAB$^+$06, MTA$^+$05b]. The spins of all these different physical systems exhibit a coherence time ($\sim 10^{-6} - 1$ s) much longer than the manipulation time ($\sim 10^{-9}$ s).

Preserving the coherence of a qubit state is indeed one of the most important requirements for all application in quantum information. However, any real quantum system is affected by interactions with its environment. These interactions affect the state of the system producing fluctuations that have to be avoided to perform a quantum computational algorithm without errors.

A quantum state can be corrupted in two different ways. The first one relates to fluctuation of the energy of the system and involves a transition between two different eigenstates of the Hamiltonian. For a spin under a magnetic field, this fluctuation

corresponds to a random transition from the up to the down state or *vice versa*. This process is characterised by the so called *population relaxation* time (T_1) which gives the time-scale of the relaxation into thermal equilibrium. The second process involves only transitions between states within the same energy and is described by the *decoherence* time, T_2.

The second basic requirement of a quantum computer involves the ability to perform qubit operations to manipulate the state of the qubit. In principle, this implies the control of the system via unitary evolution from any initial state to any final state. The evolution of an electron spin, under a static magnetic field, can be controlled by driving eigenstate transitions by the application of resonant microwave fields.

The control of the spin dynamics via microwaves is the basis of the well known Electron Spin Resonance (ESR) technique [GB58]. In ESR, single-qubit operations can be achieved by applying an appropriate sequence of microwave pulses. Different electron spin systems have demonstrated that single-qubit operations using pulsed-ESR can be performed with high fidelity [MTA$^+$05a] thanks to *long* lifetimes [TTM$^+$12] and *fast* manipulation [FDT$^+$09].

The main advantage of electron and nuclear spins of donor impurities in silicon, with respect to other spin systems, is the ability to integrate them into silicon-based electronic devices to control and read out their quantum state. Using this approach, remarkable experimental results have been achieved in the last fifteen years, as will be discussed in the following Sections.

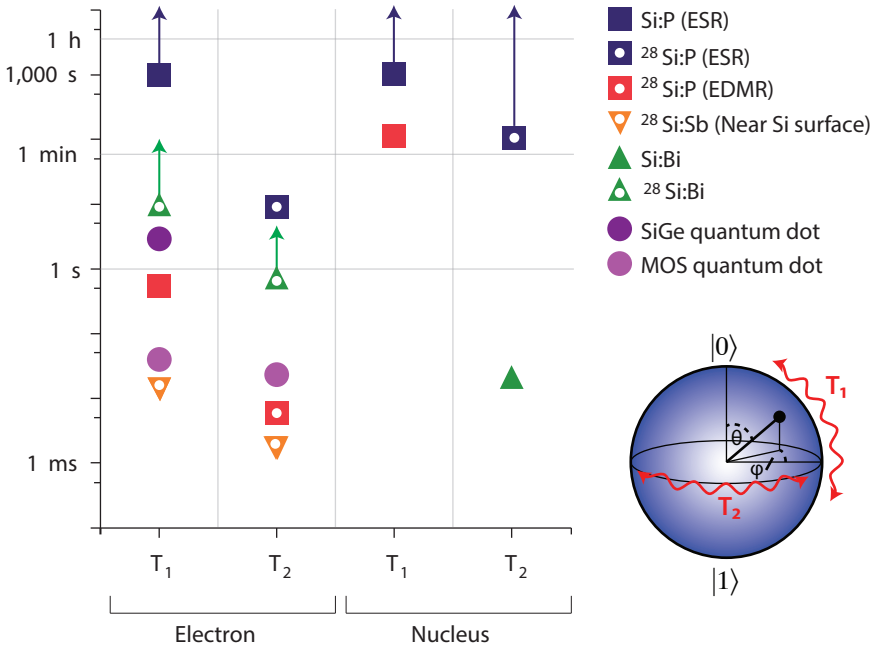


Figure 2.1.: **Information lifetimes for various spins in silicon.** This Figure summarises the experimental results for T_1 and T_2 of electron spins of donors in silicon and of silicon-based quantum dots. In the case of donor-bound electron spins, the relaxation times of the donor nuclear spin can also be extracted. Unless otherwise indicated, natural silicon (with $\sim$ 5% ^{29}Si) was used. The arrows indicate that these times become even longer at lower temperatures. From the top to bottom of the graph, electron T_1 data are taken from refs [Feh59], [WST$^+$12a], [SPV$^+$11], [MEH$^+$09], [GWR$^+$10] and [MWS$^+$10], [XHJ10], and [SLP$^+$06]; electron T2 data from refs [MDL$^+$14], [WTG$^+$13], [TLAR03], [WST$^+$12a], [SLP$^+$06] and [MMS$^+$08]; nuclear T_1 data from refs [Feh59] and [MVMB10]; and nuclear T2 data from ref [SSS$^+$13], [SST$^+$12] and ref [GWR$^+$10]. Modified and updated from [MMEL11].

2.2. Relaxation of donor spins

The relaxation properties of donor spins in silicon have been studied by ESR for more than fifty years, well before the introduction of the concept of quantum information. For instance, the introduction of the electron spin echo technique using microwave pulses, by Gordon and Bowers in 1958, allowed the first measurement of the T_2 of the electron spins bound to donors and opened a large research field of coherent control of spins in the solid state.

After the introduction of quantum information theory, ESR techniques were reinterpreted for quantum computation control of spin qubits. Since then, several different donor systems in silicon have been investigated for quantum information applications, such as phosphorous [MTB$^+$08], arsenic [LLG$^+$11], antimony [LBS$^+$07] and bismuth [GWR$^+$10, WST$^+$12a].

The electron spin relaxation time of donor electron spins in silicon was also measured in the fifties and it can be of the order of hours at low temperature [Feh59]. Since then, the mechanisms of relaxation of donor spins have been investigated and are considered to be well known [Orb61, Cas67]. The different processes of spin relaxation are also a fundamental limit for the electron spin coherence time, T_2 [Feh59, MTB$^+$08]. However at *low* temperature, T_1 becomes much longer than T_2 and other decoherence mechanisms become more important [GB58]. One of these mechanisms in natural silicon involves the presence of ^{29}Si isotopes: the nuclear spins of ^{29}Si produce magnetic field fluctuations which interact with the donor electron spins [TLAR03].

Recently, by reducing the ^{29}Si concentration down to 50 ppm, donor electron spin T_2 of the order of a second has been achieved for phosphorus [TTM$^+$12] and for bis-

muth [WST+12a]. In these experiments, the development of ^{28}Si isotopic enrichment techniques [AAB+11], providing an environment free of nuclear spins from the ^{29}Si, contributed to suppress the mechanisms that limit the electron decoherence. In this case, the interaction between different donor electron spins becomes the dominat decoherence mechanism.

One of the advantages of using donor spins for quantum information is the ability to use the hyperfine interaction to the donor nuclear spin. For instance, Electron Nuclear DOuble Resonance (ENDOR) techniques, based on the manipulation of nuclear and electron spins, have been used to study phosphorus donors in isotopic enriched ^{28}Si. Using these techniques, a nuclear spin-based quantum memory [MTB+08] and the generation of entanglement between an ensemble of electron and nuclear spins [SBR+11] have been demonstrated.

The nuclear spin coherence times of donors in silicon are much longer than those of the electron spins and are mainly limited by the hyperfine interaction between the electron and the nuclear spins [MTB+08]. By removing this hyperfine interaction, the coherence time of the nuclear spin may be enhanced – this has been recently achieved by ionising the donors by optical illumination [DHSB12]. Optical manipulation of the donor charge state combined with ESR techniques has therefore been demonstrated to be an advantageous technique to improve the nuclear spin coherence.

Optical illumination has been also used to read-out electron-nuclear spin states by exciting hyperfine split donor-bound exciton (D^0X) transitions, under an external magnetic field [YSK+06]. In 28-silicon, the linewidth of the different hyperfine D^0X transitions becomes so narrow that, using tuneable single-frequencies lasers, it is possible to selectively excite a specific transition [KTR+01].

Donor ionisation performed selectively on a given hyperfine state with single-frequency illumination at one of the D^0X transitions has also enabled the hyperpolarisation of phosphorous in silicon [YSS+09]. Optically detected nuclear magnetic resonance (NMR) of hyperpolarised phosphorous has been measured, by combining this technique with radio-frequency pulses [SSY+11].

More recently, a nuclear spin coherence time of 39 minutes has been measured at room-temperature by combining electron spin resonance and D^0X optical hyperpolarisation. These results suggested that nuclear spin-based quantum information has the potential for high-temperature operation [SSS+13] – though spin read-out and initialisation still require cryogenic temperature.

Although different ionisation strategies have demonstrated that the nuclear spin coherence is enhanced by removing the hyperfine interaction, it is still not clear how this can be exploited for quantum information applications. The read-out of nuclear spins, based on the ionisation methods described above, only allows one to measure the nuclear spin in one of the eigenstates.

Moreover, thermal and optical ionisation methods demonstrated so far, imply a random modulation of the hyperfine interaction between electron and nuclear spins that may produce decoherence. This happens if ionisation times are slower than those of the electron-nucleus spin interactions.

2.3. Towards donor spin quantum computers

The ability to address individual spins is another key requirement towards the fabrication of a scalable qubit architecture. The integration of single donor spins into electronic devices, that control and read them out, has been suggested as a strategy to fulfil individual addressability since the 1990s [Kan98, SDK03, Mor09, SLW+11].

The first proposal for a spin-based quantum computer in silicon, based on this approach, was made by Kane in 1998 who introduced the idea of an integrated device able to electronically control the quantum state of electron and nuclear spins of donors in silicon [Kan98].

In Kane's design, donor atoms are individually implanted in precise positions forming an array of quantum bits. Electrical gates are then used to initialise, control and read out the nuclear spins. The control of the hyperfine interaction by local electric fields is used to address an individual donor and the nuclear spin state is read by electron tunnelling into single electron transistors.

The electron spin relaxation and coherence times are shorter than those of the nuclear spins but they can still exist in coherent states long enough to make spin state manipulation and donor-donor interactions possible. Finally, the control of the electron-electron spin interaction is ideally tuned by varying the voltage applied to a gate in between the donors and by modifying the overlapping of the electronic wave function. As a result, the exchange-coupling interaction is tuned.

The realisation of this architecture relies on overcoming several key challenges: (1) The position of donor impurities requires atomic scale precision. The strength of the exchange coupling between the donors is very sensitive to the error in the donor position and the atomic scale positioning techniques available so far have low con-

sistency. (2) The control of the electron-nuclear spin interaction based on the application of electric field still needs to be fully explored. Even though this effect has been recently demonstrated, it is still not clear whether a strong enough shift in the transition frequency can be achieved before donor ionisation. (3) Reliable read-out of individual electron and nuclear spin as well as long-lived memories are essential. (4) Scalability and multi-quibit interaction strategies are still to be explored. Each of these four issues is discussed in more detail below.

Fabrication of single dopant devices

The fabrication of a Kane-like architecture, as described above, relies on positioning single dopants in a well-defined array. Ion implantation, the most common technique used for doping in the silicon industry is also, so far, the more explored method for the fabrication of single donor devices.

The implantation of donors at a single ion level requires high positional accuracy and a way to verify the occurrence of single-ion placement. In order to control the ion position on a 10 nm scale, several groups have, for instance, demonstrated the use of nano-scale apertures in photoresist [TCM+10].

In reference [TCM+10], the implantation of a single phosphorus donor in silicon was observed in planar nanoscale FET structures, demonstrating resonant tunnelling of electrons via the discrete donor states. The detection of single-ion placement has also been demonstrated by several methods. For example, detection of secondary electrons from highly charged ions [SPP+03] and charge detection from photodiodes [JYH+05, SBCC08] have been used.

The ability to implant single atoms into silicon devices has stimulated much re-

search in the field of single dopant transport in nano-MOSFET structures [TCM+10, TML+10]. Several groups have demonstrated transport through single dopant in three terminal configurations. In more recent years, this has been extended to two-gate devices fabricated in ^{28}Si [LPD+09, RDFV+12].

For instance, in reference [RDFV+12] the sequential transport through two phosphorus donors in a silicon nano-wire has proven the possibility to electrically control the transport through isolated donors in a nano-electronic device.

Transport measurements through a single donor atom in the channel of a silicon finFET have been also studied to determine the effect of the gate voltage on the orbital spectra of the donor [LRW+08]. They analysed the effect of the electrical field of the FET gate on the transport spectroscopy, comparing the results with an atomistic model with a good agreement.

In the last few years, research in the field of single donor implantation for applications in quantum information and in single-atom electronics has been rapidly growing, showing very promising results [FMZ+10, FMM+12]. Even though ion implantation has reported a large number of interesting results in the fabrication of single dopant devices, the precision of the dopant position is still on the order of 10 nm and it is not enough for the requirement of the fabrication of a scalable silicon based quantum architecture.

An alternative approach to place single dopant in crystalline silicon with atomic precision involves the use of a lithographic technique and a scanning probe microscope. Using this technique, the fabrication of a single phosphorus atom transistor has been recently demonstrated [FMM+12]. A single-atom transistor was fabricated with a single phosphorus atom positioned between highly doped source and drain leads with a lateral spatial accuracy of ± 1 atomic lattice spacing. Moreover, the

observation of individual donor controlled transitions for 0, 1 and 2 electron states of the donor has been demonstrated.

This lithographic technique is based on depositing a monolayer of hydrogen resist patterned by using the tip of a Scanning Tunnelling Microscopy (STM) [LSH+94]. This was adapted for the fabrication of the first in-plane silicon device with atomic scale precision [ROS+04, ROG+05]. The advantage of this technique, over the usual CMOS technology, is that these devices do not contain interfaces of different materials (such as the ones between silicon and silicon oxide) strongly reducing the effect of defects and electron traps.

In more complicated structures, the same technique has been used to confine electrons in an in-plane quantum dot [FMZ+10]. In their device, the sub-10-nm lateral confinement is provided by step change in the dopant concentration, giving a rise to a very small energy level separation of the order of 100 μeV.

The results on crystalline silicon devices, described above, highlight the considerable advantages of these systems compared to MOS techniques. For example, the absence of any nearby interfaces reduces electric-field fluctuations due to interface-charge trapping [FMM+12]. However, their fabrication procedure is still very time consuming, not easily scalable and it is not very clear how this technique could be used to place different donor species in the same device.

Controlling the electron-nuclear spin interaction by the Stark effect

One of the central requirements for the realisation of certain quantum architectures is the individual addressability of donor spins. In Kane's proposal, individual *one-*

qubit operations are performed on a specific donor by tuning its resonance frequency under the application of a local electric field [Kan98].

The electric field is controlled by a local metal gate on the surface, called an *A gate*. Under an electric field, the donor electron wavefunction is modified by pulling the electron away from the nuclear site with a consequent reduction of the hyperfine interaction. This effect, so called *Stark shift*, may allow individual control of the donors resonance frequency *in situ*.

Since Kane's proposal, the hyperfine Stark shift has been calculated theoretically. In the earliest studies, the problem was analysed with perturbation theory using a hydrogenic wavefunction [LFKV00]. Using tight-binding theory, a more precise description of the Stark shift of the hyperfine interaction was obtained [MBKK05, MCK04]. More recently, more accurate modelling of the effect has been performed by a multivalley effective mass theory approach [PWU$^+$14].

The first experimental demonstration of a Stark shift of the resonance frequency measured by ESR in an integrated device was reported in 2006 [BTS$^+$06]. In this experiment, the electrostatic tuning of the spin resonance of electrons bound to antimony donors in silicon was measured using electron spin echo sequences.

Experimental results on the Stark shift resolved a quadratic hyperfine and electron g-factor dependence on the external electric field measured as a phase shift during the spin echo experiment. A maximum hyperfine Stark shift of 25 kHz was found under the application of an electric field of about 0.1 V/μm. This results were compared to theoretical calculations in the same regime using the tight-binding and the band minima basis approaches [RWB$^+$07]. The theoretical results of the simulation of both methods were consistent with the experimental data of Si:Sb.

In the experiment described above, the electric field was applied by interdigitated metal contacts and, due to this geometry, the donor felt a non-uniform field distribution. Moreover, the Stark shift effect has only been measured for antimony impurities so far and it is not clear yet what is the maximum shift obtainable, before inducing electric field ionisation. It is therefore desirable to further investigate the Stark shift for other donor impurities in silicon under a more uniform applied electric field.

Finally, the application of large uniform electric field may in principle allow the study of the proprieties of ionised impurities achieved with a controllable donor ionisation and subsequent neutralisation.

Read-out of electron spins

The read-out of a single donor spin is an essential requirement for the implementation of a quantum architecture and involves precise measurements of qubit states. Electron spins in donors and quantum dots have a very *small* magnetic moment which is hard to detect at a single level. In order to overcome this limitation, a possible approach is to convert the spin state into a different physical propriety, such as charges [EHvB$^+$04] or optical photons.

Read-out techniques based on the spin-to-charge conversion mechanism may allow the detection of spin qubit states via current measurements. This read-out approach was originally suggested in the Kane proposal for a spin-based quantum computer [Kan98] but it required more than ten years to be implemented for a single donor [MPZ$^+$10].

The first experimental demonstration of single-donor electron spin read-out has been

achieved by coupling it to a single electron transistor (SET) [MPZ+10]. This experimental technique is based on a spin-dependent tunnelling process. By applying an external magnetic field, the Zeeman energy splits the electron spin levels and the electron has enough energy to tunnel into the SET only in a certain spin state. This tunnelling process is then detected as a change in the current through the SET. The same read-out technique has been also used to detect local ESR manipulation of a single electron spin obtained by a local microwave resonator.

Scalability of donor spin devices

Even though control and read-out of a spin qubit in silicon have been recently demonstrated, it is still not entirely clear what could be the best strategy to implement multi-qubit gate operations.

Kane suggested performing multi-qubit gate by a controllable exchange coupling between donors. However, this coupling is restricted to the nearest neighbours and it is difficult to control because its strength is extremely sensitive to the donor position [SDK03]. In order to overcome this limitation, several alternative approaches have been suggested. In 2003, Skinner *et al.* suggested an architecture for quantum computing with electron shuttling between donors to enable multi-qubit operations [SDK03]. More recent proposals involve the coupling of electron spins with quantum dots [SLW+11] and with superconducting resonators [KOB+10].

How to address scalability and multi-qubit interactions is now one of the most important open questions in the field of donor spin qubit device for quantum information. The mediated interaction by other physical systems and the coherent shuttling of electrons seem to be the most promising approaches. These approaches do not require precise donor positioning and seems to be more reproducible.

2.4. Conclusions

In this Chapter, we have discussed some of the main requirements for the application of donor spins as qubits in together with some of the main experimental achievements in this direction. For instance, it has been possible to manipulate donor electron and nuclear spins [MTB+08] and to further enhance nuclear coherence time by suppressing the hyperfine interaction [SSS+13]. Moreover, single-spin read-out has been demonstrated by coupling an electron spin to an SET [FMM+12, PTD+12].

However, much more still needs to be done in order to realise a practical quantum computer architecture. It is still not clear, for example, how charge manipulation schemes may be implemented without producing nuclear spin decoherence and how best to Stark-shift the donor spin resonance frequency for individual addressability.

CHAPTER 3

Donor electron spins in silicon

A donor impurity, replacing an atom in a silicon crystal lattice, produces a Coulomb potential that naturally confines an electron. As discussed in the previous Chapter, some silicon-based spin quantum computer architectures use the spin of donor electrons and nuclei as qubits. The basic physical proprieties that make possible the manipulation and control of spin qubits are reviewed in this Chapter. In particular, we discuss here those fundamental ideas that are relevant for the understanding of the experimental results in following Chapters and those proprieties that are different between group-V and group-VI donors, such as the electronic structure and the thermal equilibrium state. For example, phosphorous in silicon in its neutral ground state (Si:P^0) has a bound unpaired electron ($S = 1/2$) and it can be detected by ESR. In contrast, the impurities from group-VI, such as selenium, have two elec-

trons in their neutral ground state that results in an electron spin $S = 0$. In this case, ESR is only observed when the selenium donors are in the singly ionised state Si:Se^+.

3.1. Electronic levels

An electron is strongly localised around a donor impurity creating an accessible energy level in the silicon band gap. The energy separation between this level and the conduction band (i.e. ionisation energy) strongly depends on the donor electronic structure. For instance, the ionisation energies are of the order of $\sim$0.05 eV for group-V donors and $\sim$0.5 eV for group-VI.

The mechanism of donor electron confinement can be understood qualitatively as due to the Coulomb attraction of the nuclear charge localised on the impurity site. The resulting electrostatic potential can be approximated as $V \approx e/\epsilon r$, where ϵ is the static dielectric constant. Under this qualitative approximation, the electron wavefunction can be described by a hydrogen-like Schrödinger equation where the electron mass (m_e) is replaced with an appropriate effective mass m^*.

In the case of silicon, ϵ and m^* are such that this potential extends over a large number of lattice cells and the consequent hydrogen-like *orbits* have radii of the order of $\sim 5 - 50$ Å (for group-V impurities).

The electronic structure of donor in silicon has been extensively studied in the last sixty years both experimentally and theoretically. A more detailed Hamiltonian of a weakly bound donor electron can be written as

$$\mathcal{H}\Psi(\boldsymbol{r}) = \left[-\frac{\hbar^2}{2m_e}\nabla^2 + V(\boldsymbol{r}) + U(\boldsymbol{r})\right]\Psi(\boldsymbol{r}). \tag{3.1}$$

where $\Psi(\boldsymbol{r})$ is the wavefunction of the donor electron, m_e is its rest mass, $V(\boldsymbol{r})$ is the periodic potential of the undoped silicon crystal and $U(\boldsymbol{r})$ is the interaction with the donor potential [PWU$^+$14].

The solution of the Hamiltonian 3.1 can be written in an approximated form as linear combinations of Bloch functions, that are the solution for free conduction electrons in silicon described by the Hamiltonian

$$\mathcal{H}_0\ \phi(\boldsymbol{r}) = \left[-\frac{\hbar^2}{2m_e}\nabla^2 + V(\boldsymbol{r})\right]\phi(\boldsymbol{r}). \tag{3.2}$$

where $\phi(\boldsymbol{r})$ are the Bloch functions. This approach is the basis of the so called effective mass theory (EMT) that offers a good qualitative understanding of the electronic wavefunctions.

In the EMT approximation, the electron wavefunction is mainly composed of Bloch waves chosen near the bottom of the conduction band minima. In silicon there are 6 equivalent minima of the conduction band corresponding to the different directions in k-space ($\pm x$, $\pm y$, $\pm z$) and the solutions for the electron wavefunction can be written in the form

$$\Psi(\boldsymbol{r}) = \sum_{j=1}^{6} \alpha_j F_j(\boldsymbol{r})\phi_j(\boldsymbol{r}) \tag{3.3}$$

where $F_j(\boldsymbol{r})$ are *hydrogen-like* envelope functions and α_j are coefficients for each band minimum j.

The solution for the ground state of a donor electron function $\Psi_0(\boldsymbol{r})$ obtained by the effective mass theory can be further corrected by taking into account the tetrahedral symmetry proprieties of the silicon crystal. Under this correction, the six-times degenerate ground state ($1s$) splits into three states called $1s(A_1)$, $1s(T_2)$ and $1s(E)$. This splitting is usually referred as *valley-orbit* spitting and it is well described by the effective mass theory (EMT). The degeneracy is further removed by the so called *spin-valley* splitting, due to the electron spin. Under this representation the first excited state $1s(T_2)$ splits in the Γ_7 and Γ_8 states.

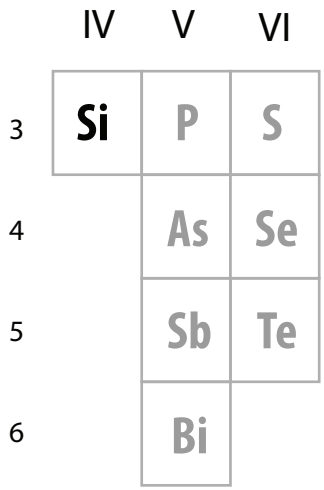


Figure 3.1.: **Periodic table with potential donor elements from group-V and group-VI.**

Group-VI impurities in silicon have two additional electrons with respect to the lattice and we refer to them as double donors. Due to the Coulomb potential, the electronic structure of double donors in silicon (such as S, Se and Te) is helium-like. The electronic structure of group-VI donors have been extensively investigated in the last thirty years due to their scientific and technological interest [GJS80, GJE+81, SLT80, GJL82, JSGG84, PMSH88, HAGD00, SYT+09]. S, Se and Te impurities also occupy one of the lattice tetrahedral sites and in their neutral ground state have two electrons in the singlet $1s(A_1)$ [GJL82]. Because the orbital wavefunction has a symmetric configuration, the total spin of the electrons is $S = 0$. These results for selenium, sulphur and tellurium have given a strong contribute for the understanding of the electronic structure of deep centres in general [JSGG84].

The double donor structure of group-VI donors in silicon was first identified by studying the energy levels of the impurities by deep level transient spectroscopy (DLTS) and by temperature dependent thermal emission techniques [GJS80]. The ionisation energies of Se^0 (307 meV) and Se^+ (593 meV) were obtained by charge techniques on *pn*-diodes [GJL82].

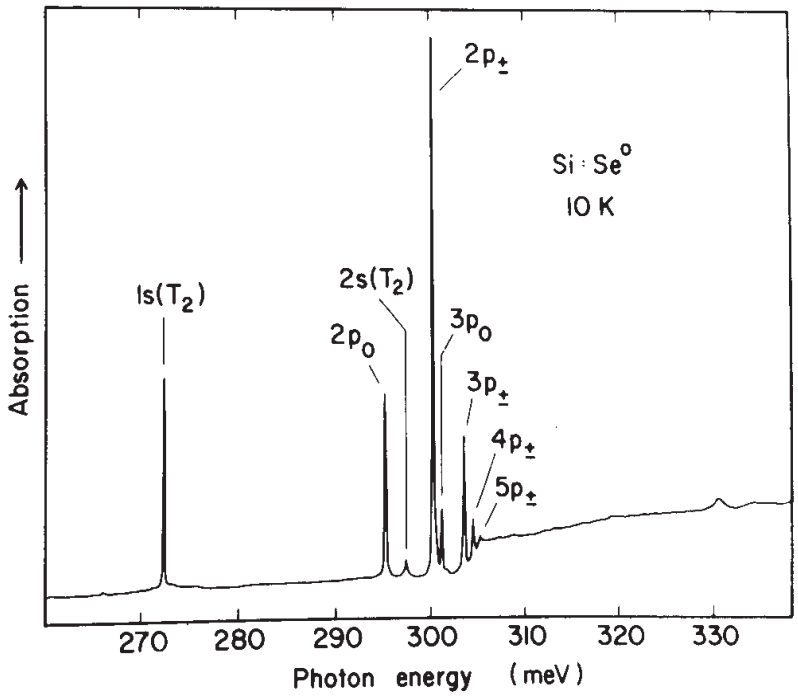


Figure 3.2.: **Absorption spectrum of Se^0 of selenium diffused in silicon:** The transition peak at lowst energy arises from the electrical dipole-allowed transition from the ground state $1s(A)$ to the first excited state $1s(T_2)$ that originates from the multi-valley structure. The transition to the Rydberg states at higher energies visible in the spectra correspond to $2s$, $2p$, $3p$, $4p$ and $5p$. (data from [JSGG84]).

More accurate information on the excited states structure of selenium was obtained by IR optical absorption spectroscopy at low temperature. Optical spectroscopy has demonstrated the existence of two kind of excited state: those that are generally referred as Rydberg states and those that originate from the multi-valley nature of the silicon conduction band [SLT80].

An optical absorption spectrum of Se^0 is shown in Figure 3.2 (data from [JSGG84]). The schematic in Figure 3.3 summarises the optical transitions from the ground state to some excited states and their energies for both Se^0 and Se^+. Higher resolution spectroscopy for the ionised selenium (Se^+) has shown that the $1s(T_2)$ state exhibits a spin-valley splitting due to the atomic spin-orbit coupling. This splitting removes the degeneracy of the $1s(T_2)$ into the state $1s(T_2)\Gamma_7$ and $1s(T_2)\Gamma_8$ states with an

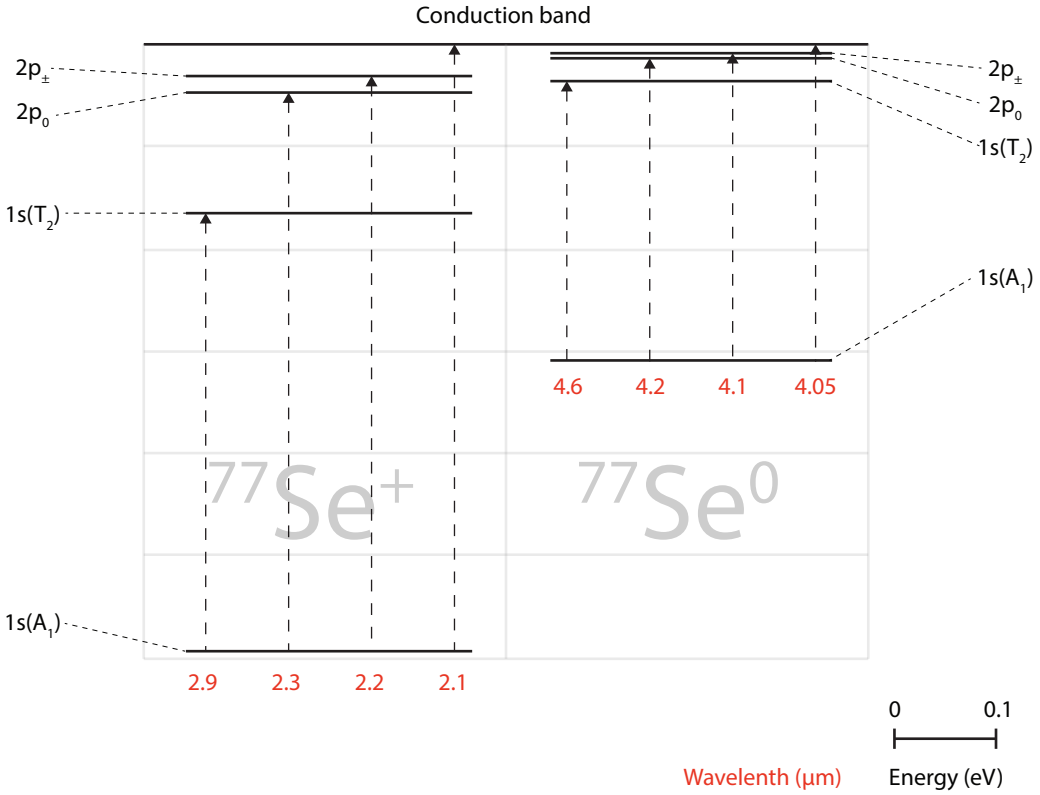


Figure 3.3.: **Optical transitions from the ground state for Se^0 (right) and Se^+ (left):** In the schematics, the separation between the ground state and conduction band (and excited states) is in scale with the relative energy difference (in red the equivalent wavelength of the optical transition). The ionisation energy of neutral selenium (Se^0) is 307 meV (4.05 μm). The energy separation with the first excited state $1s(T_2)$ is 272 meV (4.55 μm). The ground state of the ionised selenium Se^+ has an energy separation from the conduction band of 593 meV (2.1 μm). The energy separation with the first excited state $1s(T_2)$ is 429 meV (2.9 μm) [JSGG84].

energy separation of 2.3 meV. This result confirms that the main contribution to the wavefunction of the electron in the $1s(T_2)$ state originates from the six equivalent minima of the conduction band [GJL82].

Isotopic purification of 28-silicon has more recently improved the resolution of optical detected spectra for donor impurities. Using this technique, a further splitting of the $1s(T_2)\Gamma_7$ transition has been measured in ^{28}Si:$^{77}Se^+$ [SYT+09]. This splitting is due to the hyperfine coupling of electron spin with the nuclear spin $I = 1/2$ in its ground state. The optical spectrum for this transition is shown in Figure 3.4 and

the two peaks are separated by 0.056 cm^{-1}, in perfect agreement with ground state hyperfine splitting previously determined by magnetic resonance [GJE+81]. Under an external magnetic field the doublet further splits into eight lines, as expected from the energy diagram, also shown in Figure 3.4. This result demonstrates that, under an applied magnetic field, it is possible to spectrally resolve the ground state hyperfine coupling in $^{28}Si:^{77}Se^+$ using the $1s(T_2)\Gamma_7$ absorption transition [SYT+09]. Therefore, if a tuneable source were available at $\sim 2.9\ \mu m$ this could be used for fast and efficient hyperpolarization of both electron and nuclear spin, as already suggested [SYT+09].

ESR characterisation of singly-ionised selenium impurities (Se^+) was first reported by Grimmeiss *et al.* [GJE+81]. The electron-nuclear spin proprieties of Se^+ impurities in silicon can be described by the isotropic spin Hamiltonian in Equation 3.29, with an electronic g factor of $g = 2.0057$ and with nuclear spin of $I = 1/2$ for the 77-selenium and zero for all other isotopes. The electron and nuclear spins of the ^{77}Se are coupled with the hyperfine constant of $A = 1.66$ GHz [GJE+81].

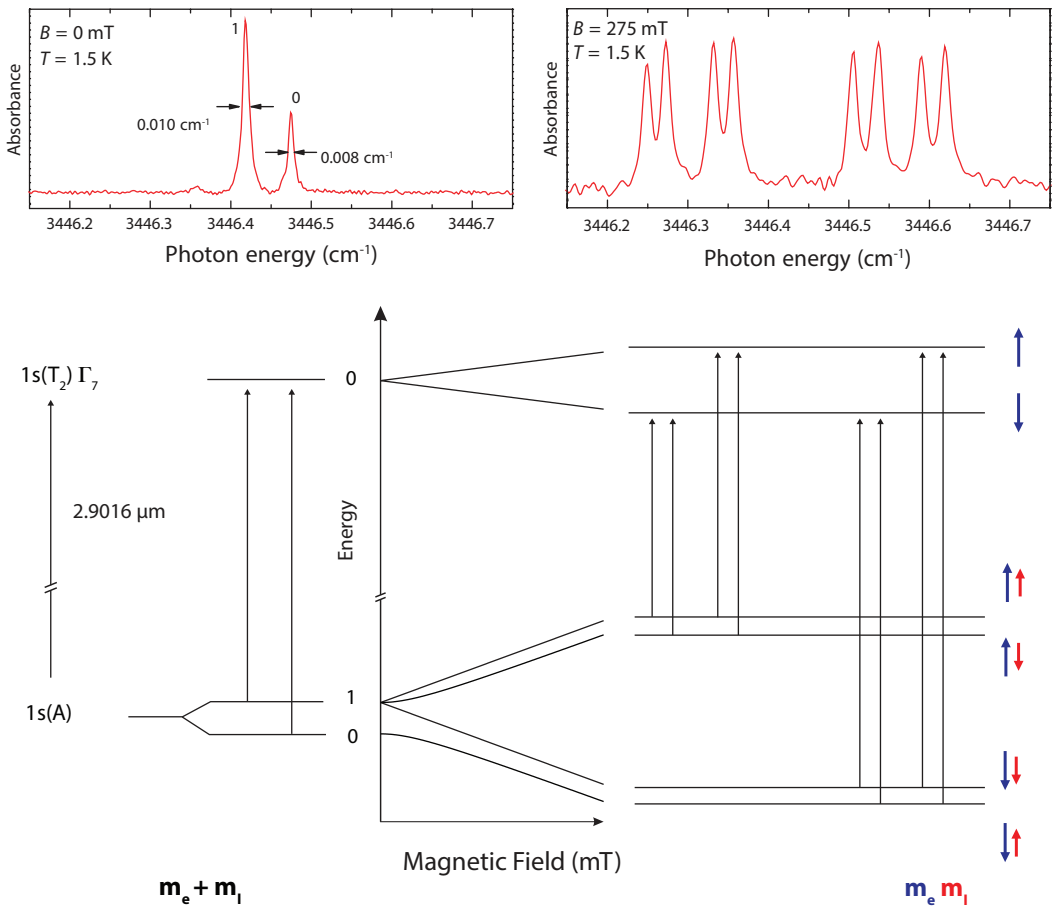


Figure 3.4.: **Spectrum of the $^{77}Se^{+}$ $1s(T_2)\Gamma_7$ transition in ^{28}Si and diagram of the energy levels and relative transitions as a function of magnetic field:** (Top-left) Spectrum without external magnetic field showing the ground state hyperfine splitting. (Bottom-left) Energy levels of the ground state and relative transitions without magnetic field. (Top-right) Spectrum with a magnetic field of 275 mT. The ground state doublet splits into eight transitions accordingly to the diagram in the (bottom-right) where the red and blue arrows represent the nuclear (m_I) and electron (m_e) spins respectively. (Bottom-centre) Energy level of the ground state and of $1s(T_2)\Gamma_7$ as a function of magnetic field. $T = 1.5$ K (data from [SYT+09])

3.2. Population of electronic levels in thermal equilibrium

Electron spin manipulation of group-V donors requires the electron to be bound to the impurity. In silicon, donor thermal excitation depends on the concentration of impurities (donor and acceptors), ionisation energy and temperature. Each donor may get thermally ionised only when its electron gets enough energy to fill the first available level in the conduction band. For this reason, the population of donor electronic levels at thermal equilibrium also depends on the density of free carriers.

Given a certain concentration of donors [D] and acceptors [A] the population of all electronic levels can be determined by solving a balance equation written as a function of chemical potential (μ) and temperature (T). In particular, the total concentration of conduction electrons (n_c) or electrons bound to the donors (n_d) must be equal to the total concentration of conduction holes (p_v) or holes bound to the acceptor (p_a) plus the excess of electrons in the sample.

As we discussed in the previous Section, each donor from group-V and group-VI contributes one and two electrons respectively and has very different ionisation energies. These properties contribute to a different behaviour as a function of temperature and concentration. In this Section, we review the main consequences of those differences for phosphorus and selenium as examples of each group.

For phosphorus doped silicon, each impurity contributes one electron and the excess of electrons in the sample is equal to the concentration of phosphorus [P] minus the concentration of acceptors [A]. The balance equation in this case reads

$$n_c + n_{\mathrm{P}} = [\mathrm{P}] - [\mathrm{A}] + p_v + p_{\mathrm{A}}. \tag{3.4}$$

For selenium, the numbers of electrons per donor is two and we have

$$n_c + n_{\mathrm{Se}} = 2[\mathrm{Se}] - [\mathrm{A}] + p_v + p_{\mathrm{A}}. \tag{3.5}$$

Solving these equations requires the explicit dependence of n_{P}, n_{Se}, n_c, p_a and p_v on chemical potential and temperature. From the solution of Eq. 3.4 and Eq. 3.5 we get the value of the chemical potential from which we can compute the mean occupation of the energy levels of each impurity per each temperature. In the following Sections, we derive the explicit form of n_{P} and n_{Se} and we describe the solution of Eq. 3.4 and Eq. 3.5 for different donors and acceptor concentrations.

Group-V donors

The charge occupation of each group-V donor could be either zero (P^+), one (P^0) or two (P^-). The concentration of bound electrons is then equal to $n_{\mathrm{P}} = \langle \mathrm{P}^0 \rangle + 2\langle \mathrm{P}^- \rangle$.

In this Section, we neglect the doubly-occupied state for group-V donors because the Coulomb repulsion between the two electrons makes the energy of this state so high that it become irrelevant for the purpose of determining thermal equilibrium condition.

For a given value of chemical potential and temperature the population of each level (n_j), with energy (E_j), can be calculated using the Fermi-Dirac distribution

$$n_j = \frac{1}{\mathcal{Z}} d_j \exp\left\{-\beta \left(E_j - N_j \mu\right)\right\} \tag{3.6}$$

where $\beta = 1/k_B T$, d_j is the degeneracy of the level, N_j is the number of electrons

and $\mathcal{Z}$, the partition function, is

$$\mathcal{Z} = \sum_j d_j \exp\{-\beta\,(E_j - N_j\mu)\}. \tag{3.7}$$

Applying Equation 3.6 for phosphorus we have

$$\frac{n_P}{[\mathrm{P}]} = \frac{1}{1 + \frac{1}{2}e^{\beta(S - E_P - \mu)}} \tag{3.8}$$

where S is the energy of the band gap and E_P is the ionisation energy.

Under the so called *non-degeneracy* approximation ($\epsilon_c - \mu \gg k_B T$ and $\epsilon_v - \mu \ll k_B T$ where ϵ_c and ϵ_v are the energy of the conduction and valence band respectively) the explicit dependence of the carrier density can be written as

$$\begin{aligned} n_c(\mu, T) &\approx N_c(T)\ e^{-\beta(\epsilon_c - \mu)} \\ p_v(\mu, T) &\approx P_v(T)\ e^{-\beta(\mu - \epsilon_v)} \end{aligned} \tag{3.9}$$

where we define

$$\begin{aligned} N_c(T) &= \frac{1}{2}\left(\frac{2m_c k_B T}{\pi\hbar^2}\right)^{3/2} \\ P_v(T) &= \frac{1}{2}\left(\frac{2m_v k_B T}{\pi\hbar^2}\right)^{3/2} \end{aligned} \tag{3.10}$$

where m_c and m_v are the effective masses of an electron in the conduction band and an hole in valence band, respectively. In the case in which the *non-degeneracy* approximation is valid and at $T = 0$, the number of conduction carriers goes to zero and Equation 3.4 becomes

$$n_{\mathrm{P}} = [\mathrm{P}] - [\mathrm{A}] + p_{\mathrm{A}}. \tag{3.11}$$

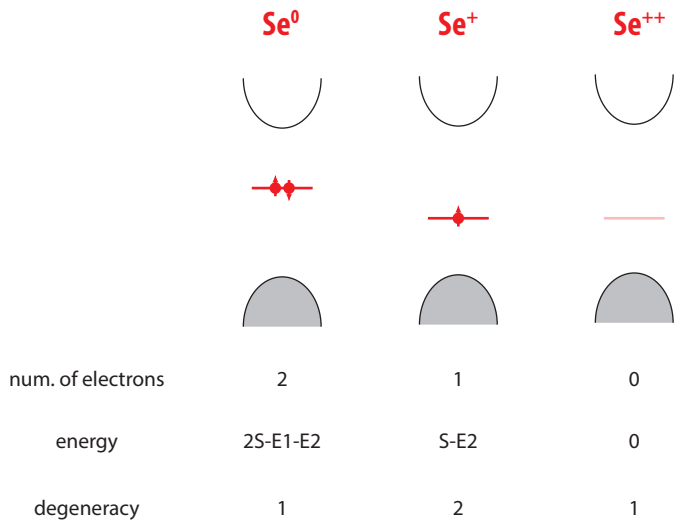


Figure 3.5.: **Selenium electronic configurations.** Neutral (Se^0), ionised (Se^+) and doubly ionised (Se^{++}) states. Band gap (S), first ionisation (E_1) and second ionisation (E_2) energies.

If the sample is *n-doped* and the concentration of acceptors is negligible ($[P] \gg [A]$), at low temperature all the donors are in the neutral state ($\langle P^0 \rangle \approx [P]$). Increasing the temperature above ~ 30 K the donors start to get ionised and at $T = 300$ K we have the condition of full-ionisation where the number of free carrier is given by

$$\begin{aligned} n_c &\approx [P] \\ p_v &\approx \frac{N_c(T) P_v(T) e^{-\beta(\epsilon_c - \epsilon_v)}}{[P]}. \end{aligned} \tag{3.12}$$

ESR detection of the electron spin of phosphorus is thus only possible below 30 K where electrons are bound to the donors. In presence of acceptors the number of ionised donors at low temperature is reduced.

Group-VI donors

Group-VI impurities have three available charge states: neutral (Se^0), ionised (Se^+) and doubly ionised (Se^{++})

Figure 3.5 shows these available configurations with their relative energies and degeneracies. Applying the Fermi-Dirac statistics in Equation 3.6 for the selenium states we have

$$\frac{\langle Se^0 \rangle}{[Se]} = \frac{1}{\mathcal{Z}} \exp\left\{-\beta\left(2S - E_1 - E_2 - 2\mu\right)\right\} \tag{3.13}$$

$$\frac{\langle Se^+ \rangle}{[Se]} = \frac{1}{\mathcal{Z}} 2 \exp\left\{-\beta\left(S - E_2 - \mu\right)\right\} \tag{3.14}$$

$$\frac{\langle Se^{++} \rangle}{[Se]} = \frac{1}{\mathcal{Z}} \tag{3.15}$$

and

$$\mathcal{Z} = \exp\left\{-\beta\left(2S - E_1 - E_2 - 2\mu\right)\right\} + 2\exp\left\{-\beta\left(S - E_2 - \mu\right)\right\} + 1 \tag{3.16}$$

where S is the silicon band gap energy, E_1 and E_2 are the first and second ionisation energies of selenium, respectively. The mean number of electrons bound to the selenium donor, n_{Se}, is then calculated by the equation

$$n_{Se} = 2\langle Se^0 \rangle + \langle Se^+ \rangle. \tag{3.17}$$

Figure 3.6 gives the relative mean occupations of the electronic levels of the selenium impurity: Se^0, Se^+ and Se^{++} and the normalised concentration of electrons bound to the selenium donors (n_{Se}) as a function of chemical potential, μ. At $T = 0$ K, for ($\mu < S - E2$), selenium donor are mostly doubly ionised, for ($S - E2 < \mu < S - E1$) they are singly ionised and for ($\mu > S - E1$) they are mostly neutral.

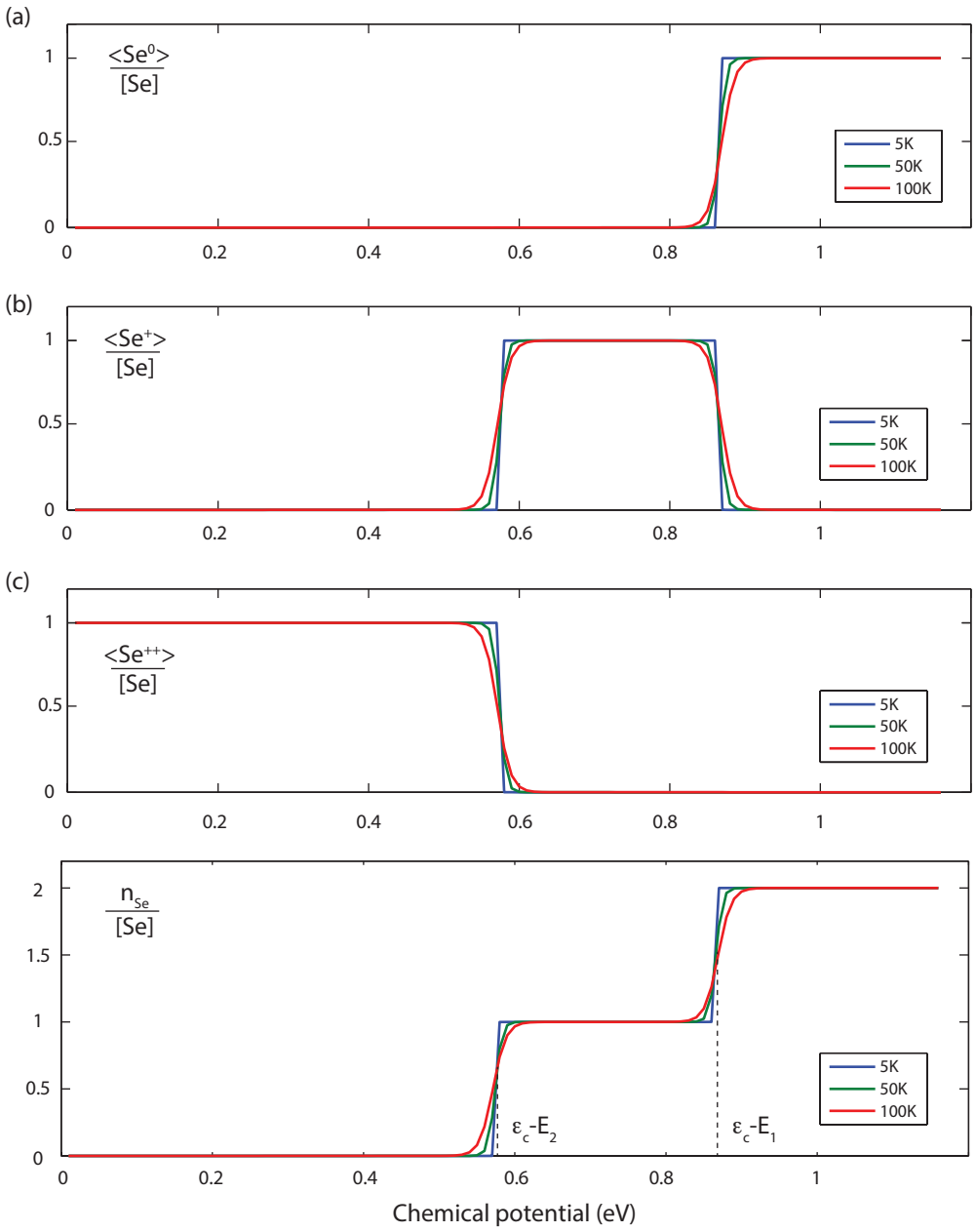


Figure 3.6.: **Relative occupations of the electronic levels of the selenium impurity and normalised concentration of electrons bound to the selenium donors at thermal equilibrium:** Relative mean concentration of Se^0 (a), Se^+ (b) and Se^{++} (c) and normalised concentration of electrons bound to the selenium donors (d) as a function of chemical potential, μ, for different values of temperature, 5 K (blue), 50 K (green) and 100 K (red).

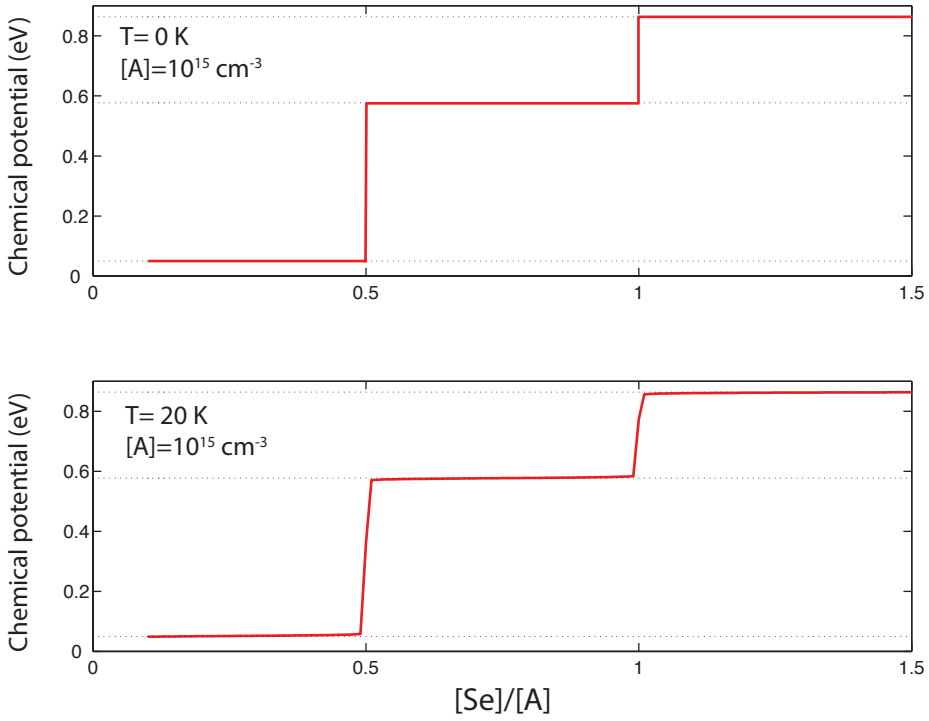


Figure 3.7.: **Chemical potential at thermal equilibrium as function of impurity concentration.** The value of chemical potential at T=0 K (a) and T=20 K (b) as a function of the ratio [Se]/[A] for [A] = 10^{15}cm^{-3}

For [Se] $\gg$ [A], the number of extra electrons exceeds the number of holes and the sample is *n-doped* and for [Se] $\ll$ [A], the sample is *p-doped*. At $T = 0$ K, the valence band is filled and the contribution of free carriers (electrons and holes) can be neglected. In this case the Equation 3.5 simplifies as follows

$$n_{\mathrm{Se}} = 2[\mathrm{Se}] - [\mathrm{A}] + p_{\mathrm{A}}. \tag{3.18}$$

The solutions of Equation 3.18 at $T = 0$ K as a function of the ratio [Se]/[A] are plotted in Figure 3.7 for an arbitrary value of acceptor concentration ([A] = 10^{15} cm^{-3}). Three different scenarios can be identified.

(1) *n-doped*, [Se]/[A] $\gg 1$: the value of chemical potential is larger then $S - E_1$ and most of the Se impurities are in the Se^0 state. In this case, as many electrons as the

number of acceptors, move from the donors to fill all the acceptor levels. Then we have $\langle Se^0 \rangle \approx [Se] - [A]$ and $\langle Se^+ \rangle \approx [A]$.

(2) *p-doped*, $[Se]/[A] \ll 0.5$: the value of chemical potential is much lower than $S - E_2$ and it is close to E_a. In this scenario all of the selenium impurities are in the state Se^{++}. Because the number of acceptors largely overcomes the number of donors, all the donor electrons will be bound to the acceptors.

(3) *highly compensated*, $[A]/2 < [Se] < [A]$. In this intermediate regime, most of the selenium impurities are in the state Se^+. Each of the ionised selenium donor gives one electron to one acceptor.

In conclusion, ESR detection of group-VI donor spins (at thermal equilibrium and low temperature) requires the presence of acceptors to compensate the sample in order to form the D^+ state. However, the concentration of acceptors has to be kept such that $[A] < 1/2[D]$ in order to avoid the formation of D^{++}.

3.3. Electron and nuclear spin Hamiltonian

Analogously to the orbital angular momentum, the spin of electrons $\boldsymbol{S}$ has some magnetic moment $\boldsymbol{\mu}$. In the simple case of a free electron with $S = 1/2$ the moment associated with its spin is given by

$$\boldsymbol{\mu} = -\frac{g_e \beta}{\hbar} \boldsymbol{S} \tag{3.19}$$

where $\beta = 9.27 \times 10^{24}\ \mathrm{J\,T^{-1}}$ is the Bohr magneton and $g_e = 2.00231(9)$ is the g-value of free electrons. The spin operator $\boldsymbol{S}$ is defined as $S_{x,y,z} = 1/2\ \sigma_{x,y,z}$ with σ_i, the Pauli matrixes, given by

$$\sigma_x = \begin{pmatrix} 0 & 1 \\ 1 & 0 \end{pmatrix}, \tag{3.20}$$

$$\sigma_y = \begin{pmatrix} 0 & -i \\ i & 0 \end{pmatrix} \tag{3.21}$$

and

$$\sigma_z = \begin{pmatrix} 1 & 0 \\ 0 & -1 \end{pmatrix}. \tag{3.22}$$

Under an applied magnetic field $\boldsymbol{B} = (0, 0, B)$, the electron spin energy levels are described by the electron Zeeman Hamiltonian (in frequency units)

$$\mathcal{H}_{EZ} = \omega_e S_z \tag{3.23}$$

where $\omega_e = g_e \beta B/\hbar$. In this condition, the electron spin gives rise to an effective quantum two level system where $|m_s = 1/2\rangle$ and $|m_s = -1/2\rangle$ are the eigenstates with energy separation given by $\hbar\omega_e$.

Donor	Group	S	I	E_d (meV)	g	A (MHz)	Reference
^{31}P	V	1/2	1/2	45.6	1.9992	117.53	[TLAR03]
^{75}As	V	1/2	3/2	53.8	1.99837	198.35	[Feh59]
^{121}Sb	V	1/2	5/2	42.7	2.0004	186.8	[FYPM54]
^{209}Bi	V	1/2	9/2	71.0	2.0003	1475.4	[WST$^+$12b]
$^{33}S^0$	VI	0	1/2	318	-	-	[GJE$^+$81]
$^{33}S^+$	VI	1/2	1/2	612	2.0054	312.4	[GJE$^+$81]
$^{77}Se^0$	VI	0	1/2	307	-	-	[GJE$^+$81]
$^{77}Se^+$	VI	1/2	1/2	589	2.0057	1658.5	[GJE$^+$81]
$^{125}Te^0$	VI	0	1/2	199	-	-	[GJE$^+$81]
$^{125}Te^+$	VI	1/2	1/2	411	2.0023	3491.7	[GJE$^+$81]

Table 3.1.: **Experimental values of ionisations energies, g-values, hyperfine interactions for donors in silicon.**

Electron and nuclear spins of donors in silicon can be described by the spin Hamiltonian

$$\mathcal{H}_0 = \mathcal{H}_{EZ} + \mathcal{H}_{SO} + \mathcal{H}_{NZ} + \mathcal{H}_{HF} + \mathcal{H}_{\text{bath}}. \tag{3.24}$$

where in addition to the electron Zeeman term we also consider the spin-orbit interaction ($\mathcal{H}_{SO}$), the nuclear Zeeman term ($\mathcal{H}_{NZ}$), the hyperfine electron-nuclear interaction ($\mathcal{H}_{HF}$) and $\mathcal{H}_{\text{bath}}$ that contains all remaining interactions with other nuclear spins and thermal phonons that are responsible for spin relaxation.

The first two terms of $\mathcal{H}_0$ take into account the electron spin $\boldsymbol{S}$, the orbital angular momentum $\boldsymbol{L}$ and their interaction. $\mathcal{H}_{EZ}$ and $\mathcal{H}_{SO}$ are usually written in the approximated form

$$\mathcal{H}_{EZ} + \mathcal{H}_{SO} = \frac{\beta}{\hbar}\boldsymbol{L} \cdot \boldsymbol{B} + \frac{g_e\beta}{\hbar}\boldsymbol{S} \cdot \boldsymbol{B} + \lambda \boldsymbol{L} \cdot \boldsymbol{S} \approx \frac{\beta}{\hbar}\boldsymbol{S} \cdot \boldsymbol{g} \cdot \boldsymbol{B} \tag{3.25}$$

where $\boldsymbol{g}$ is the Landé g-tensor that takes into account the angular orbital momentum and the spin-orbit interaction. For most donors in silicon the ground state wavefunction is isotropic due to the symmetric linear combination of all six bands and we have $g \approx 2$.

Analogously to the electron Zeeman Hamiltonian, $\mathcal{H}_{NZ}$ gives the nuclear Zeeman term for the donor nuclear spin I:

$$\mathcal{H}_{NZ} = -\omega_n \boldsymbol{I} \cdot \boldsymbol{B} \tag{3.26}$$

where $\omega_n = g_n \beta_n B_0/\hbar$ with g_n the nuclear g-value and $\beta_n = 5.05 \times 10^{-27}\,\mathrm{J\,T^{-1}}$ the nuclear magneton. The last term of the spin Hamiltonian above, $\mathcal{H}_{HF}$ gives the electron-nuclear spin interaction

$$\mathcal{H}_{HF} = \boldsymbol{S} \cdot \boldsymbol{A} \cdot \boldsymbol{I} \tag{3.27}$$

where $\boldsymbol{A}$ is the hyperfine tensor that for isolated impurities in silicon is usually isotropic. The most relevant part of the hyperfine interaction $\mathcal{H}_{HF}$ is due to the Fermi contact scalar term $A\,\boldsymbol{S} \cdot \boldsymbol{I}$, where the hyperfine constant A is given by

$$A = \frac{2}{3}\frac{\mu_0}{\hbar} g_e \beta g_n \beta_n |\Psi_0(r=0)|^2 \tag{3.28}$$

where μ_0 is the vacuum permeability [PWU+14]. Table 3.1 reports the experimental g-values, hyperfine values and the nuclear spin I of some donor impurities from group-V and group-VI.

For isolated donor impurities in silicon the Hamiltonian in Equation 3.24 can be simplified to the isotropic form:

$$\mathcal{H}_0 = \omega_e S_z - \omega_n I_z + A\,\boldsymbol{S} \cdot \boldsymbol{I} \tag{3.29}$$

where we are not considering the interaction with the environment. The solutions of Equation 3.29 depend on the values of I for each impurity. As an example, we consider the case of $I = 1/2$ which applies both in the case of ^{31}P and ^{77}Se^{+}. In this

case, the eigenstates are

$$\begin{aligned} |1\rangle &= |\downarrow\Downarrow\rangle \\ |2\rangle &= \sin(\eta)\,|\downarrow\Uparrow\rangle + \cos(\eta)\,|\uparrow\Downarrow\rangle \\ |3\rangle &= \cos(\eta)\,|\downarrow\Uparrow\rangle - \sin(\eta)\,|\uparrow\Downarrow\rangle \\ |4\rangle &= |\uparrow\Uparrow\rangle \end{aligned} \tag{3.30}$$

where $\{|\uparrow\rangle, |\downarrow\rangle\}$ $\{|\Uparrow\rangle, |\Downarrow\rangle\}$ are the electron and nuclear spin up and down states respectively and we set

$$\eta = \arctan\left(\frac{2a}{\Delta_+ + \sqrt{\Delta_+^2 + 4a^2}}\right) \tag{3.31}$$

The energy spectrum as a function of the magnetic field can be written as

$$\begin{aligned} \lambda_1 &= a - \Delta_- \\ \lambda_2 &= -a + \sqrt{\Delta_+^2 + 4a^2} \\ \lambda_3 &= -a - \sqrt{\Delta_+^2 + 4a^2} \\ \lambda_4 &= a + \Delta_- \end{aligned} \tag{3.32}$$

where we set $\Delta_+ = 1/2(\omega_e + \omega_n)$, $\Delta_- = 1/2(\omega_e - \omega_n)$ and $a = A/4$. With no external magnetic field applied ($B_0 = 0$) the solutions of the Hamiltonian are given by $\{\lambda_1 = a, \lambda_2 = a, \lambda_3 = -3a, \lambda_4 = a\}$. The eigenvalues $\{\lambda_1, \lambda_2, \lambda_4\}$ are energy degenerate and the separation with the last eigenstate is equal to the hyperfine splitting.

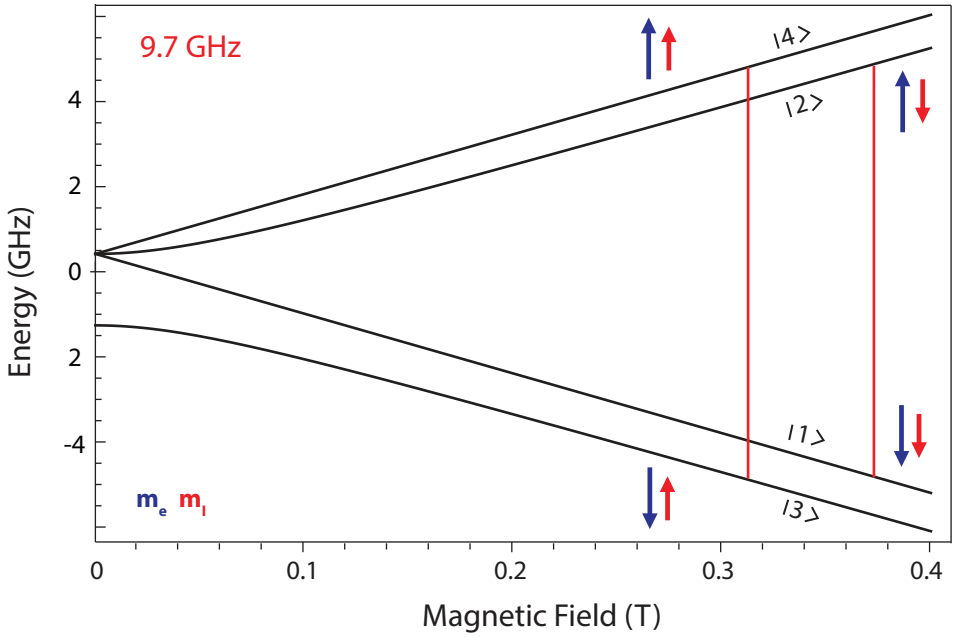


Figure 3.8.: **Energy levels of Si:^{77}Se^{+} as function of magnetic field.** Spin resonance allowed transitions in a ESR experiment at X-band microwave excitation (9.7 GHz).

Figure 3.8 illustrates the energy spectrum of the Hamiltonian as function of the applied magnetic field B_0 for Si:Se^{+}, with the allowed ESR transitions ($\Delta m_e = \pm 1$ and $\Delta m_I = 0$) at X-band (9.7 GHz). These transitions have frequencies given by

$$\begin{aligned} f_{12} &= \Delta_- + \sqrt{\Delta_+^2 + 4a^2} - 2a \\ f_{34} &= \Delta_- + \sqrt{\Delta_+^2 + 4a^2} + 2a. \end{aligned} \tag{3.33}$$

In the high field limit ($\omega_e \gg A$) the diagonal terms of the hyperfine interaction become negligible and the eigenstates can be approximated to the electron and nuclear spin-up and spin-down states ($|2\rangle \approx |\uparrow\Downarrow\rangle$ and $|3\rangle \approx |\downarrow\Uparrow\rangle$). This condition is represented in the schematic in Figure 3.9. The dashed lines in the schematic represent the ESR allowed transitions, each of which corresponds to a nuclear spin projection, m_I.

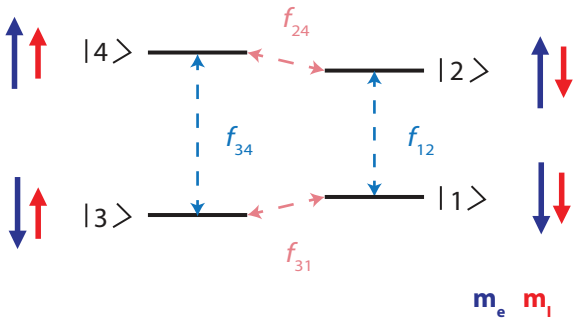


Figure 3.9.: **Energy levels of the electron-nuclear spin Hamiltonian for $I = 1/2$ in the high field limit $\omega_e \gg A$.** Blue dashed lines represents allowed ESR transitions, relative to $\Delta m_e = \pm 1$ and $\Delta m_I = 0$. Pink dashed lines corresponds to nuclear spin transitions ($\Delta m_I = \pm 1$ and $\Delta m_e = 0$).

In the rest of this thesis, we always assume that this high field approximation is valid (unless stated otherwise) and we refer to ESR transition as f_{m_I}. Although, the solutions of the Hamiltonian in Equation 3.29 have been discussed for the case of $I = 1/2$, most of the results introduced in this Section can be generalised for an arbitrary nuclear spin I.

3.4. Stark shift of donors in silicon

The resonance frequencies of the donor spins described in the previous Section can be modified under the application of an external electric field. This effect, called the Stark shift, has been introduced in Section 2.3 as a strategy for individual spin addressability.

In order to quantify the Stark effect on the donor spin resonance frequency, we consider a donor in silicon placed under an external electric field $\boldsymbol{E}$ parallel to the z direction. Under this condition, the interaction energy W of the donor electric dipole moment $e\boldsymbol{r}$ with the electric field can be written as

$$W = e\,\boldsymbol{E}\,\cdot\,\boldsymbol{r} = eEz. \tag{3.34}$$

The effect on the donor electron wavefunction can be then obtained by solving the Hamiltonian in Equation 3.1 adding the interaction energy W with the electric field $\boldsymbol{E}$. However, a simple qualitative understanding of the Stark effect can be obtained by applying the perturbation approach to the ground state solution $\Psi_0(\boldsymbol{r})$ of effective mass theory (EMT). According to perturbation theory, the first order correction can be calculated by

$$eE\,\langle\Psi_0|\,z\,|\Psi_0\rangle\,. \tag{3.35}$$

where $\Psi_0(\boldsymbol{r})$ is proportional to an *hydrogen-like* ground state function, as discussed in Section 3.1. Since $\Psi_0(\boldsymbol{r})$ has an even parity and the operator z is odd the first order Shark correction is zero. Therefore the first non-zero contribution is quadratic in electric field.

The Stark effect on the donor wavefunction arises from pulling away the electron

Donor	A (MHz)	$\lvert\Psi_0(0)\rvert^2$ (cm^{-3})	η_a (μm^{2}V^{-2})
^{31}P	117.53	0.46×10^{24}	-3.0×10^{-3}
^{75}As	198.35	1.78×10^{24}	-1.2×10^{-3}
^{121}Sb	186.8	1.15×10^{24}	-3.7×10^{-3}
^{209}Bi	1475.4	1.4×10^{24}	-0.16×10^{-3}

Table 3.2.: Hyperfine coupling constants A, square mean values of the electron wavefunction at the nuclear site and quadratic Stark shift coefficient of the hyperfine constants calculated theoretically by G. Pica *et al.* [PWU$^+$14].

from the nucleus, mixing its ground state with higher orbital excited states. In the earliest studies, the problem was analysed with perturbation theory using hydrogenic wavefunction and uniform electric fields [LFKV00]. Using tight-binding theory, a more precise description of the Stark shift and the hyperfine interaction was obtained [MBKK05, MCK04].

More recently, analytical calculations of this effect have been reported by G. Pica *et al.* [PWU$^+$14]. In the last reference, a variational theory approach has been used to quantify the correction to the wavefunction under a uniform electric field and good agreement with experimental results has been obtained. The first measurement of the Stark shift parameters for shallow donor in silicon was reported using electron spin resonance (ESR) of ^{121}Sb donors residing between interdigitated metallic electrodes evaporated on the silicon surface [BTS$^+$06].

These experiments resolved a quadratic dependence on the external electric field measured as a shift in the resonance frequency in a ESR experiment. The results have been compared to theoretical calculations obtained using the tight-binding and the band minima basis approaches showing a good agreement [RWB$^+$07].

The effect of the Stark shift on the resonance frequency is due to two independent contributions induced by spin-orbit and hyperfine field modulation. The first effect arises from the change in the spin orbit coupling induced by the distortion of the

electronic wavefunction. The second is due to the reduction of mean value of the electron wavefunction at the nuclear site $|\Psi_0(r=0)|^2$.

As introduced in Section 3.3 the hyperfine interaction due to the Fermi contact scalar term is proportional to $|\Psi_0(r=0)|^2$ and therefore, under the application of an electric field, Equation 3.28 can be rewritten as

$$A(E) = \frac{2}{3}\frac{\mu_0}{\hbar} g_e \beta g_n \beta_n |\Psi_0(r=0,E)|^2. \tag{3.36}$$

Under the application of an electric field E, the electron-nuclear spin Hamiltonian in Equation 3.29 is then

$$\mathcal{H}_0(E) = g(E)\,\frac{\beta B_0}{\hbar} S_z - \omega_n I_z + A(E)\,\boldsymbol{S}\,\cdot\,\boldsymbol{I}. \tag{3.37}$$

The frequency shift for the ESR transitions due to electric field can obtained from the Hamiltonian as $\Delta f(E) = f(E) - f(0)$ as described in Section 3.3. To first order, this shift can be approximated as

$$\Delta f(E) = \Delta g(E)\ \frac{df}{dg} + \Delta A(E)\ \frac{df}{dA}. \tag{3.38}$$

In the high field approximation ($\omega_e \gg A$), we have that $df/dg = \beta B_0/\hbar$ and $df/dA = m_I/\hbar$. The shift of the resonance frequency (Δf_{m_I}), for each ESR transition can then written as

$$\Delta f(E, m_I) = \eta_g E^2\ \frac{g\beta B_0}{\hbar} + \eta_a E^2\ \frac{m_I\, A}{\hbar} \tag{3.39}$$

where we define η_g and η_a form the equation

$$\begin{aligned} \frac{\Delta g(E)}{g} &= \eta_g E^2 \\ \frac{\Delta A(E)}{A} &= \eta_a E^2. \end{aligned} \tag{3.40}$$

The parameter η_g takes into account the relative change in electronic g-factor due to the induced spin-orbit modulation and η_a is the relative change in hyperfine interaction. As discussed before, the first order effect is quadratic with the applied electric field. The variation in the resonance frequency $\Delta f(E, m_I)$ is the physical quantity that can be measured experimentally by ESR, as discussed in Chapter 5.

The values of hyperfine constants A, the square mean values of the electron wavefunction at the nuclear site $|\Psi_0(r = 0)|^2$ and quadratic Stark shift coefficients η_a of the hyperfine constants obtained theoretically for different donors [PWU+14] are listed in Table 3.2.

3.5. Electron spin relaxation and decoherence

An ensemble of donor electron spins in silicon in a non-equilibrium distribution relax back via interactions with phonons. In this process, usually called spin-lattice relaxation, many mechanisms simultaneously contribute to the relaxation time, T_1.

The relaxation dynamics for group-V donors have been studied extensively both experimentally [Cas63, Cas67, HS60] and theoretically [Sug63, Shr83, Igo66], but only a few results have been reported for those of group-VI [Lud65].

In the case of group-V donors the relaxation is dominated by three different mechanisms depending on the magnetic field, temperature and donor concentration: direct, Orbach and Raman. In phosphorous doped silicon at low concentrations (below $\sim 10^{16}$ cm^{-3}), it has been experimentally found that electron spin relaxation can described by the equation

$$\frac{1}{T_1} = A(B^4) + CT^9 + D\exp\left(\frac{\Delta}{k_B T}\right) \tag{3.41}$$

where T is the temperature, B is the external magnetic field in Tesla, Δ is the energy separation between the ground and the first excited state, A, C and D are coefficients which describe the relative strength of these different mechanisms, with the following values obtained experimentally for P: $A = 10^{-6}$ s^{-1}T^4 (at $B \sim 0.3$ T), $C = 10^{-7}$ s^{-1}K^{-9} and $D = 2 \times 10^8$ s^{-1} [YH68].

Each term on right hand side of Equation 3.41 corresponds, respectively, to direct, Raman and Orbach mechanisms. The direct mechanism is a one-phonon relaxation process in which the emitted or absorbed phonon has energy equal to the Zeeman splitting. This mechanism does not depend on temperature and has a B^4 dependence on the external magnetic field. Therefore, the direct process dominates only at low

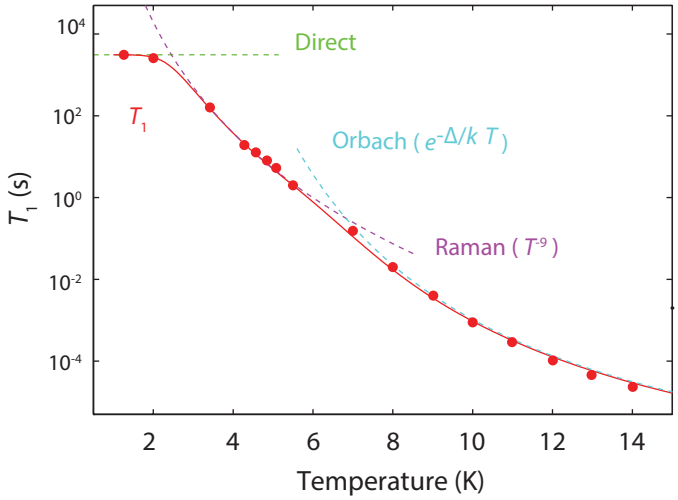


Figure 3.10.: **Temperature dependence of electron spin relaxation T_1 in ^{28}Si:P at** $B \sim 0.34$ T: Solid line is fit to the experimental data, made up of contributions (dashed lines) from different relaxation mechanisms (as indicated in Figure): direct, Raman, Orbach. Data from [Cas63].

temperature (for Si:P below 2.5 K at $B \sim 0.3$ T).

The Raman process has a T^9 temperature dependence and arises from two-phonon scattering via a continuum of excited states. For Si:P, this mechanism limits the electron spin relaxation in the range $2.5 - 6$ K at $B \sim 0.3$ T [Cas67]. It has been observed for shallow donors that the Raman process has only a weak dependence on Δ, which regulates spin mixing through a spin-orbit coupling.

The Orbach process is a second order process that involves transitions to the first excited state. It is independent of field, concentration (below $\approx 10^{16}$ cm^{-3}) and orientation [Orb61, Cas67]. The rate of this process depends exponentially on the energy gap, $\Delta = 1s(T_2) - 1s(A_1)$, between the ground state and first excited state of the donor: $T_1 \propto \exp(\Delta/k_B T)$. For example, energy difference is $\Delta = 11.6$ meV ($\Delta/k_B = 134.6$ K) for phosphorus and $\Delta = 34$ meV ($\Delta/k_B = 394.6$ K) for bismuth. Due to its exponential dependence with the temperature, the Orbach process only dominates at higher temperatures (above 6 K for phosphorus and 26 K for

bismuth) [Cas67].

Figure 3.10 gives the temperature dependence of electron T_1 for Si:P, together with the contribution of the different processes (dashed lines), as described above. Each of the mechanisms dominates at different temperature ranges: direct (green), Raman (pink) and Orbach (blue). The red solid line in Figure gives the fit to the experimental data as given by Equation 3.41 (data from [Cas63]).

The coherence of the spin states is essential for quantum information applications using donor spins in silicon. The loss of coherence is characterised by the transverse relaxation time, T_2. Although at higher temperatures (> 10 K) T_2 usually follows T_1, at lower temperatures it may be limited by additional decoherence mechanisms [TTM$^+$12]. The coherence time of shallow donors in natural silicon is known to be dominated by a decoherence mechanism that involves the flip-flop of ^{29}Si nuclear spins, namely spectral diffusion. Natural silicon contains about 4.7 % of ^{29}Si, which has a nuclear spin 1/2.

The spectral diffusion can be reduced by isotopic purification of silicon: reducing the concentration of ^{29}Si down to 50 ppm, T_2 as long as 0.45 s for phosphorous [TTM$^+$12] and 2.7 s for bismuth [WTG$^+$13] have been measured, however typically other mechanisms limit T_2 to shorter times.

In ^{28}Si and at low temperature and at low donor concentrations (below $\sim 10^{16}$ cm^{-3}), T_2 is limited by dipole coupling between electron spins which are not refocussed by the Hahn echo sequence, a mechanism termed instantaneous diffusion (ID) [TTM$^+$12, WST$^+$12b]. This effect can be mitigated by reducing the angle of the θ_2 pulse in the Hahn echo sequence ($\pi/2 - \tau - \theta_2 - \tau -$ echo) [SJ01, TTM$^+$12], providing both a measure of donor concentration, as well as a value of T_2 in the absence of ID. In

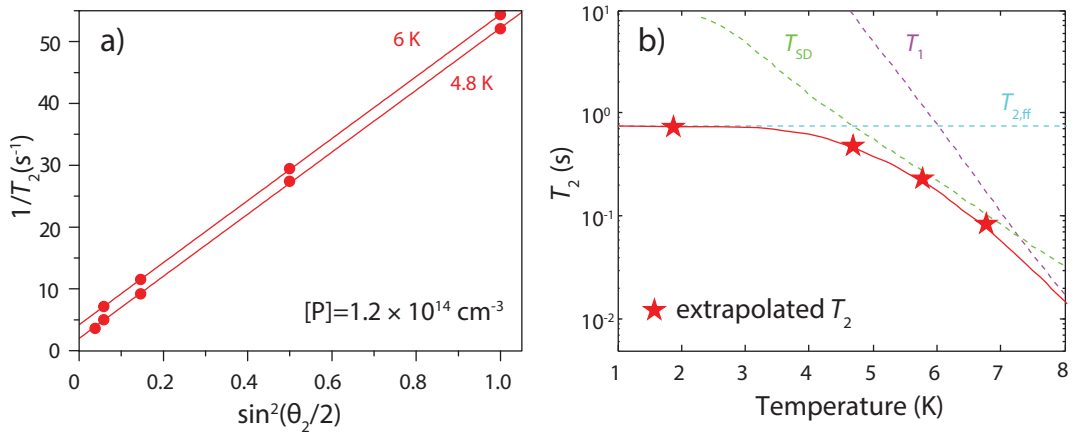


Figure 3.11.: **Extrapolated T_2 by suppression of instantaneous diffusion in ^{28}Si:P at $B \sim 0.34$ T:** a) Experimental $1/T_2$ for phosphorus donor in ^{28}Si as a function of the rotation angle θ_2 at 6 K and 4.8 K. The intercept of the linear fit gives the extrapolated T_2 corresponding to the suppression of the instantaneous diffusion at $\theta_2 = 0$. The slope of the fit correlates to the concentration of P (1.2×10^{14} cm^{-3}. Data from [TTM$^+$12]. b) Temperature dependence of extrapolated T_2. The value of T_2 is limited by T_1 above ~8 K. Below this temperature, the extrapolated value of T_2 (in the absence of ID) can be well described by a combination of spectral diffusion arising from T_1-induced spin flips of neighbouring Se$^+$ spins, combined with the temperature-independent mechanism due to spin flip-flop.

this case the extrapolated T_2 ($T_{2,\mathrm{ext}}$) can be calculated from the equation:

$$\frac{1}{T_2} = \frac{5}{2}\frac{\mu_0}{4\pi}\frac{(g\beta)^2}{\hbar}\frac{[D]}{2}\sin^2\left(\frac{\theta_2}{2}\right) + \frac{1}{T_{2,\mathrm{ext}}}. \tag{3.42}$$

where [D] is the concentration of donor spins resonant with the ESR pulses.

Figure 3.11 (a) illustrates the calculation of $T_{2,\mathrm{ext}}$ via suppression of instantaneous diffusion for phosphorous donors in ^{28}Si (data from [TTM$^+$12]). The slope of the fit gives the concentration of P (1.2×10^{14} cm^{-3}) and the intercept of the linear fit (for $\theta_2 = 0$) gives the extrapolated T_2.

The temperature dependence of $T_{2,\mathrm{ext}}$ at low donor concentrations (below $\sim 10^{16}$ cm^{-3}) can be then described by a combination two additional mechanisms: (1) spectral diffusion arising from T_1-induced spin flips of neighbouring spins and (2) a temperature-

independent mechanism due to spin flip-flops. The contribution of spectral diffusion results in Gaussian decay of the form

$$V(\tau) \propto \exp[-(2\tau/T_{SD})^2] \tag{3.43}$$

where T_{SD} depends both on T_1 and the donor concentration [D] given by

$$\frac{1}{T_{SD}^2} = \frac{\mu_0}{18\sqrt{3}} \frac{(g\beta)^2}{\hbar} \frac{[\mathrm{D}]}{T_1}. \tag{3.44}$$

The effect of spin flip-flop is temperature-independent and the echo decay has an exponential decay given by equation

$$V(\tau) \propto \exp[-2\tau/T_{\mathrm{ff}}] \tag{3.45}$$

where T_{ff} only depends on the donor concentration. Below a certain temperature, when the spin relaxation time T_1 become long, the effect of indirect flip-flops become dominant.

Figure 3.11 (b) gives the temperature dependence (red solid line) of the extrapolated T_2 for Si:P with [P]=1.2×10^{14} cm^{-3} (Data from [TTM$^+$12]). The value of $T_{2,\mathrm{ext}}$ is calculated as combined effect of three mechanisms. (1) T_1 spin relaxation dominates above ∼8 K (pink dashed line). (2) Spectral diffusion (T_{SD}) arises from T_1-induced spin flips (green dashed line) and the echo has a Gaussian decay. (3) A temperature-independent mechanism, due to spin flip-flops (T_{ff}), limits $T_{2,\mathrm{ext}}$ to about 0.45 s, (blue dashed line).

CHAPTER 4

Electron spin resonance

Electron spin resonance (ESR) is the experimental technique used in this thesis to measure the spin properties of donors in silicon. This technique was first used in 1945 [Zav45] and it is based on microwave resonant detection of unpaired electrons. The development of pulsed-ESR and the Hahn echo techniques allowed the measurement of electron spin decoherence (independently of sample inhomogeneities) and gave an incredible contribution to the understanding of the structure and dynamics of many paramagnetic species [SJ01]. The basic principals of ESR are described in this Chapter. In particular, we discuss the experimental instrumentation and the methods used in the experiments of the following Chapters.

4.1. The phenomenon of spin resonance

The physical phenomenon of spin resonance arises from the interaction of the intrinsic angular momentum with external magnetic fields. An isolated electron spin in a static magnetic field, for example, is described by the Hamiltonian introduced in Equation 3.23. The energy separation between its spin levels ($\hbar\omega_e$) is then proportional to the magnetic field intensity.

Therefore, a transition from the electron spin ground state to its excited state can be achieved by the absorption of a photon with frequency ω_e. This observation is the fundamental principal of ESR and it can be obtained experimentally with the application of microwave radiation with a polarisation perpendicular to the static magnetic field.

In an ESR experiment at X-band, the microwave frequency of 9.7 GHz corresponds to a magnetic field of about 0.35 T (for $g \approx 2$). A typical X-band spectrometer is shown in Figure 4.1. Spin resonance transitions are measured with this instrument by detecting microwaves re-emitted through their coherent emission to the microwave cavity. The details of this experimental set-up are described in Section 4.4.

The *low* sensitivity of the microwave detectors currently used requires a large number of spins to make possible the measurements. Therefore, experiments at X-band, for example, are usually carried out with an a ensemble of at least 10^{10} spins.

Thermal equilibrium of the ensemble is also crucial. For example, if the spins are equally distributed among the two states, there is no emitted signal.

Boltzmann statistics gives the ensemble state at thermal equilibrium. At a temper-



Figure 4.1.: **Bruker ElexSys E680 spectrometer at the Centre for Advanced Electron Spin Resonance (CAESR), University of Oxford**

ature T, for instance, this condition is given by the state

$$\rho^{\mathrm{eq}} = \frac{1}{\mathcal{Z}} \begin{pmatrix} 1 & 0 \\ 0 & \alpha \end{pmatrix} \tag{4.1}$$

where we define $\alpha = \exp\{-\omega_e/k_B T\}$ and $\mathcal{Z} = 1 + \alpha$.

The signal intensity of an ESR experiment is therefore proportional to the difference between the number of down spins (ρ_{11}) and up spins (ρ_{22}). We then define the so called *spin polarisation* given by

$$\mathcal{P} = \frac{n_\downarrow - n_\uparrow}{n_\downarrow + n_\uparrow} = \frac{1-\alpha}{1+\alpha} \tag{4.2}$$

where $n_\downarrow = \rho_{11}^{\mathrm{eq}}$ and $n_\uparrow = \rho_{22}^{\mathrm{eq}}$ are the concentration of spin up and down respectively. For instance at the magnetic field of the order of 0.3 T and at LHe temperature (4.2 K), the electron spin polarisation is about 5.5%.

4.2. Time evolution of a spin system

In this Section, we introduce a formal derivation of the spin resonance phenomenon for an isolated electron spin. Even though this derivation does not include the interaction with nuclear spins, most results can be generalised.

Given an ensemble of electron spins in a arbitrary state $\rho(0)$ and under a static magnetic field ($\boldsymbol{B} = (0, 0, B)$), the time evolution of ρ can be calculated by using the Liouville-von Neumann equation

$$\frac{d\rho(t)}{dt} = -i[\mathcal{H}_{EZ}, \rho(0)] \tag{4.3}$$

where $\mathcal{H}_{EZ}$ is given by Equation 3.23.

The Liouville-von Neumann equation obtained is the quantum mechanical equivalent to the equation for the dynamic of a magnetic moment under a magnetic field which leeds to the so called *Bloch equations*:

$$\hbar\frac{d\boldsymbol{S}(t)}{dt} = \boldsymbol{\mu} \times \boldsymbol{B}. \tag{4.4}$$

The solution of $\boldsymbol{S}$ from this equation gives the same results of the quantum expectation values $\langle \boldsymbol{S} \rangle$ obtained from Equation 4.3.

Because $\mathcal{H}_{EZ}$ is time-independent, the solution of the Liouville-von Neumann equation can been written as

$$\rho(t) = \mathcal{U}(t)\rho(0)\mathcal{U}^{\dagger}(t) \tag{4.5}$$

where $\mathcal{U}(t) = \exp(-i\omega_e\sigma_z t/2)$ is the time evolution operator. The time evolution of a spin under a static magnetic field gives a precession around the z-direction with frequency ω_e. In this representation, the expectation value of the projections of the

spin operator can be calculated as $\langle S_i \rangle(t) = \mathrm{Tr}(\rho(t) S_i)$ with $i = x, y, z$.

If we now consider the combined effect of a static magnetic field B_0 along the z-direct with a time-dependent field $B_1 = \cos(\omega_{\mathrm{mw}} t + \phi)$ on the x-direction, we obtain the Hamiltonian

$$\mathcal{H} = \mathcal{H}_{EZ} + \Omega \cos(\omega_{\mathrm{mw}} t + \phi) S_x \tag{4.6}$$

where we define $\Omega = g_e \beta B_1 / \hbar$.

The Liouville-von Neumann equation for the Hamiltonian in Eq. 4.6 cannot be directly integrated because it is now time-dependent. In order to find a time-independent approximation of Eq. 4.6, we use the unitary transformation given by the operator

$$U = \exp\left(i \omega_e S_z t\right). \tag{4.7}$$

This transformation moves the reference frame into a frame that rotates together with the solutions of the Zeeman Hamiltonian (i.e. *rotating frame*) and effectively removes the time-dependence from Equation 4.6. The representation obtained under this transformation is therefore equivalent to the so called *interaction* representation.

In the rotating frame, we obtain a new Liouville-von Neumann equation, which reads

$$\frac{d\tilde{\rho}(t)}{dt} = -i[\tilde{\mathcal{H}}, \tilde{\rho}(0)] \tag{4.8}$$

where we define $\tilde{\rho} = U \rho U^{\dagger}$ and the transformed Hamiltonian is

$$\tilde{\mathcal{H}} \approx \frac{\Omega}{2} [\cos(\phi) S_x + \sin(\phi) S_y]. \tag{4.9}$$

The transformation of the Hamiltonian in the rotating frame is derived in Appendix

A. The Equation 4.9 gives an effective Zeeman Hamiltonian, where the effective magnetic field is oriented in a direction on the xy-plane which is set by ϕ. The solution of Equation 4.8 is a precession around this axis.

In a pulsed-ESR experiment, an arbitrary rotation with angle θ, around an axis in the xy-plane set by ϕ, can be then achieved applying a pulse with the magnetic field strength (B_1) and the pulse duration (T_{pulse}) chosen such that

$$\theta = \frac{\Omega}{2} T_{\text{pulse}}. \tag{4.10}$$

4.3. Measurement of spin relaxation and coherence

Pulse-ESR techniques allow the manipulation of an ensemble of donor electron spins into an arbitrary state by the application of a specific sequence of rotations around the x and y axes, following the approach described in the previous Section.

If all the spins are initially in the ground state $\rho = |-1/2\rangle \langle -1/2|$, for example, by applying an on-resonance pulse with $\theta = \pi/2$ around the x-axis ($\phi = 0$), we orient the spins into the y-direction. When the microwaves are removed, the spins then start to process around the z-axis.

However, in a real experiment the spins will return back to the thermal equilibrium condition defined by Eq. 4.1, due to their interaction with the environment. The relaxation processes (T_1 and T_2), due to this interaction, have been described in Chapter 3. In this Section, we introduce the pulsed-EPR techniques used to measure them experimentally.

Free induction decay

The simplest pulsed-ESR experiment involves only the application of an on-resonance ($\pi/2$) pulse. As the pulse is applied, the spins start an in-phase precession on the xy-plane. Due to the interaction with the environment, the spins lose their coherence.

A measure of this process gives the so called *free induction decay* (FID). If the spin are in inhomogeneously broadened, by an inhomogeneous field for example, the decoherence measured by the free induction decay (T_2^*) is shorter than the intrinsic T_2.

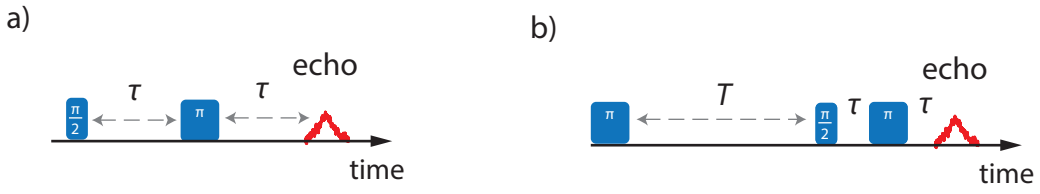


Figure 4.2.: **Schematic pulse sequences used to measure electron spin T_2 (a) and T_1 (b).**

The Hahn echo (T_2)

The Hahn echo technique is introduced to measure spin decoherence independently of the inhomogeneous broadening, based on the principle that whatever the source of this broadening, it is quasi-static.

By applying a $(\pi/2)$ pulse along the x-direction, each spin starts to acquire a phase φ which is proportional to its energy shift. If a time τ after the first pulse, we apply a second pulse with $(\theta = \pi)$, we rotate the spins of 180° and effectively we invert the spin rotation.

Because the spin always keeps the same energy shift, after a time τ each spin will now acquire a phase $-\varphi$, which compensates the one acquired in the first period. After a time 2π from the first pulse, the spins will then refocus, giving the so called *echo* signal.

The pulse sequence used to measure the electron T_2 is shown in Figure 4.2 (a). We measure the Hahn echo decay by acquiring the echo and varying τ in the sequence $(\pi/2 - \tau - \pi - \tau - \text{echo})$.

The inversion recovery (T_1)

The electron spin relaxation time T_1 is measured by applying the pulse sequence ($\pi - T - \pi/2 - \tau - \pi - \tau -$ echo), as show in Figure 4.2 (b). By first applying a π-pulse the spin polarisation of the electron spin is inverted with a consequent change in the sign of echo. Due to the interaction with the environment, the spins relax back to thermal equilibrium. If we acquire the echo, varying the time T, we obtain an echo decay with a sign inversion which gives a measure of T_1.

4.4. ESR setup

ESR measurements of this thesis have been carried out with the Bruker ElexSys spectrometers at University College London (UCL) and at Centre for Advanced Electron Spin Resonance (CAESR), University of Oxford (Figure 4.1).

In the ESR setup, the sample is placed in a cylindric microwave resonator with an inner diameter of about 5 mm (MD5). The cavity is then coupled to a microwave antenna for emission and detection and it has a tuneable quality factor up to 20000.

The cavity is kept inside an Oxford Instrument flow cryostat for cooling. This system allows temperature dependent measurement down to the temperature of liquid helium (LHe), which is about 4.2 K.

The sample inside the cavity is positioned at the centre of the Helmholtz coils of an electromagnet that generates the static magnetic field, controlled by the ElexSys and it can be varied up to about 1 T.

The microwaves (mw) are generated by a source in the microwave bridge. The signal is then split into two components. One of them is sent to the sample and the other one is used as reference. The reflected mw goes to a circulator and it is then detected by a Schottky diode in the bridge.

In a cw-ESR experiment, the reflected mw are measured as a function of the magnetic field. In order to improve the signal-to-noise, the magnetic field is modulated at a modulation frequency (f_{mod}), usually in the range $f_{\mathrm{mod}} = 10 - 100$ kHz. The ESR signal is then demodulated and converted by the ElexSys.

In a pulsed-ESR experiment, the mw are pulsed and amplified by a TWT amplifier to

about ∼1 kW. The ElexSys spectrometer allows pulse generation with a resolution of 1 ns. The electron spin echo signal is acquired by an internal oscilloscope and it is converted to a digital signal.

CHAPTER 5

Electric field ionisation and Stark Shift of arsenic donors

Charge state control of donors by electric fields has been suggested since early proposals for silicon-based quantum information architectures [Kan98]. However only a few experimental results have been achieved so far in this direction and up to date measurements of ionised donors have mainly relied on optical or thermal ionisation processes [SSS$^+$13, DHSB12].

In this Chapter, we exploit electric-field charge state manipulation of arsenic donors in 28-silicon. We develop a parallel-plate capacitor-like structure for the application of a uniform electric field to an ensemble of ^{75}As donors designed to be measured by electron spin resonance (ESR). ESR detection of donor spins allows, in principle, a measure of their relative charge states by comparing the relative spin resonance

signal under applied electric fields. The uniform field distribution also allows us to get a precise measurements of the Stark shift parameter as long as the field strength is below the ionisation threshold.

Selected results from this Chapter are published in

[LSL+14] C. C. Lo, S. Simmons, R. Lo Nardo, C. D. Weis, A. M. Tyryshkin, J. Meijer, D. Rogalla, S. A. Lyon, L. Bokor, T. Schenkel and J. J. L. Morton, *Stark shift and field ionization of arsenic donors in 28 Si-silicon-on-insulator structures.* Appl. Phys. Lett. **104**, 193502 (2014).

5.1. Materials and characterisation

Donor ionisation in silicon requires an electric field of a few $\sim$ V/μm [PWU$^+$14]. Therefore, a parallel-plate capacitor of a typical wafer thickness of 500 μm, has to be biased with a voltage higher then 1000 V in order to achieve donor field ionisation. In order to reduce the required voltage, we developed a silicon-on-insulator (SOI) device where we created a back gate by high energy donor implantation at 5 μm below the surface.

The device design allows the application of uniform and large electric fields across the SOI layer for both Stark shift measurements and controlled ionisation of the dopants. This provides a platform for ensemble ESR measurements on electrically ionised and re-neutralised donor spins. The devices measured in this Chapter was designed and fabricated by C. C. Lo at Lawrence Berkley National Laboratory, USA.

ESR measurements of the SOI device were carried out at the Centre for Advanced Electron Spin Resonance (CAESR), University of Oxford. The experimental setup is described in Figure 5.1. The device is inserted in a mw cavity and connected to a pulse generator. The ESR spectrometer and the pulse generator are then connected to a trigger to synchronised the voltage pulses with the ESR detection.

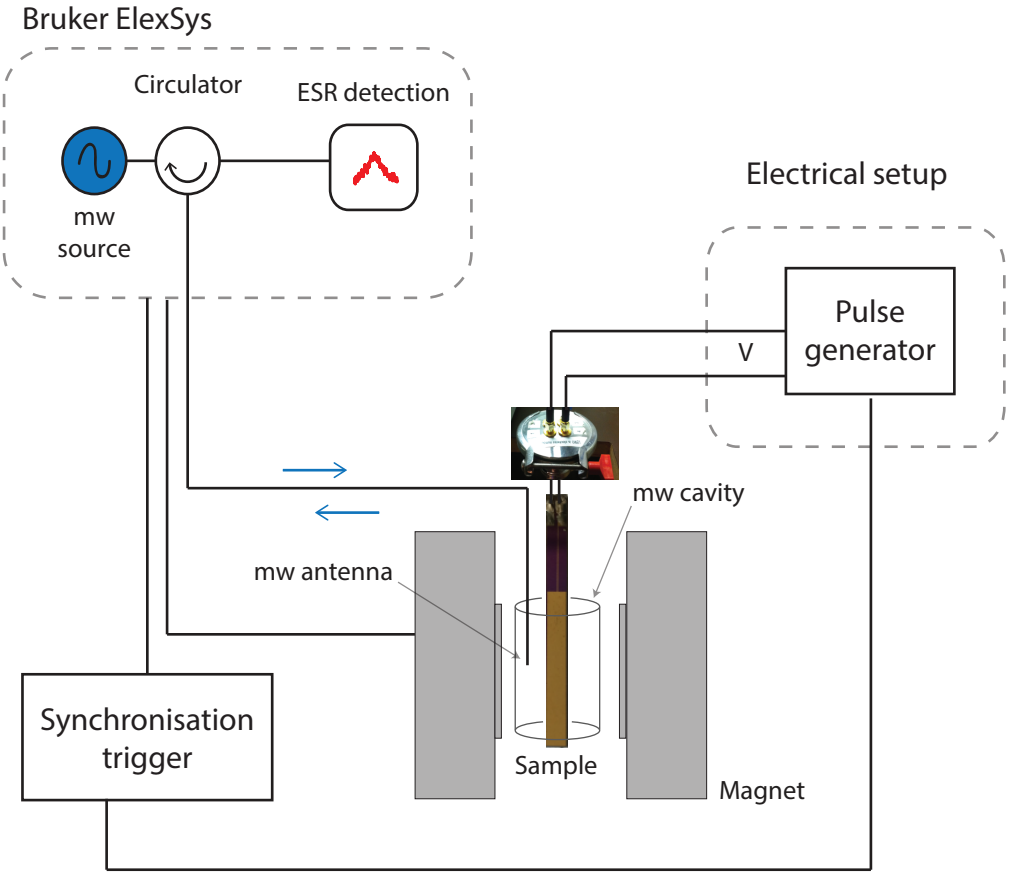


Figure 5.1.: **Schematics of experimental setup used for the electrical charge state manipulation of arsenic in the SOI device:** Bruker Elexsys spectrometer at X-band (9.7 GHz) at the Centre for Advanced Electron Spin Resonance (CAESR), University of Oxford. The instrumentation in Figure is used to synchronise the ESR with the electrical pulses.

Device design and fabrication

The SOI substrates consisted of 100 nm thick p-doped ($\sim 10\,\Omega$cm) natural silicon (^{nat}Si) with $\langle 100 \rangle$ orientation (SOITEC), and a similarly p-doped ($\sim 15\,\Omega$cm) handle wafer underneath whose conductivity normally freezes out at cryogenic temperatures. 100 nm thick isotopically purified 99.92% 28-silicon (^{28}Si) was epitaxially grown on the natural silicon SOI wafer (Lawrence Semiconductors), forming the ^{28}Si-SOI device layer.

In order to create an effective back-gate for realising a parallel plate geometry, a high energy boron (B) implantation of 4 MeV at a dose of 2.2×10^{15} cm^2 was performed, with almost all dopants implanted through the device and the 200 nm thick buried oxide (BOX) layers, peaking at 5 μm down from the handle wafer-buried oxide interface. The peak B concentration of 3×10^{19} cm^3 is above the metal-insulator-transition, ensuring that the $p+$ region in the handle wafers remains metallic even at cryogenic temperatures.

The added B concentration in the SOI layer resulting from the high energy implant is expected to be less than 1×10^{15} cm^3 from device process simulations, and the lattice damage in the SOI layer is expected to be minimal due to ion channeling and most lattice damage is expected to be incurred at end-of-range.

A 10 nm silicon oxide was subsequently grown on the SOI layer by dry oxidation at 900°C. This oxidation step activated the implanted B and also reduced lattice damage in the handle wafer induced by the MeV implants.

The ^{28}Si-SOI layer was then implanted with arsenic dopants (^{75}As) at 110 keV at a dose of 4×10^{11} cm^2 with 7° tilt. Arsenic was chosen to minimise dopant diffusion from the ^{28}Si layer to the natural silicon layer during thermal activation. In addition,

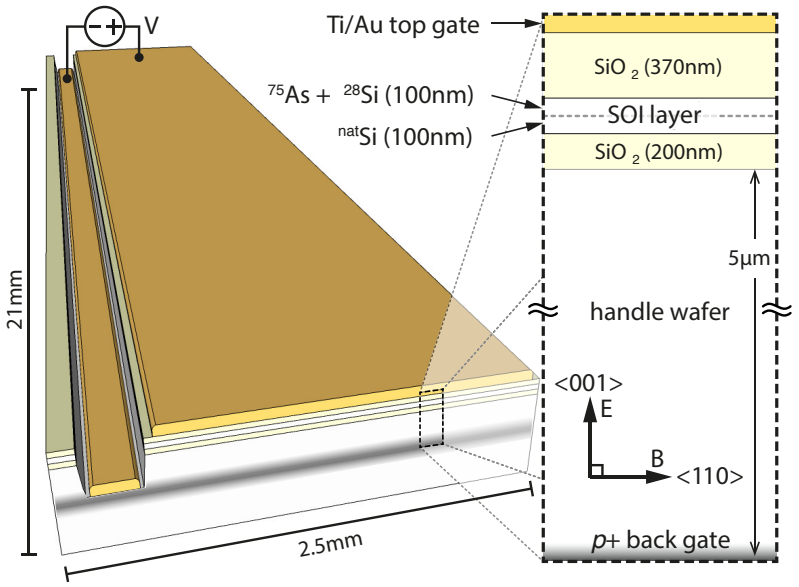


Figure 5.2.: **Schematic of the ^{28}Si-SOI device:** The ^{75}As donors reside in the epitaxially grown ^{28}Si region of the SOI layer. The $p+$ back gate is formed by MeV ion implantation. Inset: Cross-section of the device.

the As nuclear spin of $I = 3/2$ allows the clear elucidation of the contribution from the contact hyperfine induced Stark shift.

The resulting peak donor concentration is located approximately 60 nm away from the dry oxide-SOI layer interface. 360 nm of low temperature oxide was subsequently deposited at 450°C to reduce the probability of gate leakage in the large-area device required for ensemble measurements.

The dopants were then activated by rapid thermal annealing at 900°C for 10 s in a nitrogen atmosphere. We found significant dopant pile up towards the dry oxide as measured by secondary ion mass spectroscopy, which shows an As concentration of $4 - 5 \times 10^{16}$ cm^3 in the top 50 nm of the ^{28}Si epitaxial layer but drops to $\approx 1 \times 10^{15}$ cm^3 at the $^{\text{nat}}$Si-BOX interface, hence 90% of the implanted donors

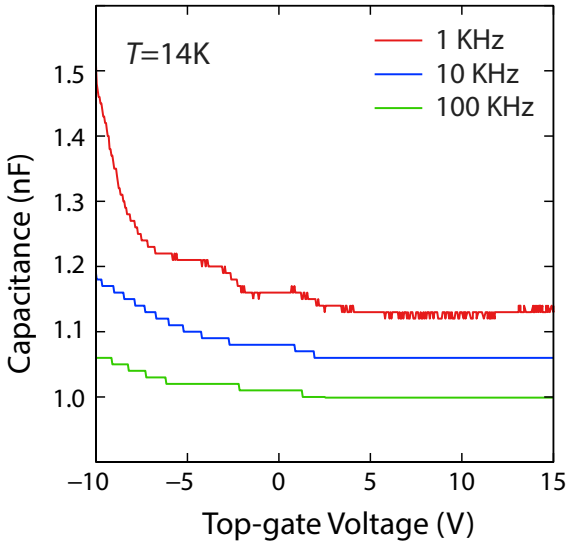


Figure 5.3.: **CV measurement of the device.** Above a gate voltage of −2 V the capacitance is constant. Below this gate voltage due to hole accumulation the at the handle wafer-BOX interface the value of the capacitance increases.

reside in the ^{28}Si layer.

In order to access the deeply implanted $p+$ back gate in the handle wafer, contact windows were made by etching through the oxide layers and SOI layer. A Bosch etch process was then carried out to etch 5 μm down the handle wafer. After native oxide removal by hydrofluoric acid, Ti/Au metallic layers were subsequently deposited to form both the contacts to the $p+$ back gate and define the top gate electrode.

The top gate electrode covers an area of 21×2.6 mm^2 with approximately 2×10^{11} donors underneath. A forming gas anneal (90% N_2, 10% H_2) at 350°C for 20 minutes was then carried out to passivate the silicon-silicon dioxide interfaces in the structure. A schematic and the cross section of the final device structure are shown in Figure 5.2.

CV measurements

Capacitance-voltage (CV) measurement at 14 K are shown in Figure 5.3 for different frequencies, showing a constant capacitance above -2 V. The capacitance of about 1 nF corresponds to 1.9 nF/cm^2, given the device dimensions of 21×2.5 mm.

Considering that the silicon permittivity is $\epsilon_{\mathrm{Si}} = 0.1$ nF/m, the device capacitance measurements are in good agreement with the geometry of the device with the top 5 μm of the silicon handle wafer being insulating. Below a gate voltage of -2 V, the capacitance of the device increase due to accumulation of holes at the interface.

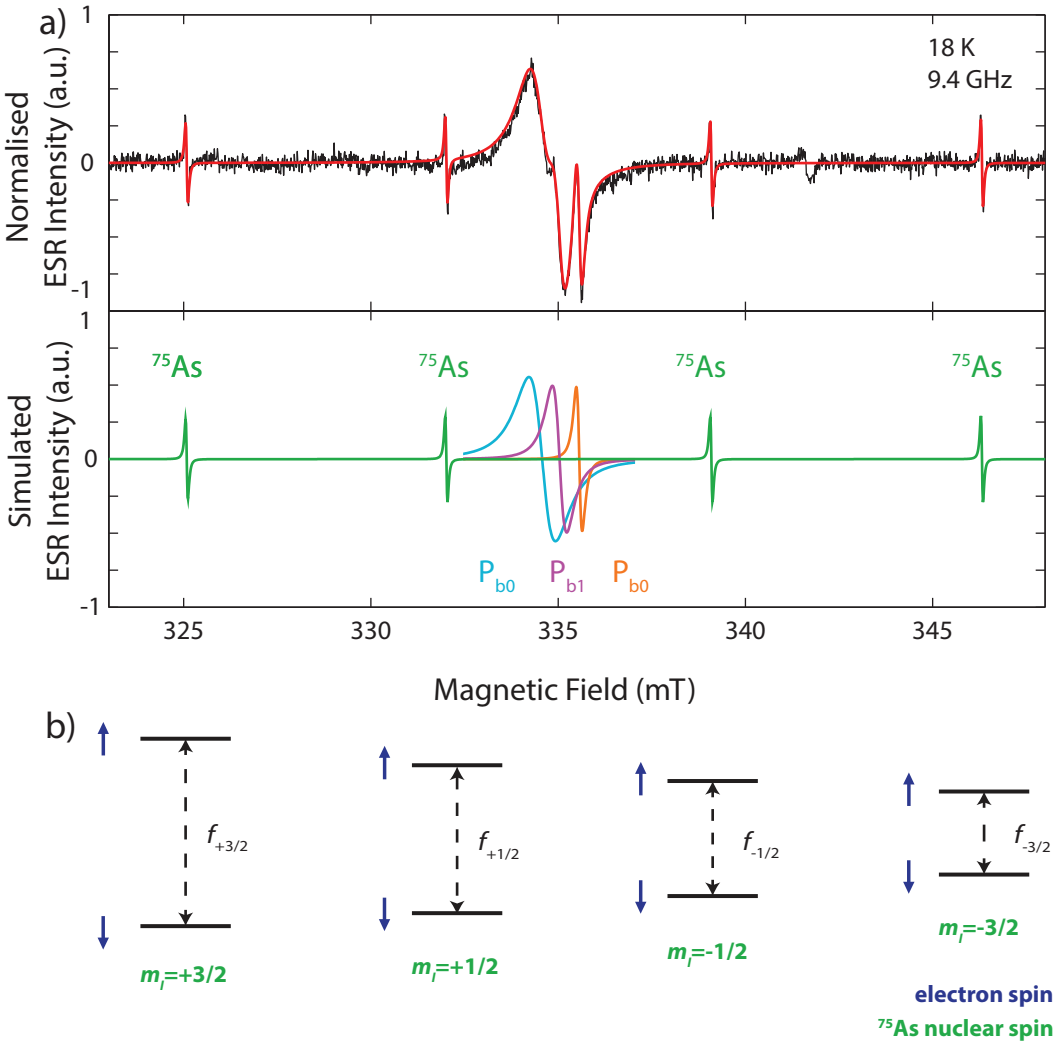


Figure 5.4.: **Cw-ESR spectrum and energy levels of the electron-nuclear spin Hamiltonian for ^{75}As, where $I = 3/2$ and in the high field limit $\omega_e \gg A$.** (a) ESR spectrum of the device at 18 K at X-band. The four narrow lines are relative to the ^{75}As. The central lines arise from different defects at the Si/SiO_2 interface as indicated in Figure. (b) Energy levels of the ^{75}As. The dashed lines represents ESR allowed transitions, that each correspond to a particular nuclear spin state m_I.

ESR characterisation

The devices were characterised by continuous wave ESR measurements with a Bruker Elexsys spectrometer at X-band (∼9.7 GHz) and at a magnetic field of ∼0.34 T. A typical cw-ESR spectra measured at 18 K is shown in Figure 5.4 (a). The four hyperfine lines separated by 7.1 mT are due to the resonance transitions of the ^{75}As, with $I = 3/2$.

The values of $g = 1.99837$ and $A = 198.35$ MHz, obtained from the spectrum, agree with previous reported values [Feh59]. However, an ESR linewidth of 0.01 mT (0.3 MHz) is observed for the As donor at 20 K, a factor of ∼40 narrower than the known linewidth in ^{nat}Si [Feh59].

The central resonance of the spectra (at $g \sim 2$) is best fit by a superposition of three Lorentzian derivative lines, as shown in Figure 5.4. These resonance transitions arises from different defects at the Si/SiO_2 interface (P_b centres) [KYK00].

In addition, we measured the electron spin relaxation time T_1 to exclude the effect of nearby charges. The experimental results, obtained by inversion recovery are shown in Figure 5.5 (a). The fit in Figure is obtained from Equation 3.41. Below 12 K, the electron spin relaxation time is limited by the Raman process, and we obtain $C = 2 \times 10^{-8}$ s^{-1}K^9. Above this temperature the Orbach became dominant and we have $D = 7 \times 10^{10}$ s^{-1}.

We also obtained an electron spin coherence time $T_2 = 0.3$ ms at 2 K. Figure 5.5 (b) gives the experimental decay of T_2 obtained varying τ in the sequence ($\pi/2 - \tau - \pi -$ echo). The value of T_2 suggests that the electron spin coherence time is limited by instantaneous diffusion through dipole-dipole interactions between donor spins at concentrations of 4×10^{16} cm^{-3} [TTM$^+$12].

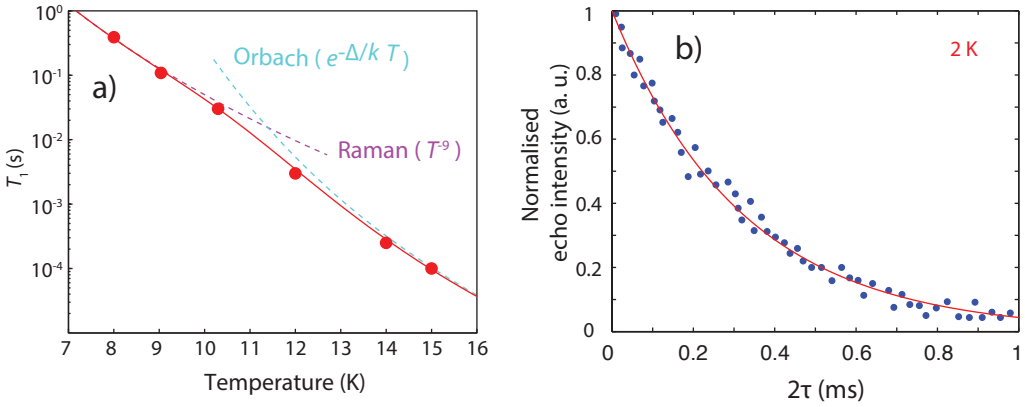


Figure 5.5.: **Experimental relaxation times of ^{75}As in the SOI device:** (a) Temperature dependence of the electron T_1. Blue dots are experimental data. Red curve is the fit using Equation 3.41. (b) T_2 decay at 2 K. The pulse sequence used to measured T_1 (a) and T_2 (b) are described in Section 4.3.

The linewidth of the resonant transitions and spin coherence time T_2 confirm that the signal mostly arises from dopants residing in the ^{28}Si layer and that the SOI layer has a low defect density.

5.2. Stark shift of resonance frequency

The parallel plate geometry of the device permits the application of a uniform electric field to the arsenic donor in SOI layer. Under an electric field below the ionisation threshold, the donors remain neutral but their electron wavefunctions are distorted due to the Stark effect (as described in Section 3.4).

In this Section, we present the first measurement of the Stark effect for arsenic donor in silicon. The Stark effect can be quantified by the shift of the resonance frequency $\Delta f(E, m_I)$ measured experimentally by ESR under a uniform electric field, as previously reported for Si:Sb [BTS$^+$06]. The shift in resonance frequency can be then related to the parameters η_a and η_g, defined in Section 3.4.

Theoretical estimates of the Stark effect [RWB$^+$07, PWU$^+$14] and previous experimental results [BTS$^+$06] suggest the expected shift in frequency to be of the order of ~ 50 KHz at 0.3 V/μm. This frequency shift cannot be detected by cw-ESR because it is less then the inhomogeneous broadening of the ESR linewidth: 0.01 mT (0.3 MHz). Therefore, we use Hahn echo pulse sequence detecting the frequency shift by measuring the echo phase as a function of the applied electric field [BTS$^+$06].

The Hahn echo detection is more sensitive to small resonance shifts (as it is limited by $1/T_2$ rather then $1/T_2^*$). The experiment is based on the application of a voltage pulse during the defocussing period of the standard spin echo sequence as described in Figure 5.6. In a regular Hahn echo experiment, a first microwave pulse $(\pi/2)_{mw}$ rotates the spins into the plane perpendicular to the magnetic field B_0. The spin will then process at different frequencies due to their local environment (defocusing). After a time τ a second pulse $(\pi)_{mw}$ rotate the spins inverting the rotation. Assuming

each spin maintains its own frequency at all times, at a time 2τ all the spin are refocused forming an echo.

When a voltage pulse is applied only during the defocussing period of the Hahn echo, the spins acquire a phase shift due a global change in frequency that it is not refocussed in the second period of the sequence. This uncompensated phase can be defined for each m_I transition as

$$\Delta\phi(E, m_I) = \phi(E, m_I) - \phi(E = 0, m_I), \tag{5.1}$$

and can be related to the frequency shift as

$$\Delta\phi(E, m_I) = 2\pi\Delta f(E, m_I) \times \tau_E \tag{5.2}$$

where τ_E is the duration of the voltage pulse.

In the device structure described in Figure 5.2, we expect the local strain and localised charges at the Si/SiO_2 interface to affect the measurement of the Stark shift [BTS+06]. The presence of a local internal field (E_{in}) can be seen as a linear contribution in the shift dependence with the external field (E_{ex}). As we discussed in Section 3.4, we expect the Stark shift to be proportional to the square of the electric field and we have

$$\Delta f \propto (E_{ex} + E_{in})^2 = E_{ex}^2 + 2E_{ex}E_{in} + E_{in}^2. \tag{5.3}$$

A linear component of the Stark effect is thus expected to arise from local inhomogeneity, resulting in a decay of the electron spin signal [BTS+06]. In order to avoid this contribution, we applied a bipolar voltage pulse (positive and negative) as shown in Figure 5.6.

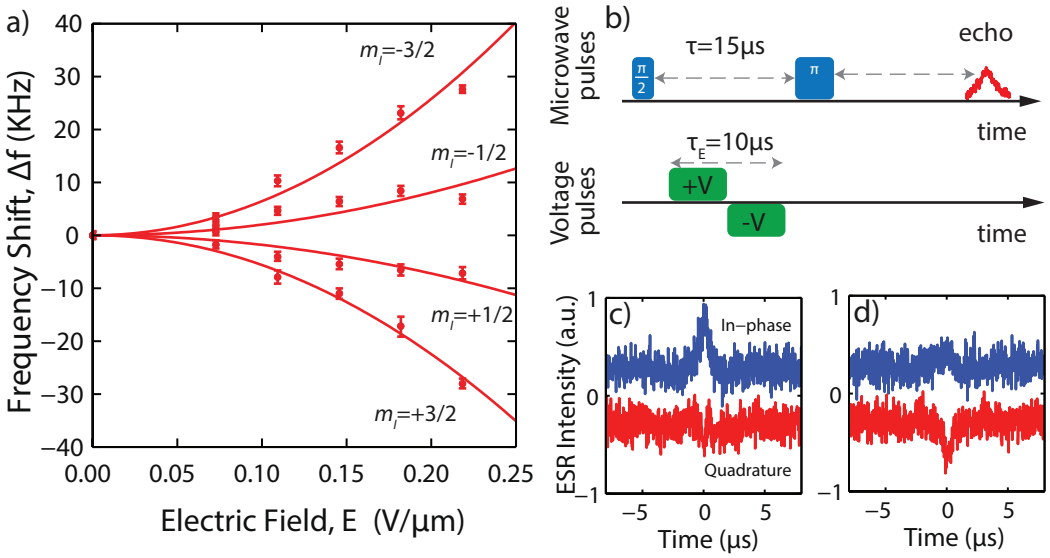


Figure 5.6.: **Stark shift of the resonance frequency for the four ESR lines of Si:As and pulse sequence used in Stark shift experiment.** (a) The different ESR lines m_I have a different resonance shift according to Equation 5.4. Error bars indicate 95% confidence bounds in fitting the phase shift of the echo. Solid lines represent the fit using Equation 5.4. (b) Synchronisation of the voltage (electric field) with the microwave pulses for the Hahn echo sequence. (c) Hahn echo for the $m_I = +3/2$ ESR transition of arsenic donors. (d) Hahn echo of the same transition under an applied electric field of $E = 0.22$ V/μm. The phase shift due to the application of the electric field is $\Delta\phi = 108°$.

All measurements were carried out with microwave pulse delays of $\tau = 15$ μs, and the voltage pulses for each polarity are 5 μs long (total $\tau_E = 10$ μs voltage pulse for each measurement). A two step phase cycling (+X,+X and +X,−X) for the microwave pulses is used to remove spurious background signals.

Figure 5.6 (c,d) show that an electric field of $E = 0.22$ V/μm is sufficient to set a phase shift of $\Delta\phi = 108°$ across the $m_I = +3/2$ ESR transition. All phase shifts extracted from the echo signals for the four different hyperfine-split lines are converted to frequency shifts following Equation 5.2 and are shown in Figure 5.6. The solid lines represent quadratic fits to the data as defined by

$$\Delta f(E, m_I) = \eta_g E^2 \frac{g\beta B_0}{\hbar} + \eta_a E^2 \frac{m_I A}{\hbar}. \tag{5.4}$$

We find the contact hyperfine term $\eta_a = -1.9 \pm 0.7 \times 10^{-3}\,\mu\mathrm{m}^2/\mathrm{V}^2$ and the spin-orbit term $\eta_g = 5 \pm 15 \times 10^{-6}\,\mu\mathrm{m}^2/\mathrm{V}^2$. The spin-orbit shift is very weak compared with the hyperfine shift under our experimental conditions with relatively moderate magnetic fields [BTS+06, RWB+07], and even its sign cannot be determined accurately within experimental errors. Indeed, fitting the data while neglecting the spin-orbit term results in virtually no change to the contact hyperfine value.

Finally, the measured resonance line width (dominated by inhomogeneous broadening) is here of about 0.3 MHz thanks to the use of ^{28}Si material. This implies that the Stark shift parameter measured suggest that an electric field of the order of $1\,\mathrm{V}/\mu\mathrm{m}$ is sufficient for shifting an entire ESR line out of resonance, similar to the value suggested by Bradbury *et al.* [BTS+06].

5.3. Electric field induced donor ionisation and neutralisation

ESR detection of field induced donor ionisation has not been demonstrated so far, although it has been suggested since early proposals [Kan98]. The main difficulties are due to the application of a sufficiently strong ($\sim V/\mu m$) and homogeneous electric field to a sufficiently large number of spins to be detected by ESR . The parallel plate geometry of the device used here and the relatively *low* separation between its plates (5 μm) allow us to apply an uniform electric field up a *few* $\sim V/\mu m$ to about 10^{10} donors and to investigate the consequent field ionisation.

At low temperature, all arsenic donors in the ^{28}Si layer of the device are in their neutral state. Under the application of an electric field sufficiently strong to ionise the donors, the electrons tunnel off the impurity sites and move at the Si/SiO_2 interface. Figure 5.7 gives a schematic representation of this process. Removing the electric field, the electron tunnel back to the donors and the neutral condition is re-established (i.e. neutralisation).

Measuring the ESR signal intensity as function of electric field (E), we observed that for $E \gtrsim 2$ V/μm all the donors are completely field-ionised, as shown in Figure 5.8 (a). Removing the electric field causes the ESR signal to reappear as a result of the re-neutralisation of the donors. This experimental result gives us two important insights relevant for silicon-based quantum information applications: (1) a measure of the minimum field strength required for the field-induced electron tunnelling, (2) an upper bound limit for the Stark shift achievable and thus a minimum microwave duration compatible with individual addressability of electron spins.

(1) Electrically induced spin-dependent tunnelling has been suggested as a read-

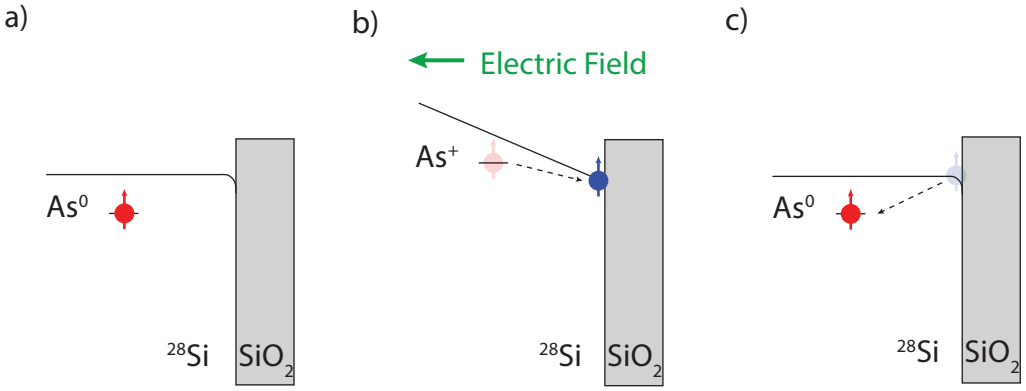


Figure 5.7.: **Schematic of field ionisation of the ^{75}As donors in silicon:** (a) At low temperature, the arsenic donors in the SOI layer are in their neutral state. (b) Applying a voltage above the ionisation threshold forces the electron to tunnel off the donor to the Si/SiO_2 interface (i.e. ionisation). (c) After the voltage is removed, thermal equilibrium is re-established and the electrons move back to donor site (i.e. neutralisation).

out strategy for donor electron spins [MVMB10]. Recent experiments have also demonstrated individual spin read-out via field-induced tunnelling to an SET device [MPZ$^+$10, PTD$^+$12, PTD$^+$13], as described in Section 2.3. The result described here, provides a experimental measurement of the minimum electric field necessary to induce electron tunnelling from the donor site, for Si:As.

(2) As introduced in Section 2.3, one of the strategies suggested for the manipulation of individual spins in a device with a large array of donor is to apply a local electric field to individually shift the resonance frequency of each of donor. The maximum frequency shift that can be achieved depends on the maximum electric field that can be applied before ionisation, as given by Equation 5.4. For Si:As, we obtain a estimate for the maximum Stark shift of each ESR transition given by

$$\Delta f_{max}(m_I) < m_I \times (1 \pm 0.5)\ \text{MHz}. \tag{5.5}$$

This in turn determines how quickly individual electron spins can be manipulated

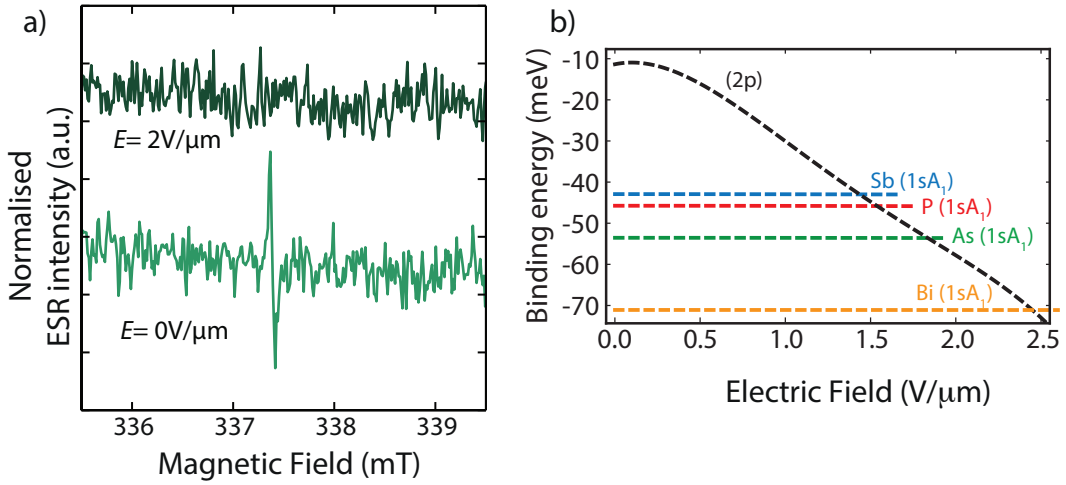


Figure 5.8.: **Electric field ionisation of the ^{75}As and theoretical calculations:** (a) Continuous wave ESR signal of the m_I=+3/2 signal with constant voltage (lower) $E = 0\,\mathrm{V}/\mu\mathrm{m}$ and (upper) $E = 2\,\mathrm{V}/\mu\mathrm{m}$ measured at 18 K, offset for clarity. (b) Theoretical calculation of the ground state and the 2p-state of group-V donors as a function of the electric field. When the energy of the 2p state becames degenerate with the ground state the donor is ionised (Calculations from [PWU$^+$14]).

in Kane-like architecture. In the manipulation of electron spin the microwave pulse length (τ) determines the bandwidth of the excitation. Therefore, if τ is shorter than Δf_{max}^{-1} the excitation also affects those spins that should not be selected because their resonance frequency will also lie within the pulse bandwidth. Following this approach, we obtain for Si:As that $\tau_{min} > 700 \pm 300$ ns.

Recent theoretical calculations of the field ionisation of donors show a good agreement with the results obtained here [PWU$^+$14]. In the last reference, a variational theory approach has been used to quantify the correction to electron wavefunction under a uniform electric field. The electronic ground state of group-V donors has a weak dependence on the external electric field, as shown in Figure 5.8 (b). However, when the electric field is increased, the 2p state becomes degenerate with the ground state and the donor is ionised [PWU$^+$14].

Having determined the minimum electric field necessary to ionise the donors, we

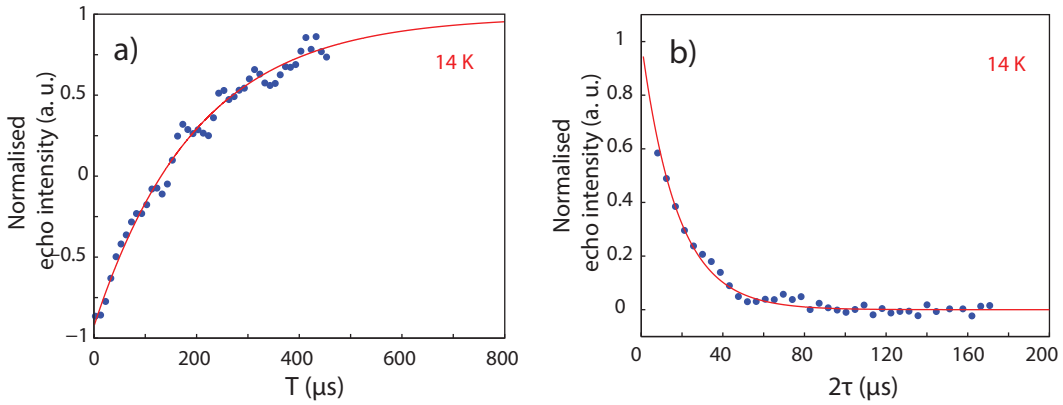


Figure 5.9.: **Experimental relaxation times of ^{75}As in the SOI device at** 14 K**:** The pulse sequence used to measured T_1 (a) and T_2 (b) are described in Section 4.3.

now investigate the dynamics of the ionisation-neutralisation following an electric field pulse, by monitoring the electron spin echo intensity. This technique is based on applying the Hahn echo sequence at different times δ after the voltage pulse V. A similar technique has been previously used for studying donor-acceptor recombination after above band gap illumination [DHW89]. After applying the voltage pulse, the relative concentration of neutral arsenic impurities can be measured using the Hahn echo sequence ($V - \delta - \pi/2 - \tau - \pi - \tau -$ echo).

In order to find the best experimental conditions for the ionisation/neutralisation experiment, we first measured the electron spin relaxation times in our SOI device. The electron spin T_2 is then obtained by varying τ in the sequence ($\pi/2 - \tau - \pi - \tau -$ echo), as discussed in Section 4.3. The experimental decay at 14 K gave $T_2 = 20$ μs and it is shown in Figure 5.9 (b). Electron relaxation time T_1 was measured varying T in the inversion recovery sequence ($\pi - T - \pi/2 - \tau - \pi - \tau -$ echo). A result of $T_1 = 0.2$ ms is shown in Figure 5.9 (a) at the same temperature. Given the electron spin relaxation times, we therefore set an experimental repetition time of 1 ms to allow electron spin relaxation and we set $\tau = 2.5$ μs.

The experimental results of the ionisation/neutralisation dynamics and the relative pulse sequence are shown in Figure 5.10. We measured the echo as a function of δ after an voltage pulse of $\sim$3 V/μm (10 μs) to make sure all donors are ionised. When the voltage pulse is removed the spin echo signal starts to reappear with a delay of 5 μs (2τ) because the echo can be measured only if both microwave pulses are applied after the voltage is removed. The resulting neutralisation time have been measured to be limited by the RC constant of the device to be about 1.6 μs.

Even though the geometry of the device is limiting the dynamics of the process, this result suggests that the neutralisation time is shorter than $\sim 1\mu s$ and it demonstrates the feasibility of charge state control via electric field.

A further study to take advantage of the electric field induced ionisation and neutralisation may include measuring the nuclear spin T_2 of ionised arsenic donors, As^+. However, the main difficulty of this experiment is the low electron spin resonance signal intensity, due to the low total number of spins in the sample. Given the concentration of arsenic donors used here ($4 - 5 \times 10^{16}$ cm^3) and considering that the implantation layer is only 100 nm thick, a total number of donors in the sample is about $\sim 10^{10}$. Unfortunately the time necessary to measure nuclear T_2 of this low number of spins with our experimental sensitivity is currently *too long*.

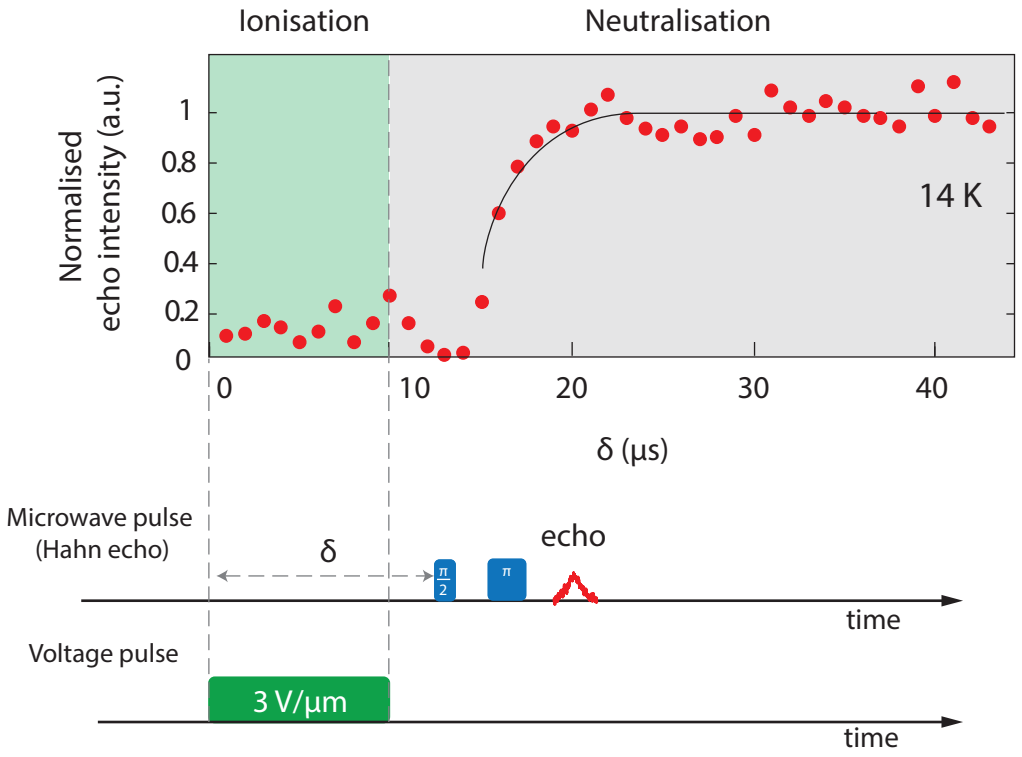


Figure 5.10.: **Ionisation/re-neutralisation dynamics of the ^{75}As:** Normalised electron spin echo signal as a function of time δ from the ionisation pulse V, measured at X-band ($B \sim 0.3$ mT) and at 14 K with $\tau = 2.5$ μs. During a voltage pulse of $\sim$3 V/μm (10 μs), all donors are ionised. When the voltage pulse is removed the spin echo signal starts to reappear with a delay of 5 μs (2τ). The neutralisation time constant of 1.6 μs is limited by the RC constant of the device.

5.4. Conclusions

In conclusion, we have investigated arsenic donor spins under applied electric fields by electron spin resonance.

We measured the Stark shift of the donors by applying electric fields below the ionisation threshold of the dopants, and find a hyperfine Stark shift parameter of $\eta_a = -1.9 \pm 0.7 \times 10^{-3}\ \mu\text{m}^2/\text{V}^2$. Thanks to this result we are able to estimate the value of the electric field necessary to shift an entire ESR line out of resonance. This value ($\sim$1 V/μm) is within achievable local electric field applicable in the SOI technology suggesting the feasibility of single-spin addressability via electric field control.

We also measured the electric field necessary to induce the ionisation of arsenic donor to be $\sim$2 V/μm. This result has two important implications. (1) It gives an experimental measure of the minimum electric field necessary to induce electron tunnelling within the context of single-electron spin measurement by tunnelling to SET devices [MPZ$^+$10, PTD$^+$12, PTD$^+$13]. (2) It sets a limit on the maximum resonance shift that can be applied to arsenic donors before ionisation, with implications on how quickly electron spins can be manipulated in Kane-like architecture [Kan98].

Finally, we demonstrated electric field dynamical control of the charge state of arsenic donors. Even though the geometry of the sample used here is limiting how fast we can re-neutralised the donors, we have determined that this process is shorter then $\sim \mu s$.

CHAPTER 6

Spin relaxation of selenium donors in silicon

Electron and nuclear spin proprieties of chalcogen impurities in silicon have so far attracted limited experimental attention, even though they have already been suggested as potential candidates for silicon-based qubits [KMD+00].

In this Chapter, we introduce the proprieties of selenium impurities in silicon and we characterise the samples, also used in the Chapter 7 for charge state manipulation. For instance, we present here, what is to our knowledge, the first study of the electron spin relaxation T_1 and decoherence T_2 of Si:Se^+ and their mechanisms. These are essential quantities for the potential application of selenium donor spins in quantum information.

Selected results from this Chapter are published in

[LWS$^+$15] R. Lo Nardo, G. Wolfowicz, S. Simmons, A. M. Tyryshkin, H. Riemann, N. V. Abrosimov, P. Becker, H.-J. Pohl, M. Steger, S. A. Lyon, M. L. W. Thewalt and J. J. L. Morton, *Spin relaxation and donor-acceptor recombination of Se^+ in 28-silicon*, **arXiv:** 1503.05811 (2015).

6.1. Materials characterisation

The selenium doped samples used in this Chapter were prepared by M. Steger at Simon Fraser University and have been previously measured by IR absorption spectroscopy [SYT+09].

The sample preparation was realised with starting *p-doped* 28-silicon with high isotopic purification of 99.991% and a residual concentration of 75 ppm ^{29}Si and 15 ppm ^{30}Si. The presence of acceptors is required to partially compensate the sample forming Se^+ [Lud65] and the B concentration is $\sim 5 \times 10^{13}$ cm^{-3}. The value of acceptor concentration was confirmed by the results of the Se^+ spin relaxation T_2, as described in Section 6.3. This is because the concentration of Se^+ at low temperature depends on the concentration of acceptors and can be measured by suppressing the effect of instantaneous diffusion on the electron T_2 (see Section 3.5).

The selenium impurities were thermally diffused in the sample as explained in literature [JSGG84]. Each sample was sealed in an ampoule together with the dopant and was kept at constant diffusion temperature of about ∼1000 K. The samples' resistivity was measured to be about 4 Ω cm, which corresponds to a donor concentration of $\sim 5 \times 10^{15}$ cm^{-3} making the samples *n-doped*. In order to confirm the value for the impurity concentration, we measured the Hall coefficient of the samples, as described below.

The ESR measurements reported in the following Sections were performed using three samples described in Table 6.1. Samples (B) and (C) were diffused with isotopically enriched ^{77}Se at 97.1 % and sample (A) was diffused with selenium at natural isotopic concentration (^{74}Se:0.9%, ^{76}Se:9.4%, ^{77}Se:7.5%, ^{78}Se:23.8%, ^{80}Se:49.6%, ^{82}Se:8.7%).

Sample	Host material	Acceptor	Dopant	Dimensions (mm)
A	^{28}Si	B	^{nat}Se	3×4×1
B	^{28}Si	B	^{77}Se	3×4×1
C	^{28}Si	B	^{77}Se	2×2×8

Table 6.1.: **Si:Se samples measured in this Chapter.** Each sample was prepared by doping an initial *p-doped* 28-silicon substrate with selenium at a concentration larger than that of acceptor making the sample *n-doped* as described in the text.

At thermal equilibrium and given the donor and acceptor concentrations, the population of the electronic levels in the samples can be determined by solving Equation 3.5, as explained in Section 3.2. This solution is determined by calculating the value of chemical potential (μ) for each temperature (T). The temperature dependence of μ and the relative population of the electronic levels, obtained with the impurity concentration for our samples, are given in Figure 6.1.

At low temperature, as many electrons as the number of acceptors [A] move from the donors to fill all the acceptor levels and the number of selenium donors in the Se^+ state is equal to the concentration of acceptors ($\langle Se^+ \rangle \approx [A]$). All the remaining selenium impurities are in the neutral state ($\langle Se^0 \rangle \approx [Se] - [A]$). Increasing the temperature above 150 K, the number of $\langle Se^+ \rangle$ grows rapidly because some of the electrons get a thermal energy sufficient to move into the conduction band. Therefore, the number of $\langle Se^0 \rangle$ decreases and the number of electrons in the conduction band increases.

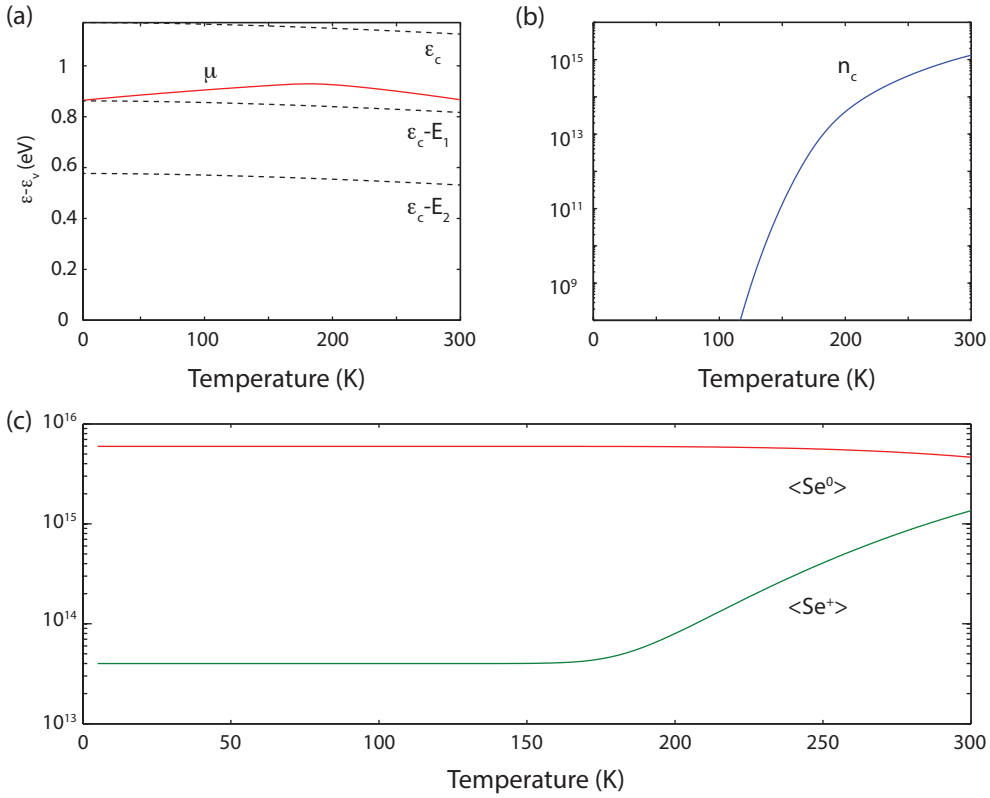


Figure 6.1.: **Population of selenium electronic levels in thermal equilibrium:** (a) Value of the chemical potential, μ, obtained by solving the balance equation using Fermi-Dirac statistics with $[\mathrm{B}] = 5 \times 10^{13}$ cm^{-3} and $[\mathrm{Se}] = 5 \times 10^{15}$ cm^{-3}. (b) Concentration of conduction electrons. (c) Mean number of Se^0 and Se^+ per cm^3.

Hall-effect measurements

Doping levels of the samples were studied by measuring the Hall-effect using the van der Pauw method. The measurement of the Hall-effect in semiconductors enables to determine if the sample is *n-doped* or *p-doped* and the concentration of the majority carriers.

If a constant current I_x is forced to flow across a semiconductor under an external magnetic field B_z, the carriers experience a Lorenz force $F_y = qv_x\ B_z$, where $v_x = I_x/(nqA)$, n is the carrier density, q is the electron charge and A is the area of the sample section perpendicular to I_x. When the steady state is reached, there is no net flow of charge in the y-direction and the potential difference due to the Hall-effect is given by

$$V_y = -\frac{1}{nq}\frac{I_x B_z}{t} \tag{6.1}$$

where t is the thickness of the sample. We therefore define the Hall-coefficient as

$$R_H = \frac{V_y}{I_x} = -\frac{1}{nq}\frac{B_z}{t}. \tag{6.2}$$

The value of R_H is positive if the sample is *n-doped* and it is negative if it is *p-doped*. The value of n can be then calculated from Equation 6.2. If one dimension is much smaller than the others, an accurate measurement of the Hall-coefficient may be obtained by the van der Pauw method. This method requires four Ohmic contact at the four corners of the sample, as shown in Figure 6.2. Under this configuration, the current flows along the edges. If the contacts are numbered from 1 to 4 in a counter-clockwise order we can define

$$\begin{aligned} V_{13} &= -\frac{1}{nq}\frac{I_{24} B_z}{t} \\ V_{24} &= -\frac{1}{nq}\frac{I_{13} B_z}{t} \end{aligned} \tag{6.3}$$

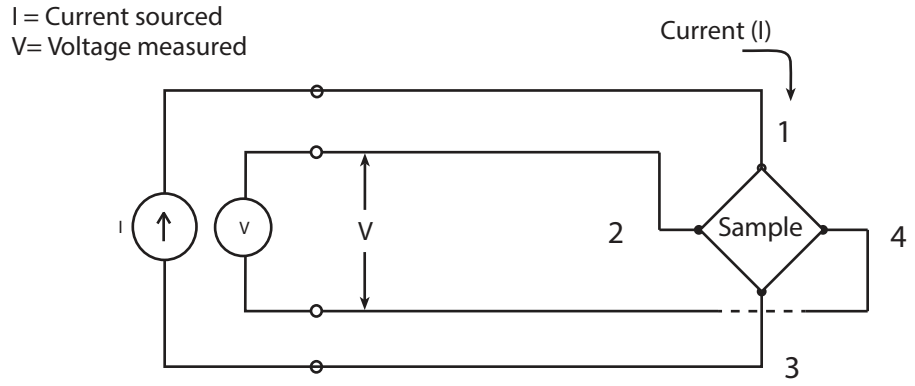


Figure 6.2.: **Schematics of the Hall-effect measurements set-up:** The sample is connected using the van der Pauw method where each of four contact connects one of the corners. The measurement are done under constant current and the Hall voltage is measured by using a Keithley Model 2400 Series SourceMeter controlled by a computer via GPIB connection.

where I_{24} and I_{13} are the current flowing from contact 2 to 4 and from 1 to 3 respectively and we have that $R_H = (V_{13} + V_{24})/(I_{24} + I_{13})$.

The measurements were done under a magnetic field $B = 1\,\mathrm{T} = 10^{-4}\,\mathrm{Wb} \cdot \mathrm{cm}^{-2}$ and a constant current of $I_x = 100\,\mathrm{mA}$ set by a current source, while the voltage measurement used a Keithley Model 2400 Series SourceMeter controlled by a computer via GPIB connection, as described in Figure 6.2.

Given the thickness of the sample $t = 0.115\,\mathrm{cm}$, the measured value of the Hall-coefficient is $R_H = 4.8\,\Omega$, which confirmed that the majority carries in the sample are electron with a concentration of $n_c = 1.1 \times 10^{15}\,\mathrm{cm}^{-3}$. By solving Equation 3.5 for $T \sim 300\,\mathrm{K}$ and given the electron concentration measured, the obtained concentration of selenium impurities in the sample is [Se]$\sim 5 \times 10^{15}\,\mathrm{cm}^{-3}$.

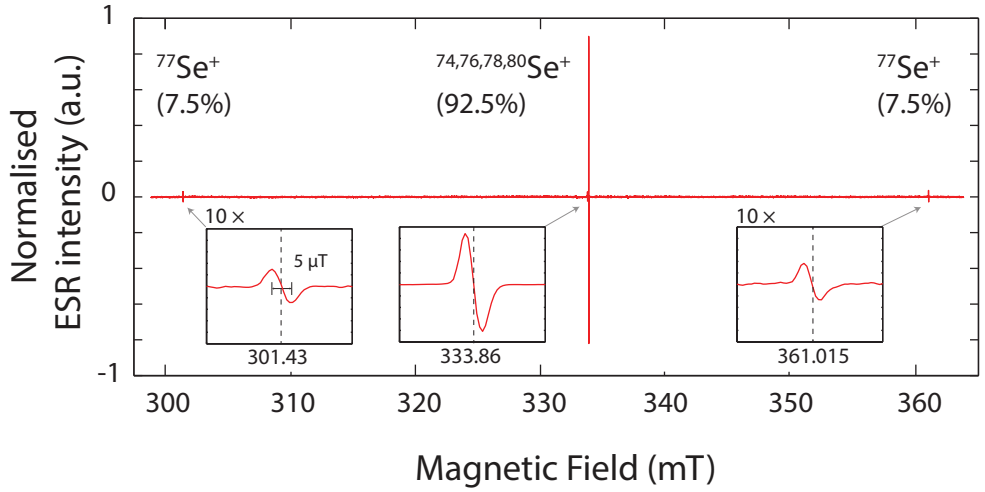


Figure 6.3.: **cw-ESR spectra of sample (A) ^{28}Si:^{nat}Se^{+} at X-band:** The central line corresponds to the Se spin transition of the isotopes with zero nuclear spin ^{X}Se^{+} (X=74, 76, 78, 80). The doublet arises from the ^{77}Se isotope with nuclear spin $I = 1/2$. Measurement at 23 K.

cw-ESR and ENDOR characterisation of Si:Se^+

The samples were first characterised by continuous wave ESR measurements with a Bruker Elexsys spectrometer at X-band (9.7 GHz) and at a magnetic field of ∼0.34 T. Typical cw-ESR spectra measured at 23 K are shown in Figure 6.3 for ^{nat}Se (sample-A) and in Figure 6.4 for ^{77}Se (sample-B).

The peaks in the Figures correspond to the ESR-allowed transitions ($\Delta m_e = \pm 1$, $\Delta m_I = 0$), obtained from Equation 3.29, with g-factor and hyperfine interaction in agreement with the previously reported values [JSGG84]. Due to the isotopic purification of the silicon material, the linewidth ($< 5\ \mu$T) is greatly reduced with respect to previous reported spectra [GJE$^+$81].

In the cw-ESR spectrum of sample (A) in Figure 6.3, the central line corresponds to the spin transition of the isotopes with zero nuclear spin ^{X}Se$^+$ (X=74, 76, 78, 80) and the doublet arises from the ^{77}Se isotope with nuclear spin $I = 1/2$.

The relative intensity of the lines reflects the natural isotope distribution. For sample (B) in Figure 6.4, the central line at $g = 2.0057$ is largely suppressed, due to the isotopic enrichment of the selenium impurities (97.1 %). The remaining features in Figure 6.4 have been characterised by angular dependent cw-ESR and ENDOR and confirmed to be due to ^{77}SeH pairs, previously measured in natural Si and referred as Si-NL60 [HAGD00].

In the insert of Figure 6.4, we plot the spectra of the ^{77}SeH for two particular orientations of the magnetic field along the [100] and the [011] directions of the silicon crystal. When the magnetic field is oriented in the [100] direction, the four possible orientations of the SeH pairs are equivalent and only four lines are measured (linewidth is $< 20\ \mu$T) - each line corresponding to a combination of the ^{77}Se and ^{1}H

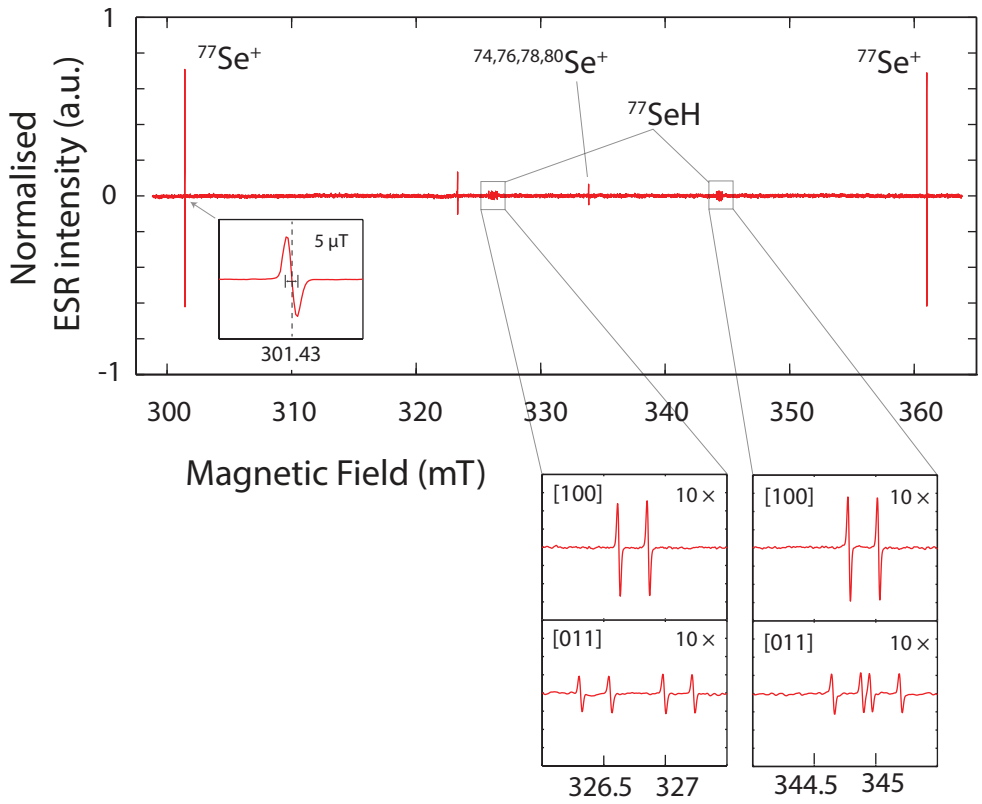


Figure 6.4.: **cw-ESR spectra of sample (B) ^{28}Si:^{77}Se^{+} at X-band:** The doublet arises from the ^{77}Se isotope with nuclear spin $I = 1/2$. The central line at $g = 2.0057$ is largely suppressed by isotopic enrichment of selenium and the remaining transitions are due to ^{77}SeH pairs. Measurement at 23 K.

nuclear spin projection. The larger spitting between the two doublets is ~ 18.3 mT (related to the ^{77}Se hyperfine coupling) with a smaller splitting of ~ 0.24 mT (related to the ^{1}H hyperfine coupling). Therefore, the presence of the hydrogen in this defect centre reduces the ^{77}Se hyperfine coupling by a factor of $\sim$3 and gives it a slight anisotropy. A detailed study of the ^{77}SeH pairs is given in the next Section.

We also characterise the nuclear spin resonance transitions of selenium by electron nuclear double resonance (ENDOR) techniques. These transitions, named f_{24} and f_{31}, are shown in Figure 3.9 and correspond to $\Delta m_I = \pm 1$, $\Delta m_e = 0$. In order to measure the nuclear spin resonance, we use the Davies pulse-ENDOR technique.

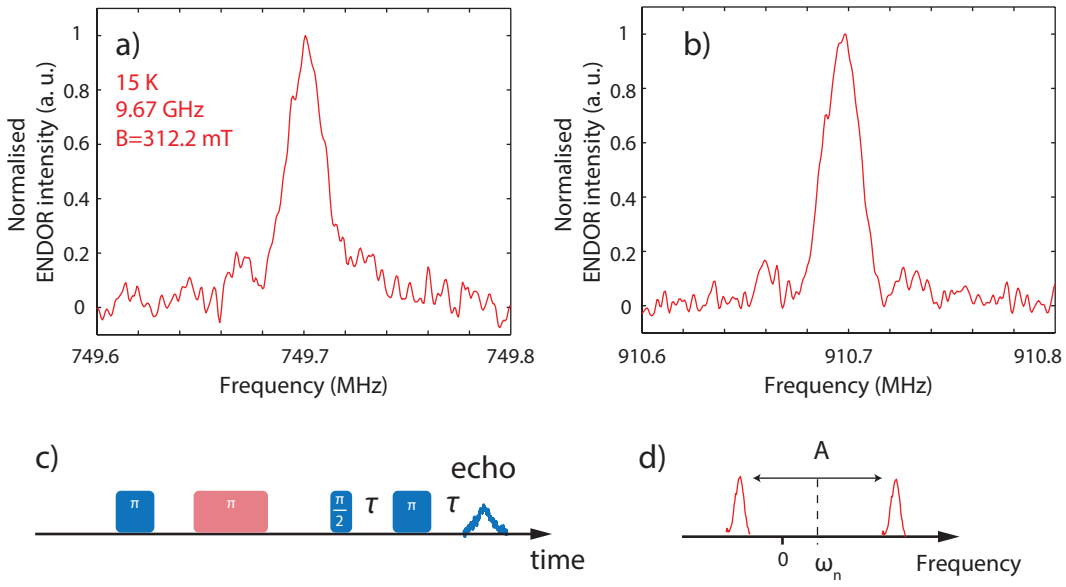


Figure 6.5.: **ENDOR spectra of ^{28}Si:^{77}Se^{+} at X-band: ENDOR transitions f_{31} (a) and f_{24} (b) measured via the ESR transition $m_I = +1/2$. (c) Davies-ENDOR pulse sequence. d) Schematic representation of the central frequency (ω_n) and the separation (A) of the ENDOR peaks.**

This method, based on the combined effect of microwaves (mw) and radio frequency (RF) pulses, allows one to measure nuclear spin resonance by electron spin echo detection. The Davies ENDOR pulse sequence is shown in Figure 6.5 (c). A first mw π-pulse inverts the electron spin polarisation of a particular ESR transition. After this first mw-pulse, a selective RF π-pulse is applied. If the RF π-pulse is resonant with one of the nuclear transitions, the electron spin polarisation is transferred. This change in polarisation is finally detected by the electron spin echo.

Therefore we measure the electron spin echo as a function of the RF pulse frequency in the sequence ($\pi_{\mathrm{mw}} - \pi_{\mathrm{RF}} - \pi/2_{\mathrm{mw}} - \tau - \pi_{\mathrm{mw}} - \tau -$ echo). Typical ENDOR spectra of the nuclear spin transitions of selenium are shown in Figure 6.5. The two ENDOR peaks in Figure 6.5 are centred at a frequency of 80.5 MHz. The separation of the peaks, 1660.4 MHz, corresponds to ^{77}Se hyperfine splitting.

cw-ESR and ENDOR characterisation of ^{77}SeH pairs in ^{28}Si

In this Section, we study the origin of the angular-dependent transitions observed in Figure 6.4 and we demonstrate that they arise from ^{77}SeH pairs.

We first measure the cw-ESR angular dependence of these transitions. Their central field of each resonance is given in Figure 6.6 as function of the rotation angle θ between the magnetic field and the [100] direction of the silicon crystal, when the sample is rotated along [011]. In this notation, the two spectra given in Figure 6.4 correspond to $\theta = 0°$ for [100] and $\theta = 90°$ for [011].

From the angular dependence given in Figure 6.6, three quartets of resonances can be identified (red, blue and green dots). Each quartet corresponds to a spin system oriented along a particular direction of the crystal with one electron spin interacting with two nuclear spins. Although there are four possible orientations of this system, at least two of them are always equivalent by symmetry, leaving three sets of lines in general.

The angular dependence of the resonances of each quartet is well fit by the Hamiltonian (solid lines in Figure)

$$\begin{aligned}\mathcal{H} =& \frac{\beta}{\hbar}\, \boldsymbol{g}_e \cdot \boldsymbol{S} \cdot \boldsymbol{B} - \frac{g_{n1}\beta_{n1}}{\hbar}\, \boldsymbol{I_1} \cdot \boldsymbol{B} - \frac{g_{n2}\beta_{n2}}{\hbar}\, \boldsymbol{I_2} \cdot \boldsymbol{B} \\ &+ \boldsymbol{S} \cdot \boldsymbol{A_1} \cdot \boldsymbol{I_1} + \boldsymbol{S} \cdot \boldsymbol{A_2} \cdot \boldsymbol{I_2}\end{aligned} \tag{6.4}$$

where the first three terms are the electron and nuclei Zeeman energies and the last two terms are the hyperfine interaction of the electron with the two nuclei (^{77}Se and ^{1}H).

The fit in Figure 6.6 (solid lines) was obtained by using the MATLAB toolbox *EasySpin* 4.5.5. The results of the fitting confirm that the three set of four transitions

arise from a complex of one electron spin interacting with two nuclear spins oriented along the four equivalent <111> directions of the silicon crystal. The schematic Figure 6.7 (c) represents one of the four possible orientation of this complex.

The g-tensor and the two hyperfine tensors obtained from the fit (in the pair coordinates) are

$$\boldsymbol{g}_e = \begin{pmatrix} 1.996 & 0 & 0 \\ 0 & 1.995 & 0 \\ 0 & 0 & 1.995 \end{pmatrix} \tag{6.5}$$

$$\boldsymbol{A}_1 = \begin{pmatrix} 6.78 & 0 & 0 \\ 0 & 6.60 & 0 \\ 0 & 0 & 6.60 \end{pmatrix} \text{ MHz} \tag{6.6}$$

$$\boldsymbol{A}_2 = \begin{pmatrix} 535.6 & 0 & 0 \\ 0 & 495.3 & 0 \\ 0 & 0 & 495.3 \end{pmatrix} \text{ MHz.} \tag{6.7}$$

The solution of the Hamiltonian in Equation 6.4 gives eight energy levels which are represented in the schematic (a) in Figure 6.7. When the field is oriented along [100], the four orientations of the pairs are equivalent and therefore only four resonances are measured, as shown in Figure 6.4 and 6.6. Along this particular orientation, the hyperfine constants obtained from the fitting relate to the observed splitting and we are $A_2 \sim 510MHz$ ($\sim$ 18.3 mT) and $A_1 \sim 6.73$ MHz ($\sim$ 0.24 mT).

The large difference in the intensity of the two hyperfine constants suggests that the electron is spatially closer to the one of the two nuclear spins. In order to confirm the element species involved in the pairs, we measured nuclear spin resonant transitions by Davies-ENDOR technique, at each of the four ESR lines, when the field is applied

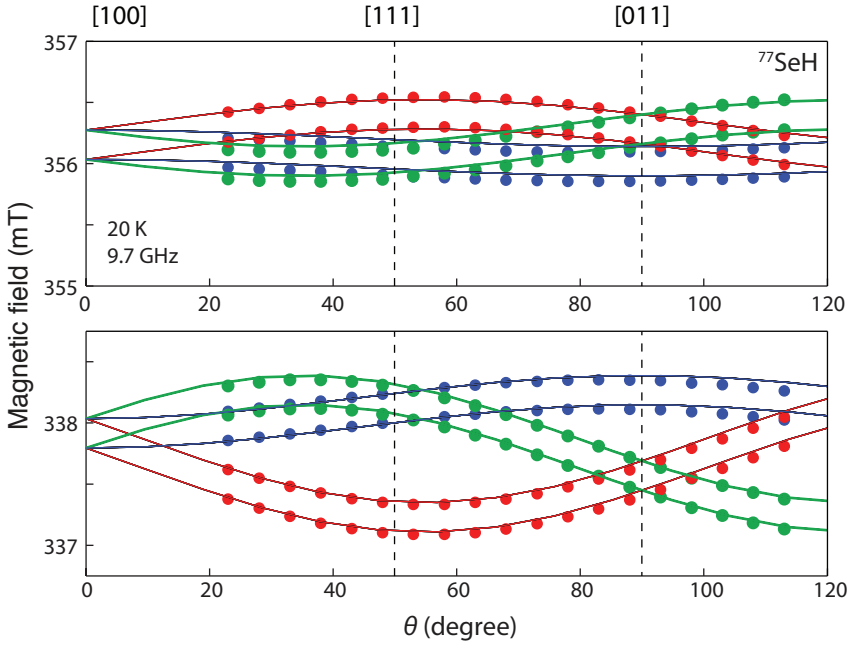


Figure 6.6.: **Angular dependence of the cw-ESR of the SeH pairs:** central field of the cw-ESR resonance as a function of the rotation angle θ between the magnetic field and the [100] direction of the silicon crystal, when the sample is rotated along [011]. Measurements at X-band (9.7 GHz).

along the [100] direction.

For the two central ESR transitions (f_{34} and f_{56} as named in the schematic in Figure 6.7 (a)) there are four observable ENDOR resonances that correspond to the two nuclear spin transitions (i.e. $\Delta m_{I_1} = \pm 1$ and $\Delta m_{I_2} = \pm 1$ with $\Delta m_e = 0$). For the two external ESR transitions only two ENDOR transition are observable. In Figure 6.7 (b), we plot the ENDOR transitions named f_{24} and f_{13}, both relative to the ESR transition f_{34}.

The two ENDOR peaks, in Figure 6.7 (b), are separated by 6.73 MHz (which corresponds to the hyperfine splitting A_1) and they are centred at 14.4 MHz which is the Zeeman energy of the hydrogen nuclear spin at $B = 337.2$ mT, confirming that the second nuclear spin involved in the pair is hydrogen.

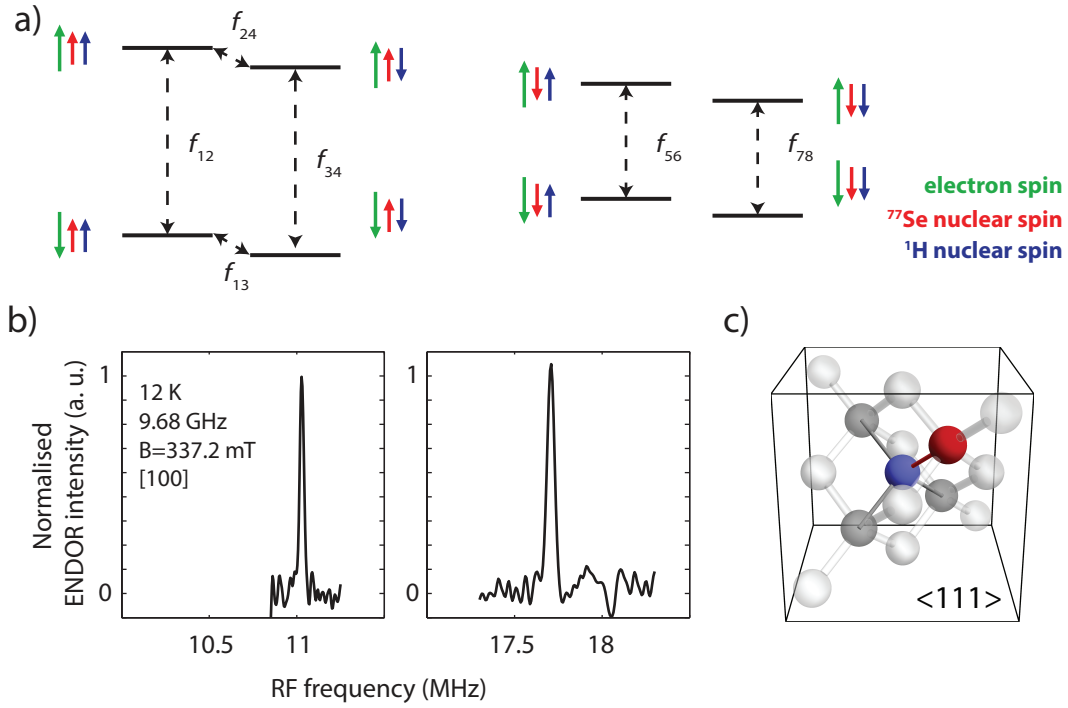


Figure 6.7.: **cw-ESR characterisation of the SeH pairs:** (a) Schematic representation of the energy levels of one SeH pair. (b) ENDOR spectra relative to the ESR transition f_{34} when the magnetic field is applied along the [100] direction. The two peaks arise from the transitions f_{24} and f_{13}. (c) Schematic representation of the Se and H atoms within the silicon crystal structure orientated along one of the equivalent <111> directions.

The values of the g-tensor and the hyperfine tensors obtained from the fit agree (within the experimental error) with the result previously attributed to ^{77}SeH pairs in natural silicon [HAGD00]. In the work of the last reference, the fit of the A and g-tensor were obtained by angular dependent ENDOR measurement because the linewidth of the ESR resonance was larger than hyperfine splitting (0.24 mT). The linewidth of the resonances measured here is much smaller, (<20 μT) due to isotopic purification of 28-silicon, and allows us to obtain the tensors only by cw-ESR.

6.2. Electron spin relaxation

In this Section we study electron spin relaxation of selenium impurities in 28-silicon. Electron spin relaxation times T_1 were measured by pulsed ESR using the inversion-recovery technique, where the electron Hahn echo is detected at different times (T) after an inversion pulse (π) in the sequence ($\pi - T - \pi/2 - \tau - \pi - \tau - \text{echo}$).

The results of the spin relaxation of $^{77}Se^{+}$, measured for sample (B), are shown in Figure 6.8 (blue dots). We find that $(1/T_1)$ is well fitted by $1/T_1 = CT^9$ with $C = 1.2 \times 10^{-8}$ s^{-1}K^9, in the temperature range of $5 - 35$ K, (blue solid line). The T_1 measurements, on all the samples and for both the ^{77}Se isotope (with $I = 1/2$) and on the Se isotopes with $I = 0$, show the same results within experimental error, implying that the electron spin relaxation time is independent of the projection of selenium nuclear spin ($m_I = 0, \pm 1/2$).

A comparison with P donors in silicon shows that T_1 is between one and two order of magnitude longer for Se^{+} in this temperature range. Figure 6.8 also shows the temperature dependence of the electron spin T_1 for P (red dots) and the relative contributions of the different relaxation mechanisms (red dashed lines), as discussed in Chapter 3. Si:P data are from reference [Cas63]. The red solid line in Figure 6.8 is the experimental fit given by equation

$$\frac{1}{T_1} = CT^9 + D \exp\left(\frac{\Delta}{k_B T}\right) \tag{6.8}$$

where $C = 10^{-7}$ s^{-1}K^{-9} and $D = 2 \times 10^8$ s^{-1} [YH68]. The two terms on the right side of Equation 6.8 refer to the Raman and the Orbach processes respectively.

The Orbach two-phonon relaxation process [Orb61, Cas67] depends exponentially on the energy gap, $\Delta = 1s(T_2) - 1s(A_1)$, between the ground state and first excited

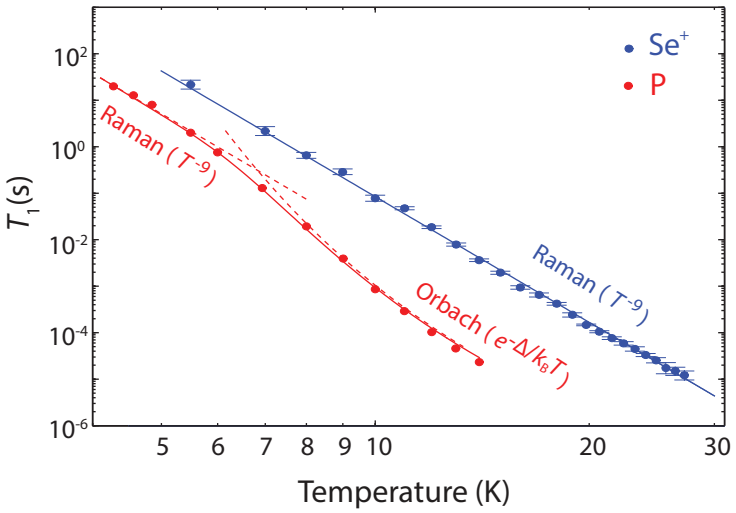


Figure 6.8.: **Temperature dependence of electron spin relaxation time T_1 in ^{28}Si:^{77}Se$^+$ and Si:P at** $B \sim 0.34$ T: Blue dots (Se) and red dots (P). Solid lines are fits to the experimental data, made up of contributions (dashed lines) from different relaxation mechanisms. For selenium the temperature dependence of T_1 is well fit with T^{-9} Raman process. For phosphorous both Raman and Orbach processes are considered in this temperature range. Data for Si:P is from Ref [Cas63].

state of the donor: $T_1 \propto \exp(\Delta/k_BT)$. Therefore, though the Orbach process is the dominant T_1 mechanism for phosphorus donors at X-band and at temperatures above ∼8 K, the large value of $\Delta = 429$ meV for Se$^+$ makes the Orbach process irrelevant here.

The T^9 Raman process dominates the phosphorus donor electron spin relaxation in the range $2-6$ K at X-band [Cas67], arising from two-phonon scattering via a continuum of excited states. Table 6.2 reviews the experimental values of the coefficients C together with the energy separation with the first excited state (Δ) for donors in silicon. It has been observed in the shallow donors that this process has only a weak dependence on Δ, which dictates the spin mixing through a spin-orbit coupling [Cas67]. Our results on Se$^+$ are consistent with this observation – despite the much larger value of Δ, the strength of the T^9 Raman process is only marginally weaker than for the shallow donors. Nevertheless, the electron spin T_1

Donor	Tem. Raman range (K)	C ($s^{-1}K^9$) CT^9	Δ (meV)	Reference
P	2.6 - 6	10×10^{-8}	10.5	[Cas63]
As	5 - 11	2×10^{-8}	19.7	[Cas63]
Bi	5 - 26	6.6×10^{-8}	33.8	[WST+12b]
Se^+	5 - 35	1.2×10^{-8}	429	this work

Table 6.2.: Experimental value of the temperature dependence of the electron spin relaxation (T_1) in the Raman regime and energy separation (Δ) to the first excited state ($1s(T_2)$) for donor in silicon.

for Se^+ in silicon remains longer than any of the shallow donors across the full temperature range studied here, suggesting that it may also offer the longest spin coherence times.

It is worth briefly considering an alternative electron spin relaxation mechanism based on the interaction with the acceptors. In our samples, for every selenium impurity in the Se^+ state there is one acceptor in a charged state due to compensation [Lud65]. Under these conditions the charges localised on the isolated impurities are known to originate a Coulomb interaction between them. This interaction may be responsible for the formation of bound states known as donor-acceptor (DA) pairs [Wil68]. Therefore the presence of acceptors could in principal limit the electron spin relaxation by an electron-exchange interaction with the Se^+.

The mechanism of relaxation due to $S = 0$ pairs has been suggested in literature in order to explain concentration-depend relaxation for shallow donors with concentrations above 10^{16} cm^{-3}. In this mechanism, the relaxation is dominated by nearby fast-relaxing centres [YH68]. Under these conditions, the relaxation process is given by the modulation of the exchange interaction with donor spin pairs in a $S = 0$ spin state [Sug63]. This mechanism involves a phonon transition to the triplet state of the pair, inducing a spin-flip of the donor by relaxing back to the sin-

gle state [HS60]. The resulting effect on the spin relaxation would be concentration dependent. Here, we exclude that this mechanism is having an effect on the spin relaxation because no difference is observed among different samples and different isotopes of selenium. However, in order to conclusively exclude the effect of $S = 0$ pairs on spin relaxation, further measurement may be done without acceptors. The ionisation of the selenium impurities could be in principle achieved also by electric field ionisation [KMD$^+$00]. The required electric field for selenium ionisation has been theoretically calculated to be of the order of 10^8 Vm^{-1}, following the approach described by Pica *et al.* [PWU$^+$14].

6.3. Electron spin coherence

The electron spin coherence time (T_2) of $^{77}Se^+$ was measured by varying τ in the Hahn echo sequence ($\pi/2 - \tau - \pi - \tau -$ echo) and the results (red dots) are shown in Figure 6.9 (b). We find that T_2 is limited by spin relaxation (T_1) down to about 15 K. Below this temperature, T_2 in these samples is limited by dipole coupling between Se^+ electron spins which are not refocussed by the Hahn echo sequence, a mechanism called instantaneous diffusion (ID) [TTM$^+$12, WST$^+$12b]. This effect can be mitigated by reducing the angle of the θ_2 pulse in the Hahn sequence ($\pi/2 - \tau - \theta_2 - \tau -$ echo), as explained in Section 3.5 [SJ01, TTM$^+$12].

Figure 6.9 (a) shows the measured $1/T_2$ as a function of $\sin^2(\theta_2/2)$ for two different temperatures. The value of T_2 in absence of ID (red stars in Figure 6.9 (b)), and the measure of the concentration of Se^+electron spins are calculated by extrapolating the intercept at $\theta_2 = 0$ form as described form equation

$$\frac{1}{T_2} = \frac{5}{2}\frac{\mu_0}{4\pi}\frac{(g\beta_0)^2}{\hbar}\frac{\langle Se^+\rangle}{2}\sin^2\left(\frac{\theta_2}{2}\right) + \frac{1}{T_{2,\mathrm{ext}}}. \tag{6.9}$$

The concentration of Se^+ we obtain is 4×10^{13} cm^{-3}, confirming the level of boron in this sample. The extrapolated value of T_2 in the absence of ID, can be well described by a combination of spectral diffusion arising from T_1-induced spin flips of neighbouring Se^+ spins, combined with a temperature-independent mechanism that limits T_2 to about 80 ms.

The red solid line in Figure 6.9 (b) gives the temperature dependence of the extapolated value of T_2 (in the absence of ID). The model is obtained by taking into account the combined effects of the three mechanisms described above: i) spin relaxation of the central spin, yielding an echo decay of the form $\exp[-(2\tau/T_1)]$; ii) a temper-

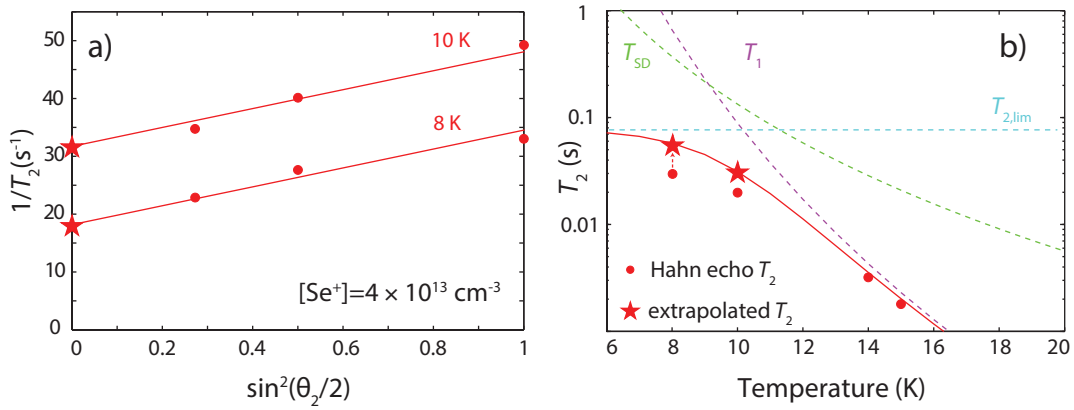


Figure 6.9.: **Extrapolated T_2 in ^{28}Si:^{77}Se$^+$ at** $B \sim 0.34$ T: a) $1/T_2$ as function of rotation angle θ_2. The intercept of the linear fit gives the extrapolated T_2 corresponding to the suppression of the instantaneous diffusion (see main text). The slope of the fit correlates to the concentration of Se^+ (4×10^{13} cm^{-3}). b) Temperature dependence of extrapolated T_2. The value of T_2 is limited by T_1 above ~12 K. Below this temperature, the extrapolated value of T_2 (in the absence of ID) can be well described by a combination of spectral diffusion arising from T_1-induced spin flips of neighbouring Se^+ spins, combined with a temperature-independent mechanism that limits T_2 to about 80 ms.

ature independent process of the form $\exp[-(2\tau/T_{2,\mathrm{lim}})]$ with $T_{2,\mathrm{lim}} = 80$ ms; and iii) a spectral diffusion process caused by spin relaxation of nearest neighbours, of the form $\exp[-(2\tau/T_{SD})^2]$ with $T_{SD}^2 = K\,T_1/[\mathrm{Se}^+]$ and $K = 7.6 \times 10^{12}$ s/cm^3 [SJ01, TTM$^+$12].

At the spin concentration used here, indirect flip-flop of neighbour electron spins is expected to limit T_2 to about ~1 s [TTM$^+$12]. We then postulate the temperature independent-mechanism observed arises from charge tunnelling in the sample, due to the high impurity concentration and compensation in the material. Therefore, for lower donor concentrations and using alternative means of ionising the Se, we anticipate the coherence times will be at least as long as those obtained for P (and indeed, longer, for the same temperature).

6.4. Nuclear spin coherence

The coherence time of ^{77}Se nuclear spin (T_{2n}) is studied in this Section, in the case the donor is in the Se^+ state. The method used here to measure T_{2n}, has already been used to demonstrate that a coherent electron spin state can be transferred to a nuclear spin in Si:P [MTB$^+$08]. This method is based on an ENDOR pulse sequence used to excite both the electron and the nuclear spins and to measure the nuclear spin state via the electron spin. As shown in Ref. [MTB$^+$08], the nuclear spin coherence time can be considerably longer than the one of the electron spin. In particular, T_{2n} of phosphorous in silicon has been shown to be limited by $2T_{1e}$ above about 9 K. Below this temperature, a temperature independent mechanism due to the dipole-dipole interaction between the spins limits T_{2n}.

The schematic in Figure 6.10 illustrates the pulse sequence used for the coherent-state transfer and to measure T_{2n}. The electron spin coherence is first generated by an initial mw $\pi/2$ pulse. We then apply a second mw π-pulse to refocus the electron spins. When the electron spins are refocused, we apply a sequence of on-resonance RF π and mw π-pulses to transfer the coherent state from an electron spin degree of freedom to the nuclear spin. The process of coherent state transfer, obtained by those two pulses, is described in the insert in Figure 6.10. After the application of an RF π-pulse to refocus the nuclear spins, the sequence is reversed to transfer back the coherent state to the electron spins, in order to allow the state read-out.

The nuclear spin coherence time T_{2n} is then measured by detecting the electron spin echo obtained at the end of the sequence, varying the time τ_n (shown in Figure 6.10). A typical decay obtained to measure T_{2n} at 12 K is shown in Figure 6.11 (b). In those measurements, we chose the ESR transition f_{mw} and the nuclear spin transition f_{RF}, as shown in Figure 6.10. At this temperature we find that $T_{2n} = 10$ ms

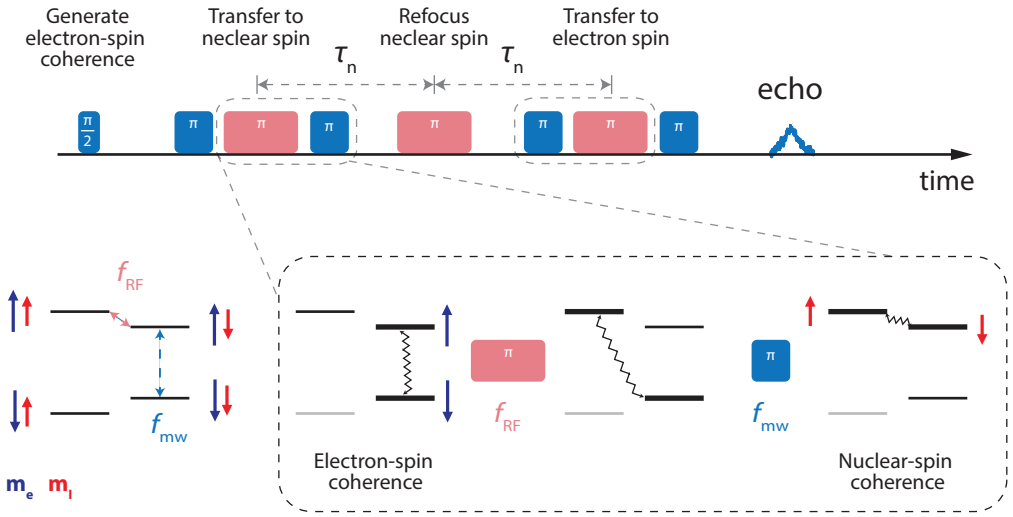


Figure 6.10.: **Schematic of pulse sequence used to measure nuclear spin coherence time T_{2n}:** A coherent superposition of the electron spin is created and transferred to the nuclear spin. After a time $2\tau_n$, the coherence is transferred back to the electron spin and measured by the spin echo sequence.

and $T_{1e} = 18$ ms (shown in Figure 6.11 (a)). The temperature dependence of the measured T_{2n} is shown in Figure 6.12 for selenium (a) - data for phosphorous (b) ([P]=3×10^{15} cm^{-3}) is shown for comparison.

For phosphorous, the temperature dependence of T_{2n} follows $2T_{1e}$ above about 8 K. Below this temperature a temperature independent mechanism limits T_{2n} to about 110 ms. We therefore fit the temperature dependence of phosphorus nuclear spin coherence time T_{2n} with the equation

$$\frac{1}{T_{2n}} = \frac{1}{2T_{1e}} + \frac{1}{T_{2n,\mathrm{lim}}}, \tag{6.10}$$

as shown in Figure 6.12 (b) - (red solid lines). The temperature independent mechanism, observed here for Si:P, is known to arise from dipole-dipole nuclear spins interaction, which depends on the impurities concentration.

For selenium, the temperature dependence of the nuclear spin coherence time (T_{2n})

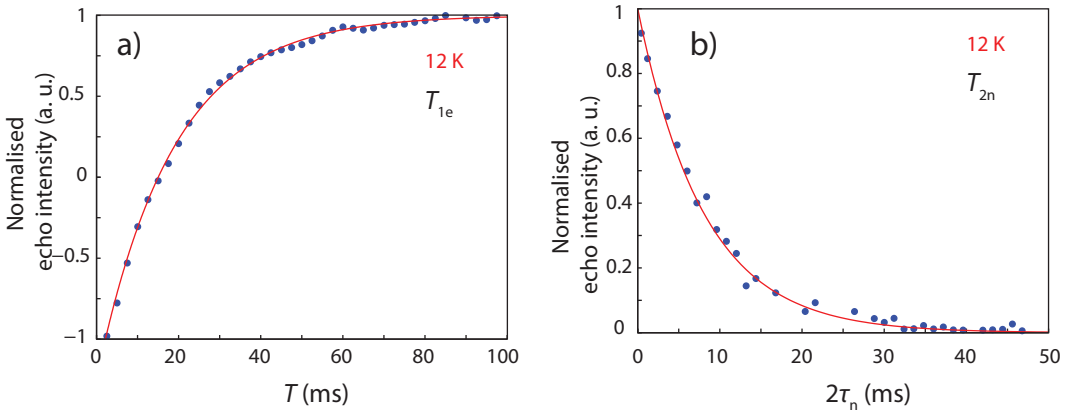


Figure 6.11.: **Electron spin T_1 and nuclear spin T_2 of $^{77}Se^+$ at 12 K:** Electron T_{1e} is measured by varying T in the inversion recovery sequence. Nuclear T_{2n} is measured by varying τ_n in the sequence in Figure 6.10.

does not seems to be limited by the same mechanisms as for phosphorous (see Figure 6.12 (a)) and T_{2n} seems to be closer to the electron spin coherence time T_{2e} (green dashed line).

We therefore postulate that a different mechanism is responsible here for the decoherence of ^{77}Se nuclear spins. It is worth noticing that because T_{2n} and T_{2e} are limited to about the same values, a similar mechanism may be responsible for both the electron and nuclear spin decoherence. In this case, because the electron and the nuclear spins have different gyromagnetic ratios, this common mechanism is unlikely to arise from magnetic dipole-dipole interactions.

An alternative mechanisms may then arise from the electrical noise due to charge tunnelling (caused by the presence of acceptors). For example, electrical noise is known to affect the nuclear spin coherence thought the Stark shift of the nuclear spin resonance [WUT+14], which results in T_{2n} being limited to the same value as the electron spin coherence. Although the Stark shift parameters are not yet known for Se^+, we expect this effect to be weak for selenium due to the large energy gap to the first excited state, and because studies on group-V donors have show Stark

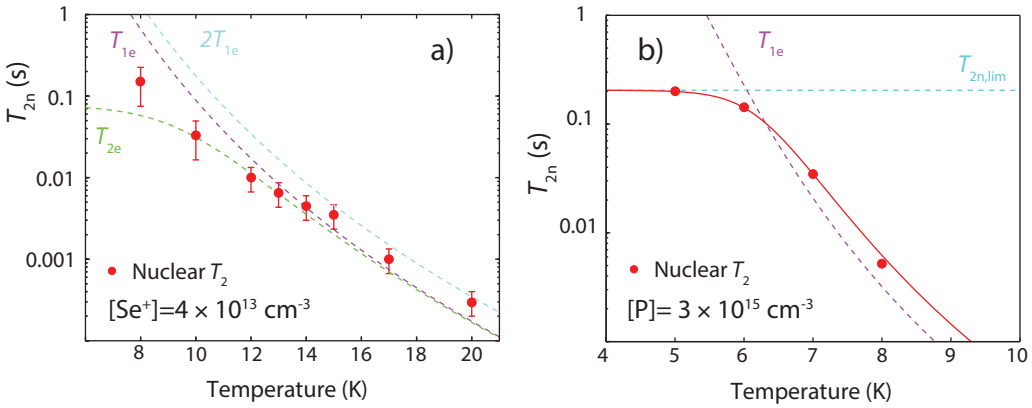


Figure 6.12.: **Temperature dependence of the nuclear spin coherence:** T_{2n} of selenium (a) and phosphorous (b). Red dots experimental data. Red solid line is fit using Eq. 6.10

shift parameters depend on the size of this gap [PWU+14]. On the other hand, if the electron of the donor being measured tunnels away, this process generates both electron and nuclear spin decoherence, independently from the Stark shift and so the charge-tunnelling may nevertheless be responsible for the observed T_{2n} times.

The electron-nuclear spin mixing may also have an effect on the nuclear spin decoherence. Because of the large hyperfine constant of selenium (1.66 GHz), the eigenstates of the electron-nuclear spin Hamiltonian have a non-negligible degree of mixing at X-band, which may also reduce the nuclear spin coherence time. If this were solely responsible for the observed T_{2n}, however, we would expect the T_{2n} times to be longer than T_{2e} by some factor, while the data show that they almost overlap. Further studies at different donor concentration and compensation are needed to pull apart these different mechanisms in more details.

6.5. Conclusions

The electron spin relaxation and decoherence times of selenium measured in this Chapter have confirmed the potential advantage of Si:Se for quantum information applications. In particular, the electron spin relaxation T_1 of selenium is the longest observed for donors in silicon in the temperature range $5 - 35$ K. The larger ionisation energy of selenium with respect to group-V donors reduces the effect of the interaction with phonons, increasing T_1.

As a result of the longer relaxation time, the coherence time T_2 of the Se^+ electron spin is also the longest observed for donors in silicon above 10 K. This trend is likely to extend to lower temperatures for samples with lower Se concentrations than those studied here. The large ionisation energy should also result in a dramatically reduced Stark shift [PWU+14] compared to shallow donors, such that the electron and nuclear spin coherence of Se^+ could be relatively unaffected by charge noise in nano-devices, despite the large value of the hyperfine coupling.

The results reported in this Chapter also motivate further experimental and theoretical investigation on the relaxation and decoherence of selenium impurities in silicon. For instance, a concentration and compensation dependence at low temperature may verify if the trend observed in this work extends to lower temperatures and may conclusively demonstrate the origin of the low temperature decoherence mechanism. A study of the relaxation mechanisms without acceptors may also exclude their potential effect on measurements process studied here. Finally, theoretical work on selenium electron spin may also provide a better qualitative and quantitative understanding on the relaxation and decoherence mechanisms.

CHAPTER 7

Optical charge state manipulation in selenium doped silicon

Optical illumination techniques combined with spin resonance are extensively used to study the proprieties of electron-nuclear spins of donor in silicon. For instance, in ESR studies at low temperature optical illumination is used to generate free carriers to accelerate electron spin relaxation allowing measurement repetition times that are shorter than electron intrinsic relaxation T_1 [TLAR03]. Electrically detected magnetic resonance (EDMR) of spin dependent recombination in silicon also relies on the optical generation of free carriers. Electron spin coherent detection of phosphorous impurities near the surface has been measured electrically using this technique [SBH$^+$06].

The properties of ionised impurities have also been demonstrated by combining

optical pulses with spin resonance. Recent experiments have shown that nuclear spin coherence can be enhanced by removing the hyperfine interaction with the electron spin by placing the donor in a charge state (D^+) [DHSB12].

In this Chapter, we investigate donor-acceptor (DA) recombination in compensated selenium doped silicon, following above band gap illumination, as a strategy for optical charge state manipulation.

Selected results from this Chapter are published in
[LWS$^+$15] R. Lo Nardo, G. Wolfowicz, S. Simmons, A. M. Tyryshkin, H. Riemann, N. V. Abrosimov, P. Becker, H.-J. Pohl, M. Steger, S. A. Lyon, M. L. W. Thewalt and J. J. L. Morton, *Spin relaxation and donor-acceptor recombination of Se^+ in 28-silicon*, **arXiv:** 1503.05811 (2015).

7.1. DA recombination dynamics in compensated selenium doped silicon

Singly-ionised selenium impurities in compensated silicon are present under by thermal equilibrium conditions. The application of pulses of optical illumination at different frequencies may be used to bring them out of this equilibrium state, such as from Se^+ to Se^0 and *vice versa*. However, removing the illumination, the equilibrium conditions will be re-established by subsequent dynamics.

Thermal equilibrium of charges in compensated silicon depends on the value of chemical potential, impurity concentration and temperature. Given donor and acceptor concentrations, the thermal equilibrium condition can be calculated by solving a balance equation, as discussed in Section 3.2. If the concentration of donors is higher than the acceptors (i.e. *n-type* sample) and below a certain temperature, as many electrons as the number of acceptors move from the donors to fill the acceptors level. In compensated selenium doped *n-type* silicon, this condition is reached below about $\sim$150 K because of the value of the ionisation energies.

Given the concentration of selenium [Se] and boron [B] used here ([Se] $\gg$ [B]), the charge state at thermal equilibrium has been discussed in Section 6.1. In particular, Figure 6.1 gives the temperature dependence of the chemical potential and the population of the electronic level of selenium impurities. At low temperature ($T <$ 150 K), the chemical potential is such that the equilibrium state is $\langle Se^+ \rangle_{eq} \approx$ [B] and $\langle B^- \rangle_{eq} \approx$ [B].

If at time t_0 all the impurities in sample are re-neutralised ($\langle Se^+ \rangle(t_0) = 0$ and $\langle B^- \rangle(t_0) = 0$), donor electrons will naturally move back to the acceptors to re-establish thermal equilibrium condition. The dynamics of this recombination process

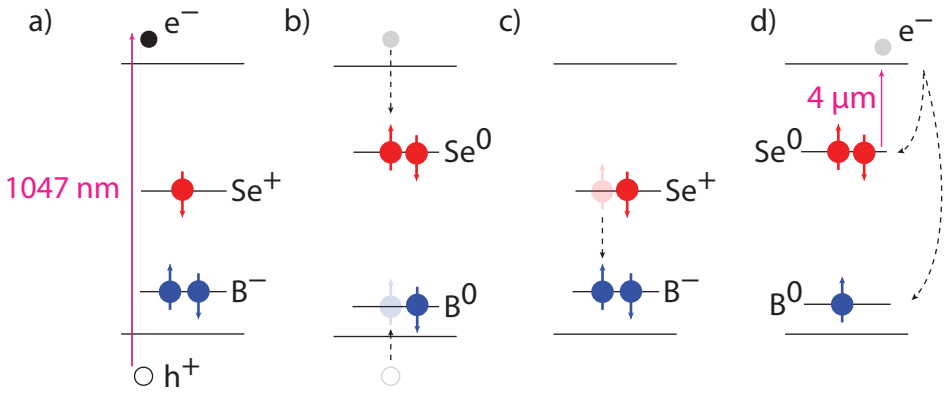


Figure 7.1.: **Schematic representation of the recombination mechanisms in selenium doped silicon after above band gap illumination:** (a) At thermal equilibrium one of the electron from a selenium impurity moves to the acceptor B forming the DA pair (Se^+B^-). Under 1047 nm illumination electron-hole pairs are formed. (b) The excess of conduction carriers recombines through the impurities levels forming a non-equilibrium state. (c) The process of DA recombination re-establishes the thermal equilibrium. (d) Under 4 μm illumination, an electron from Se^0 is continuously pumped into the conduction band enhancing the rate at which the thermal equilibrium is re-established.

has been previously modelled for compensated silicon doped with group-V impurities by Thomas *et al.* [THA65].

In reference [THA65] the dynamics lead to an exponential behaviour which strongly depends on the DA pair distance separation. Appendix B gives a derivation of the dynamics of DA recombination process adapted for group-VI impurities in silicon and based on the approximations used in reference [THA65].

Charge neutralisation in compensated silicon may be experimentally obtained by above band gap illumination. In silicon, optical illumination with photon energy larger than conduction band gap (≈1.1 eV) is known to generate free electron-hole pairs. Those carries usually recombine *faster* (≈ms) than the DA recombination [DHW89], and effectively neutralise all donors and acceptors in the sample. The DA recombination dynamics for compensated phosphorous doped silicon has been measured using this method [DHW89].

Figure 7.1 gives a schematic representation of DA recombination following optical illumination for compensated selenium doped silicon. Se^+ and B^- impurities, which are charged under thermal equilibrium conditions are first neutralised following the creation of free carriers. Due to the fast capture of free carriers into the impurities levels, the neutral condition is established. The following DA recombination dynamics brings the system back to thermal equilibrium.

7.2. Materials and methods

The technique used to study DA recombination, following above band-gap laser illumination, is based on measuring the Se^+ electron spin echo as it recovers back to thermal equilibrium. This method has been previously used to study DA recombination of highly compensated phosphorus-doped silicon [DHW89] showing that the recombination time can be as long as $\sim 10^3$ s.

The sample used in this Chapter, is compensated 77-selenium doped 28-silicon with [Se]=5×10^{15} cm^{-3} and [B]=4×10^{13} cm^{-3} (sample (B) as named in Section 6.1). ESR measurements were carried out with a pulsed Bruker Elexsys spectrometer at X-band (9.7 GHz) and at a magnetic field of $\sim$0.34 T. In order to measure the photoconductivity under illumination, we have connected the sample as shown in Figure 7.3. Under the application of an oscillating voltage 1 mV, the current across the sample is amplified and detected by a lock-in amplifier. The data are finally acquired by a digital oscilloscope.

Optical pulses at various frequencies were synchronised with the ESR detection as shown in Figure 7.3. The above band gap illumination is generated by a solid state laser diode with frequency of 1047 nm and a maximum power of 500 mW.

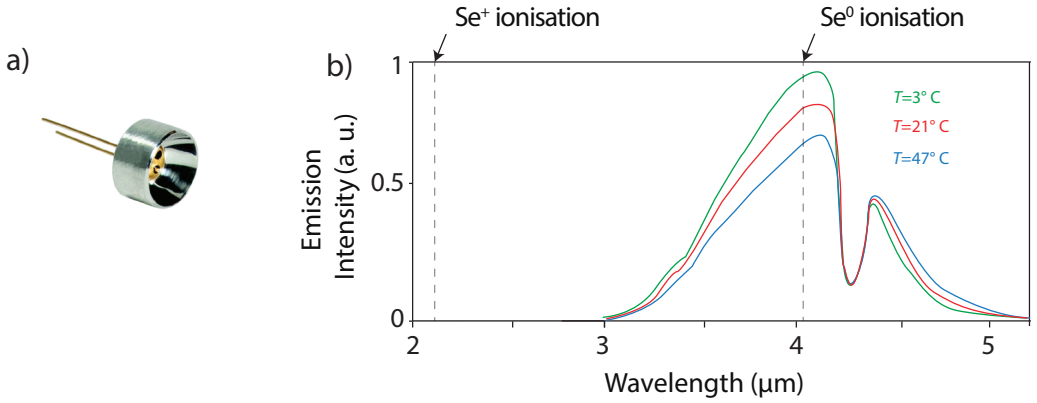


Figure 7.2.: **THORLABS LED4300P** 4 μm **LED:** (a) Image of the LED. (b) Optical spectra at different temperature as indicated in Figure. Data from the LED data sheet. 4.3.

A commercial THORLABS LED4300P 4 μm LED is used for selective ionisation of the selenium donors. The LED, shown in Figure 7.2 (a), is powered with a constant current of 200 mA by an home-made power supply. Typical spectra of the LED at different temperature are shown Figure 7.2 (b). This particular LED has been chosen because its illumination only ionises selenium impurities in the Se^0 state and does not excite those in the Se^+ state (as it can be observed by comparing the spectra in Figure 7.2 with the schematics of the selenium energy levels in Figure 3.3), nor excite free carriers across the band gap.

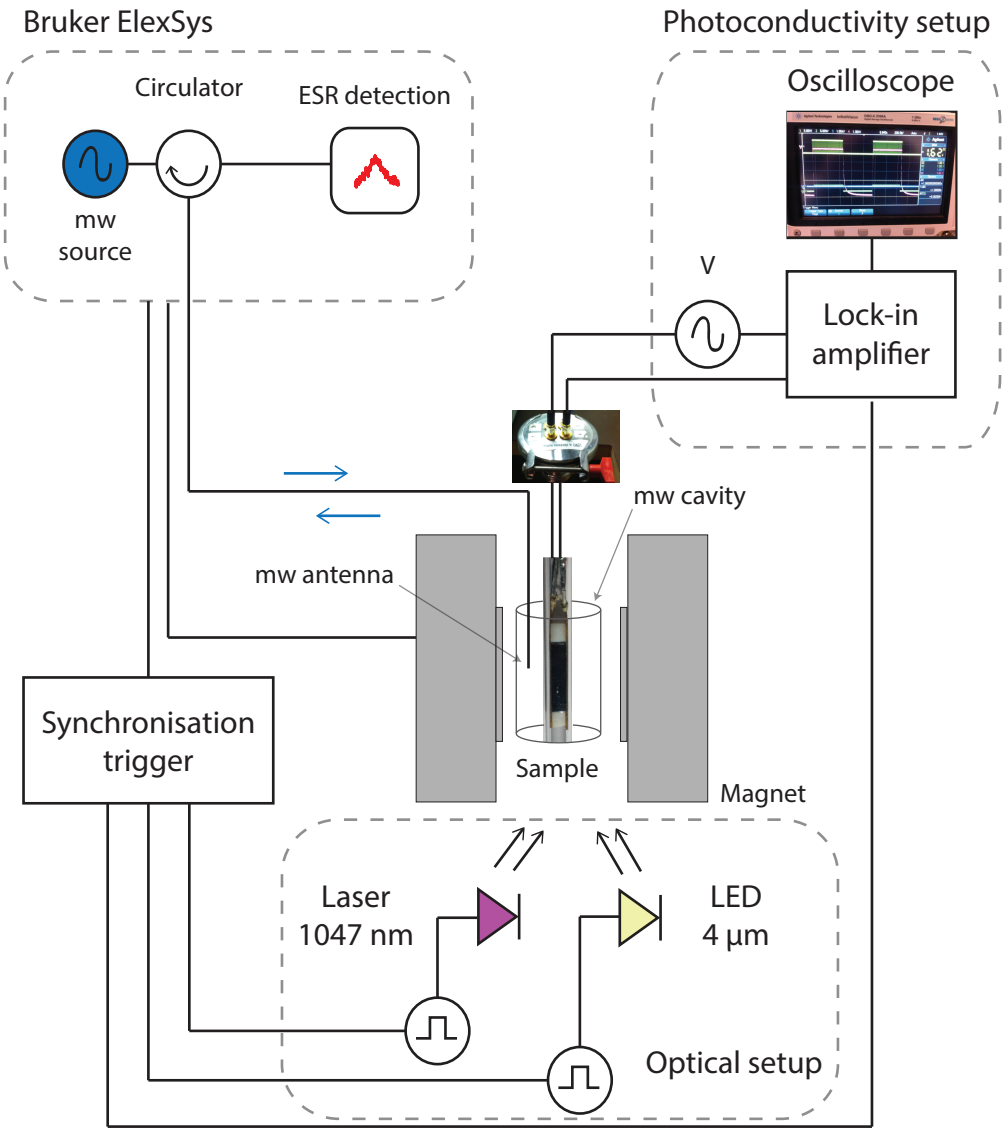


Figure 7.3.: **Schematic of the experimental setup used for the optical charge state manipulation of selenium:** Bruker Elexsys spectrometer at X-band (9.7 GHz) at University College London (UCL), where pulse-ESR is synchronised with the optical illumination.

7.3. A spin echo study of DA recombination dynamics

At a given temperature, the signal intensity of the spin echo is proportional to the number of singly-ionised selenium impurities Se^+. Therefore, we measure the spin echo intensity at different times δ after a laser pulse P at 1047 nm by using the sequence $(P - \delta - \pi/2 - \tau - \pi - \tau - \text{echo})$.

In order to obtain optimal experimental conditions, we chose to carry out the measurement at 15 K, where we have measured the electron spin relaxation T_1 and coherence T_2. Figure 7.4 shows the experimental decay of the integrated electron spin echo measured for T_1 (a) and T_2 (b). At this temperature, T_1 and T_2 are about 2 ms. We then set $\tau = 10\ \mu$s and a measurement rate of 10 Hz in order to allow enough time for electron spin relaxation.

In order to study the effect of free carriers, we measure the carrier life-time after illumination by photoconductivity (process (b) in Figure 7.1). At thermal equilibrium and low temperature, the concentration of free carriers in silicon can be neglected and the conductivity is proportional to the photo-induced carriers. After contacting the sample, we measure the photoconductivity via the electrical probe, as shown in Figure 7.3.

In Figure 7.5, we show the decay of the sample conductivity after a laser illumination for 1 s with a power of 100 mW. The setup used for this measurement is described in Section 7.2. The data in the Figure is fit with a bi-exponential decay obtaining a photo-induced carrier lifetime of 40 ms. After 0.1 s, 90% of the carriers are already re-neutralised.

ESR measurement of ionised selenium showed that a 1047 nm laser illumination at 100 mW and for about 1 s was sufficient to ensure zero initial spin echo signal.

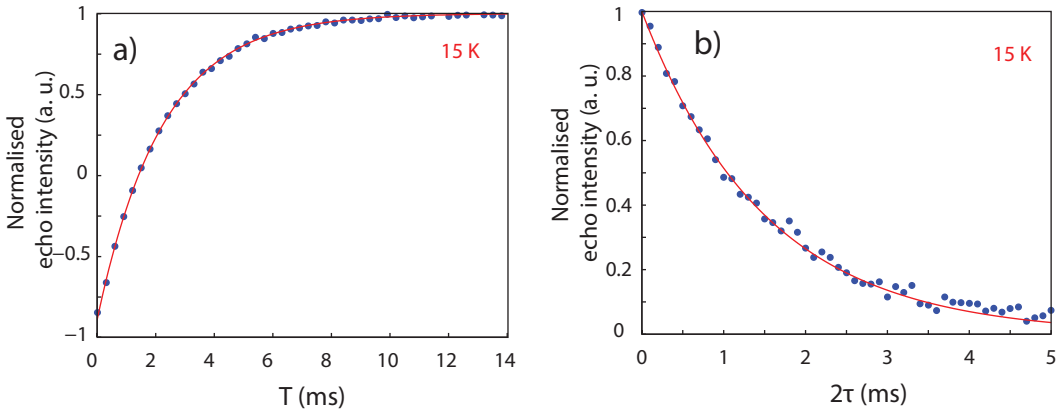


Figure 7.4.: **Experimental relaxation times of $^{77}Se^{+}$ at 15 K:** The pulse sequence used to measured T_1 (a) and T_2 (b) are described in Section 4.3.

Therefore, we assume that at this initial (non-equilibrium) condition, all donor and acceptors are neutralised ($\langle Se^{+}\rangle(\delta = 0) = 0$ and $\langle B^{-}\rangle(\delta = 0) = 0$).

The normalised spin echo signal measured at different times δ after the laser pulse and the relative pulse sequence are shown in Figure 7.6. The dynamics of this process corresponds to (c) in Figure 7.1. After ∼1000 seconds following the laser pulse, 60-70% of the echo intensity has recovered indicating that the majority of selenium-boron pairs has recombined. However, obtaining the full echo intensity required a waiting time of $\sim 10^4$ s, at which thermal equilibrium is re-established ($\langle Se^{+}\rangle \approx [B]$ and $\langle B^{-}\rangle \approx [B]$). The non-exponential behaviour is consistent with a random distribution of donor-acceptor nearest-neighbour distances.

An analytical expression to model the DA recombination dynamics is derived in Appendix B, for selenium doped silicon with low compensation. In this condition, the relative distance between donors and acceptors is much larger than the Bohr radius of both electron and hole bound to the impurities. Their wavefunctions in the ground state can be then considered unperturbed.

At the concentration used here, the most probable distance between DA nearest-

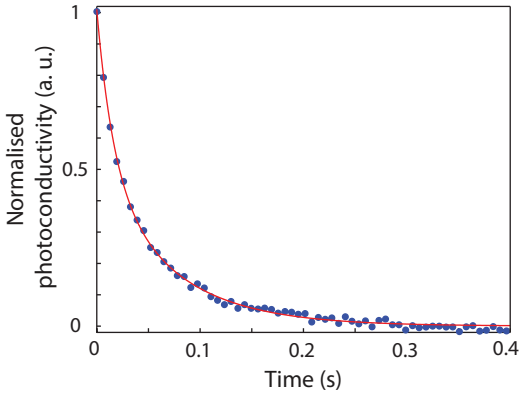


Figure 7.5.: **Measured carrier life-time after above band gap illumination at 15 K:** (a) An image of the oscilloscope directly measuring the photoconductivity of the sample. (b) Bi-exponential fit of the same data.

neighbours is about 50 nm which is much larger than $a_H^* = 4.2$ nm, the effective Bohr radius of the bound hole in silicon.

Under this approximation, the recombination rate (W) for each individual donor-acceptor (DA) pair is calculated to be proportional to the modulus squared of the optical matrix element between the donor and the acceptor in the neutral condition. We therefore obtain

$$W(r) = W_0 \exp\left\{-\frac{2r_{DA}}{a_H^*}\right\}, \tag{7.1}$$

where r_{DA} is the donor-acceptor distance separation and W_0 has been determined to be between 10^5 s^{-1} and 10^3 s^{-1} [DHW89].

Taking into consideration the effect of an ensemble of selenium impurities surrounding the acceptor, the dynamics can be shown to follow:

$$\frac{\langle \mathrm{B}^0(t)\rangle}{[\mathrm{B}]} = \exp\left[4\pi[\mathrm{Se}]\int_0^\infty \left\{e^{-W(r)t} - 1\right\}\, r^2 dr\right], \tag{7.2}$$

$$\frac{\langle \mathrm{Se}^+(t)\rangle}{[\mathrm{B}]} = 1 - \frac{\langle \mathrm{B}^0(t)\rangle}{[\mathrm{B}]} \tag{7.3}$$

where $\langle Se^{+}(t)\rangle$ and $\langle B^{0}(t)\rangle$ are the concentrations of Se^{+} and B^{-} respectively.

We simulate the dynamics of the recombination process using the Equations above, taking the known concentration of selenium impurities, and we find a good fit to the experimental data. The value of the relaxation rate W_0 used in the fit was 10^4 s^{-1}, at 15 K, which is consistent with previous values observed for similar samples doped with shallow donors [DHW89].

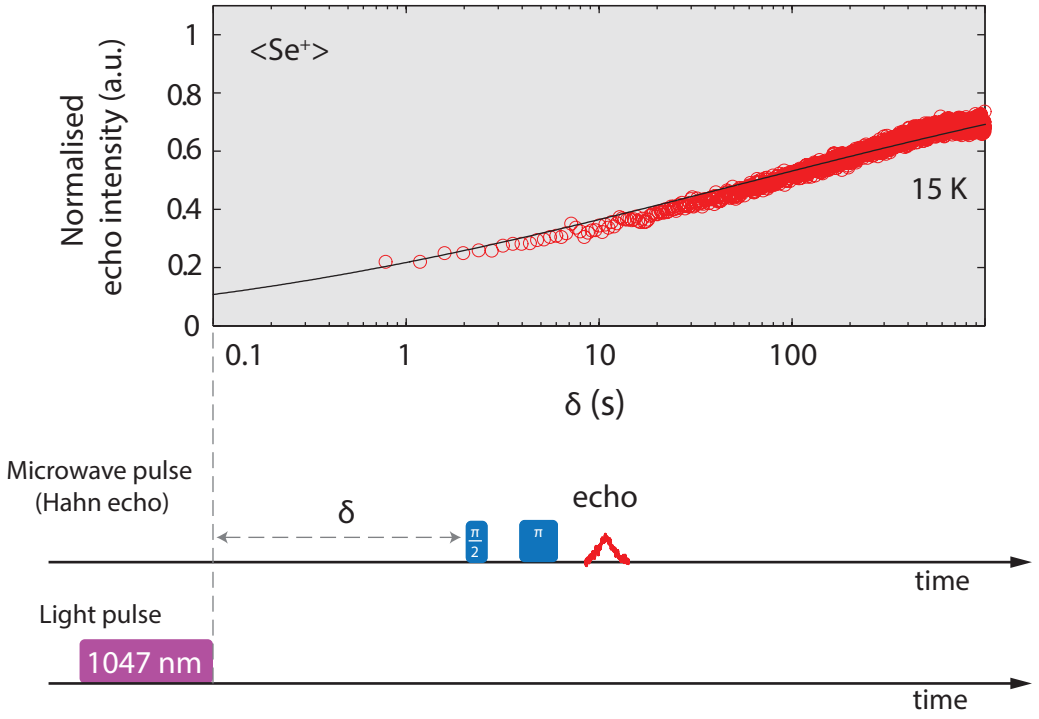


Figure 7.6.: Measured recombination dynamics after above band gap illumination: Normalised electron spin echo signal as a function of time δ from the illumination pulse P, measured at X-band ($B \sim 0.3$ mT) and at 15 K with $\tau = 10$ μs. Signal intensity of the spin echo is proportional to the concentration of singly-ionised selenium impurities Se^+ (red circle). Simulated dynamics of the recombination process is obtained using Equations 7.3, taking the known concentration of selenium impurities (black line). The value of the relaxation rate W_0 used in the fit was 10^4 s^{-1}.

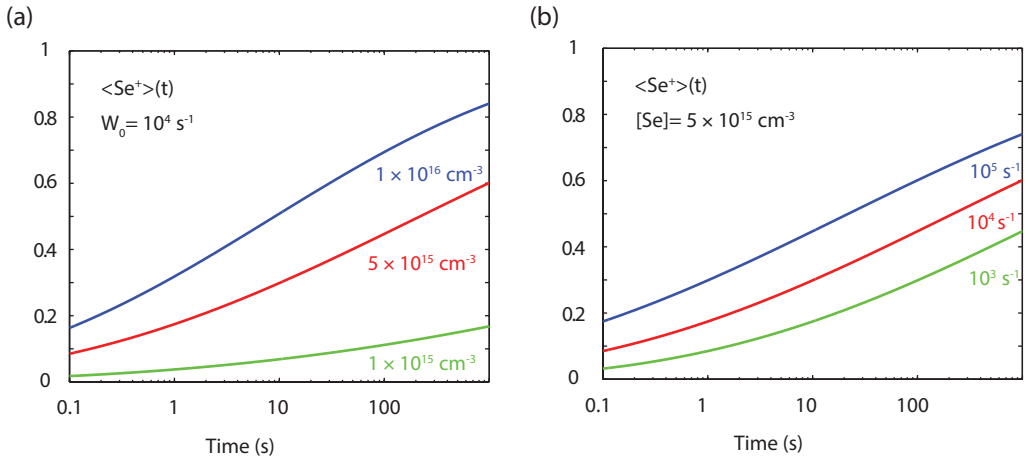


Figure 7.7.: **Solutions of the DA recombination dynamics for different values of W_0 and donors concentration:** (a) Ratio between the number of ionised selenium donors per unit volume as a function of time and its value at thermal equilibrium ($\langle Se^+(t)\rangle/\langle Se^+\rangle_{eq}$) for $W_0 = 10^4$ s and for different values of concentration as indicated. (b) $\langle Se^+(t)\rangle/\langle Se^+\rangle_{eq}$ for [Se]=5×10^{15} cm^{-3} and different values of W_0 as indicated.

In Figure 7.7, we give the results for the simulated DA recombination dynamics for different values of W_0 and donor concentrations. The simulation is obtained by Eq. 7.3 and the plot gives normalised concentrations of ionised selenium donors as a function of the time after the illumination pulse ($\langle Se^+(t)\rangle/\langle Se^+\rangle_{eq}$).

The donor-acceptor recombination time is strongly dependent on the concentration, as shown in Figure 7.7 (a). For instance, for a selenium concentration of 10^{16}cm^{-3} , about 80% of the donors recombine to thermal equilibrium after about 10^3 s. For a concentration ten times lower, the average distance decreases and the recombination rate is much lower then 20% recombined in the same time. However, for a given donor concentration, the dependence on the parameter W_0 does not affect the recombination as much.

The approach to thermal equilibrium can be accelerated over that resulting from DA pair recombination by optically ionising the neutral selenium. The ionisation

energy of neutral selenium (307 meV) corresponds to a wavelength of about 4 μm, as shown in Figure 3.2. At this infrared frequency, *low-cost* solid state LED sources are already available. The ionisation energy of group-V impurities, on the other hand, is much lower and the selective optical ionisation of donors requires a much higher frequencies. Under 4 μm optical illumination, an electron is continuously excited from the neutral selenium into the conduction band, whereupon it either returns to re-neutralise the selenium, or is captured by an acceptor (Figure 7.1 (d)).

We used a THORLABS LED4300P 4 μm LED (shown in Figure 7.2) to illuminate the sample, while measuring the concentration of ionised selenium, under the same conditions used before. The sequence used together with the experimental results are given in Figure 7.8. We find that under weak (10 μW) illumination at 4 μm, the rate at which equilibrium charge conditions are established is two orders of magnitude faster then the direct DA recombination. Within the first second after the 1047 nm flash, about 50 % of the echo signal is recovered and thermal equilibrium state is reached after about 100 s. The recombination is well fit by a bi-exponential decay with $\tau_1 = 1.6$ s and $\tau_2 = 40$ s. The effect of 4 μm illumination is further evidence that the slow observed recombination dynamic is limited by long-lived (i.e. distant) DA pairs. Moreover, the illumination sequence (1047 nm + 4 μm) could be used in order to study the nuclear spin properties of neutral selenium, $^{77}Se^0$, following analogous methods to those used to study ionised P nuclear spins through electrically detected magnetic resonance [DHSB12].

In shallow donors such as P, the hyperfine interaction with the electron spin strongly limits the nuclear spin coherence, such that nuclear spin coherence times for P^+ are strongly enhanced [SSS+13]. Similarly, one could expect the nuclear spin coherence time for neutral selenium (in its singlet ground state) to be comparably long.

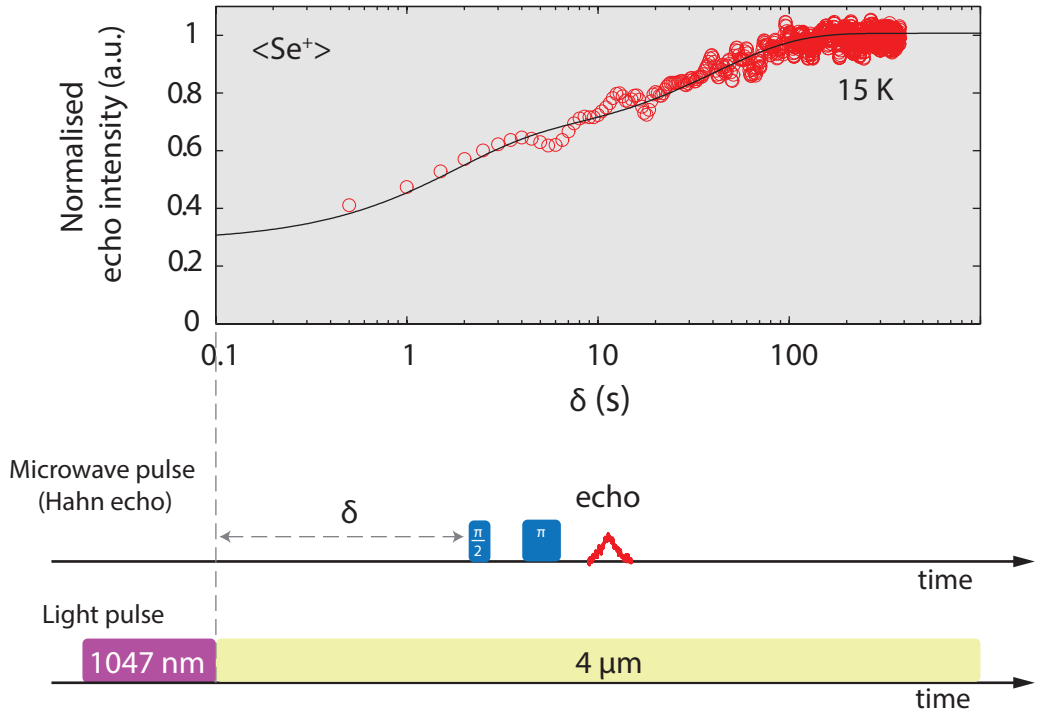


Figure 7.8.: Measured recombination dynamics after above band gap illumination and under 4 μm illumination: Normalised electron spin echo signal as a function of time δ from the illumination pulse P, measured at X-band ($B \sim 0.3$ mT) and at 15 K with $\tau = 10$ μs. Signal intensity of the spin echo is proportional to the concentration of singly-ionised selenium impurities Se^+ (red circle). Under 4 μm optical illumination, an electron is continuously excited from the neutral selenium into the conduction band, whereupon it either returns to re-neutralise the selenium, or is captured by an acceptor (Figure 7.1 (d)). The recombination is well fit by a bi-exponential decay with $\tau_1 = 1.6$ s and $\tau_2 = 40$ s (black line).

7.4. Conclusions

In conclusion, we have investigated optical methods to manipulate selenium charge state, examining this through donor-acceptor recombination following above band gap illumination. We have first measured the DA recombination dynamics of selenium in compensated silicon, demonstrating that this can be as long as 10^4 s at the concentration used here.

We also showed that neutral selenium impurities can be selectively ionised using 4 μm illumination. This suggests a possible mechanism to first bring selenium donors into an ESR-active Se^+ state, and to subsequently neutralise them leaving a potentially long-lived ^{77}Se nuclear spin. Future studies could exploit these methods to measure the nuclear spin coherence of neutral selenium donors.

CHAPTER 8

Conclusions

Research in the field of spin-based quantum computation in silicon has been attracting a growing attention in the last years. Despite impressive advances, such as single-spin control and read-out, much more has to be achieved in order to apply these remarkable results into the realisation of a quantum computer. Among these areas of future research, charge state control of donor has its importance, for example as a strategy to enhance nuclear spin coherence time. The work of this thesis was dedicated to explore electrical and optical strategies for charge state manipulation of donors in silicon.

In Chapter 5, we demonstrated electric field ionisation/recombination of arsenic donors in 28-silicon. We developed an SOI device with implanted arsenic donors

to be measured by ESR, under an electric field sufficiently strong to allow donor ionisation. We obtained a measure of the electric field necessary for ionisation of the arsenic donors with implications on how fast individual addressability of electron spins can be implemented. Moreover, the demonstration of the electric field ionisation/recombination of arsenic donors suggests that this method may be used to measure the nuclear spin coherence time of ionised donors. Future studies may investigate the electric field shift of the nuclear resonance and the nuclear spin coherence time of field ionised donors. However, the device measured in this Chapter has a signal intensity which is too weak to allow measurements of the nuclear spin state. In order to investigate the nuclear spin proprieties under electric field a different device design may improve the signal intensity. For example, increasing the thickness of the doped layer by an order of magnitude, we may increase the number of donors being still able to obtain an electric field strong enough to ionised them.

In Chapter 6, we initiated a study of a new class of donor spin qubit, Se^+ impurities in silicon. The results of this Chapter demonstrate that singly-ionised selenium has the longest electron spin relaxation time among donors in silicon, so far studied. However, we find that its electron and nuclear spin coherence times measured here are shorter than expected. The origin of this effect must be investigated further, but it is believed to be associated with the compensation of the material studied. In order to conclusively identify the sources of electron and nuclear spin decoherence mechanisms, a future study could investigate the Se and B concentration and compensation dependence of this effect.

Optical charge manipulation of selenium in silicon is demonstrated in Chapter 7, using light pulses at different wavelength. These results have been obtained thanks to one of the advantages of group-VI donors for applications in quantum computa-

tion: the larger ionisation energy of selenium, compared with the one of group-V donors, means their excited states can be driven using commercial light sources (as opposed to the THz sources needed to excite group-V donors).

Even though the results of this Chapter demonstrate that is possible to control optically the charge state of selenium donors, these processes are still difficult to control, relatively slow and inherently random. It may be also interesting to investigate the combined effect of electrical and optical methods for the charge state manipulation of group-VI donors.

In conclusion, the results presented in this thesis indicate that different donor spins in silicon still continue to present new proprieties that may be potentially advantageous for application in quantum information, such as the ability to place donors in different charge states.

APPENDIX A

The rotating frame

In Section 4.2, we have used the approximated Hamiltonian in Eq. 4.9, which is derived in this Appendix.

The spin state $|\psi\rangle$ in the rotating frame can be defined as

$$\left|\tilde{\psi}\right\rangle = U\left|\psi\right\rangle. \tag{A.1}$$

where U is the unitary operator in Eq. 4.7, which is

$$U = \exp\left(i\omega_e S_z t\right). \tag{A.2}$$

The Hamiltonian under this transformation can be derived substituting the transformed state $\left|\tilde{\psi}\right\rangle$ into the Schrödinger equation, given by

$$i\frac{d}{dt}\left|\psi\right\rangle = \mathcal{H}\left|\psi\right\rangle. \tag{A.3}$$

By inverting the definition of transformed state

$$\left|\psi\right\rangle = U^{\dagger}\left|\tilde{\psi}\right\rangle \tag{A.4}$$

and substituting in the Schrödinger equation we have

$$\omega_e S_z U^{\dagger}\left|\tilde{\psi}\right\rangle + iU^{\dagger}\frac{d}{dt}\left|\tilde{\psi}\right\rangle = \mathcal{H}U^{\dagger}\left|\tilde{\psi}\right\rangle \tag{A.5}$$

that can be re-written as

$$iU^{\dagger}\frac{d}{dt}\left|\tilde{\psi}\right\rangle = (\mathcal{H} - \omega_e S_z)U^{\dagger}\left|\tilde{\psi}\right\rangle \tag{A.6}$$

By multiplying both side of the equation with U, we obtain

$$i\frac{d}{dt}\left|\tilde{\psi}\right\rangle = \tilde{\mathcal{H}}\left|\tilde{\psi}\right\rangle \tag{A.7}$$

where we have defined

$$\tilde{\mathcal{H}} = U\left(\mathcal{H} - \omega_e S_z\right)U^{\dagger}. \tag{A.8}$$

If we substitute the explicit form of the Hamiltonian in Eq. 4.6 into Equation A.8, we obtain

$$\tilde{\mathcal{H}} = \Omega\cos(\omega_{\mathrm{mw}}t + \phi)US_xU^{\dagger}. \tag{A.9}$$

An explicit form of the Hamiltonian can be obtained by using the Baker-Hausdorff

formula, which for the Pauli matrixes is given by

$$e^{-i\alpha S_z} S_x e^{i\alpha S_z} = \cos(\alpha) S_x - i \sin(\alpha)[S_z, S_x] \tag{A.10}$$

Because we have $[S_z, S_x] = iS_y$, we therefore find that

$$\tilde{\mathcal{H}} = \Omega \cos(\omega_{\mathrm{mw}} t + \phi) \left[\cos(\omega_e t) S_x - \sin(\omega_e t) S_y\right]. \tag{A.11}$$

If we now chose $\omega_{\mathrm{mw}} = \omega_e$ and using the relations

$$\cos(\alpha) = \frac{1}{2}\left(e^{i\alpha} + e^{-i\alpha}\right) \tag{A.12}$$

$$\sin(\alpha) = \frac{1}{2i}\left(e^{i\alpha} - e^{-i\alpha}\right) \tag{A.13}$$

we obtain

$$\tilde{\mathcal{H}} = \frac{\Omega}{2}\left\{[\cos(\phi) + \cos(2\omega_e + \phi)] S_x - [\sin(2\omega_e + \phi) - \sin(\phi)] S_y\right\} \tag{A.14}$$

Finally, if we neglect the fast rotating terms ($2\omega_e$), so called *rotating wave approximation*, we obtain the Hamiltonian

$$\tilde{\mathcal{H}} \approx \frac{\Omega}{2}[\cos(\phi) S_x + \sin(\phi) S_y]. \tag{A.15}$$

APPENDIX B

Theory of DA recombination dynamics in selenium doped silicon

In Chapter 7, we measured the concentration of selenium impurity following above band-gap illumination. The recombination dynamics has been modelled using an analytical expression given by Equation 7.3 and valid for selenium doped silicon with low compensation. In this Appendix, we give a derivation of Equation 7.3, obtained for group-VI impurities in silicon and based on the approximations used in reference [THA65].

The approach used to obtain 7.3 is based on the calculation of the recombination rate of an isolated D-A pair as a function of the distance separation between the donor and the acceptor. The effect of the ensemble is then taken into account as a

set of independent recombination channels.

Rate of recombination of an isolated pair

Given a donor-acceptor pair at low temperature and out of thermal equilibrium (D^0A^0), the electron will naturally move from the donor to fill the acceptor level to re-establish thermal equilibrium (D^-A^+). The recombination rate (W) of this process will depend strongly on the distance r_{DA} between donor and acceptor.

The value of $W(r_{DA})$ can be taken to be proportional to the square module of the optical matrix element M between the wave functions of the donor and acceptor in the neutral condition ($W(r_{DA}) \propto |M|^2$). If the hole bound to the acceptor has a much lower ionisation energy than the electron bound to the donor and if we assume that the presence of an electron bound to the donor close by the acceptor does not modify much the hole wavefunction, the optical matrix element can be then considered to be proportional to the value of the hole wavefunction at the donor site

$$M(r) \propto \psi_H(r_{DA}). \tag{B.1}$$

This condition is largely satisfied for compensated selenium doped in silicon, having for Se^0 is $E_1 = 307$ meV and for boron $E_B \approx 50$ meV.

The ground state wavefunction of a hole bound to a Boron and calculated at the donor site, can be taken to be proportional to an hydrogen-like wavefunction such as

$$\psi_H(r_{DA}) \propto \exp\left\{-\frac{r_{DA}}{a_H}\right\} \tag{B.2}$$

where a_H is the effective Bohr radius of the hole, given by

$$a_H = \left[\frac{2m_H E_a}{\hbar^2}\right]^{\frac{1}{2}} \tag{B.3}$$

and m_H is the effective mass of the hole in silicon.

Therefore, the recombination rate of an Se^0B^0 isolated pair can be written as

$$W(r_{DA}) = W_0 \exp\left\{-\frac{2r_{DA}}{a_H}\right\} \tag{B.4}$$

where W_0 is a constant and the exponential contains the dependence on the donor-acceptor distance. The value of W_0 has be experimentally determined for group-V donor in silicon to be between 10^5 s^{-1} and 10^3 s^{-1} [DHW89].

Recombination dynamics for an ensemble in low compensation

The number of selenium impurities in the sample is given by

$$N_{\mathrm{Se}} = [\mathrm{Se}]\, V \tag{B.5}$$

where V is the volume of the crystal. All the N_{Se} donors interact with a given acceptor and contribute to the dynamics as N_{Se} independent recombination channels. Given a particular distance configuration of the donors surrounding the acceptor, the probability (Q) of the hole being bound to the acceptor (B^0) can be calculated by solving the differential equation

$$\frac{dQ}{dt} = -Q \sum_{i}^{N_{\mathrm{Se}}} W(r_i) \tag{B.6}$$

which gives the solution

$$Q(t) = \exp\left\{-\sum_{i}^{N_{\mathrm{Se}}} W(r_i)t\right\} \tag{B.7}$$

The number of acceptors in the neutral state is then obtained by multiplying Q to the concentration

$$\langle \mathrm{B}^0(t)\rangle = Q(t)[\mathrm{B}]. \tag{B.8}$$

The result given by Equation B.7 is valid for a given donors configuration. In order to extende this result for a random distribution, we need to multiply this results times the probability of having that given configuration and to sum over all configurations. Since each donor is randomly distributed, the probability of having a donor in the volume V is $1/V$ and we then have

$$\frac{\langle \mathrm{B}^0(t)\rangle}{[\mathrm{B}]} = \left(\frac{1}{V}\right)^{N_{\mathrm{Se}}} \int_V \int_V ... \int_V \exp\left\{-\sum_{i}^{N_{\mathrm{Se}}} W(r_i)t\right\}\ d^3r_1 ... d^3r_j ... d^3r_{N_{\mathrm{Se}}} \tag{B.9}$$

and we obtain

$$\frac{\langle \mathrm{B}^0(t)\rangle}{[\mathrm{B}]} = \left[\frac{1}{V}\int_V \exp\left\{-W(r)t\right\}\ d^3r\right]^{N_{\mathrm{Se}}}. \tag{B.10}$$

For $r \gg a_H$, $W(r)$ goes rapidly to zero and the exponential can be approximated as

$$\exp\left[-W(r)t\right] \approx 1 + \left\{\exp\left[-W(r)t\right] - 1\right\} \tag{B.11}$$

Moving into spherical coordinates and under the approximation B.11 we find that

$$\frac{\langle \mathrm{B}^0(t)\rangle}{[\mathrm{B}]} = \left[1 + \frac{4\pi}{V}\int_0^\infty \left\{\exp\left[-W(r)t\right] - 1\right\}\ r^2 dr\right]^{N_{\mathrm{Se}}} \tag{B.12}$$

and in the limit for $V \to 0$ we finally obtain

$$\frac{\langle \mathrm{B}^0(t)\rangle}{[\mathrm{B}]} = \exp\left[4\pi[\mathrm{Se}]\int_0^\infty \left\{\exp\left[-W(r)t\right] - 1\right\}\ r^2 dr\right]. \tag{B.13}$$

where we have $N_{\mathrm{Se}}/V = [\mathrm{Se}]$. Considering that we have

$$\frac{\langle \mathrm{B}^0(t)\rangle}{[\mathrm{B}]} = 1 - \frac{\langle \mathrm{B}^-(t)\rangle}{[\mathrm{B}]} \tag{B.14}$$

and

$$\langle \mathrm{Se}^+(t)\rangle = \langle \mathrm{B}^-(t)\rangle \tag{B.15}$$

we can rewrite the Equation B.13 for the selenium donors as

$$\frac{\langle \mathrm{Se}^+(t)\rangle}{[\mathrm{A}]} = 1 - \exp\left[4\pi[\mathrm{Se}]\int_0^\infty \left\{\exp\left[-W(r)t\right] - 1\right\}\ r^2 dr\right]. \tag{B.16}$$

Bibliography

[AAB+11] B. Andreas, Y. Azuma, G. Bartl, P. Becker, H. Bettin, M. Borys, I. Busch, M. Gray, P. Fuchs, K. Fujii, H. Fujimoto, E. Kessler, M. Krumrey, U. Kuetgens, N. Kuramoto, G. Mana, P. Manson, E. Massa, S. Mizushima, A. Nicolaus, A. Picard, A. Pramann, O. Rienitz, D. Schiel, S. Valkiers, and A. Waseda. Determination of the Avogadro Constant by Counting the Atoms in a 28Si Crystal. *Physical Review Letters*, 106(3):1–4, January 2011. pages 12

[ABD+13] D D Awschalom, L C Bassett, A S Dzurak, E L Hu, and J R Petta. Quantum Spintronics: Engineering and Manipulating Atom-Like Spins in Semiconductors. *Science*, 339:1174–1179, 2013. pages 2

[BAB+06] Simon C Benjamin, Arzhang Ardavan, G Andrew D Briggs, David a Britz, Daniel Gunlycke, John Jefferson, Mark a G Jones, David F Leigh, Brendon W Lovett, Andrei N Khlobystov, S a Lyon, John J L Morton, Kyriakos Porfyrakis, Mark R Sambrook, and Alexei M Tyryshkin. Towards a fullerene-based quantum computer. *Journal of Physics: Condensed Matter*, 18(21):S867–S883, May 2006. pages 8

[BTS+06] F. Bradbury, a. Tyryshkin, Guillaume Sabouret, Jeff Bokor, Thomas Schenkel, and S. Lyon. Stark Tuning of Donor Electron Spins in Silicon. *Physical Review Letters*, 97(17):1–4, October 2006. pages 18, 47, 78, 79, 81

[Cas63] T. G. Castner. Raman Spin-Lattice Relaxation of Shallow Donor in Silicon. *Physical Review*, 130:58–75, 1963. pages 50, 51, 52, 104, 105, 106

[Cas67] T. G. Castner. Orbach Spin-Lattice Relaxation of Shallow Donors in Silicon. *Physical Review*, 155(3):816, 1967. pages 11, 50, 51, 52, 104, 105

[Deu85] D Deutsch. No Title. *Phil. Trans. R. Soc. A*, 400:97, 1985. pages 1

[DHSB12] Lukas Dreher, Felix Hoehne, Martin Stutzmann, and Martin Brandt. Nuclear Spins of Ionized Phosphorus Donors in Silicon. *Physical Review Letters*, 108(2):027602, January 2012. pages 2, 3, 12, 67, 116, 128

[DHW89] P. Dirksen, A. Henstra, and W. Wenckebach. An electron spin echo study of donor-acceptor recombination. *J. Phys: Condens. Matter*, 7085(1):7085, 1989. pages 85, 118, 119, 124, 125, 141

[DiV95] DP DiVincenzo. Quantum computation. *Science*, 270(5234):255–261, 1995. pages 1

[EHvB+04] J. M. Elzerman, R. Hanson, L. H. W. van Beveren, B. Witkamp, L. M. K. Vandersypen, and L. P. Kouwenhoven. Single-shot read-out of an individual electron spin in a quantum dot. *Nature*, 430(July):431–435, 2004. pages 19

[FDT+09] G D Fuchs, V V Dobrovitski, D M Toyli, F J Heremans, and D D Awschalom. Gigahertz dynamics of a strongly driven single quantum spin. *Science (New York, N.Y.)*, 326(5959):1520–2, December 2009. pages 9

[Feh59] G. Feher. Electron spin resonance experiments on donors in silicon. *Physical Review*, 114:129–1244, 1959. pages 10, 11, 41, 76

[FMM+12] Martin Fuechsle, Jill a Miwa, Suddhasatta Mahapatra, Hoon Ryu, Sunhee Lee, Oliver Warschkow, Lloyd C L Hollenberg, Gerhard Klimeck, and Michelle Y Simmons. A single-atom transistor. *Nature nanotechnology*, 7(4):242–6, April 2012. pages 16, 17, 21

[FMZ+10] Martin Fuechsle, S Mahapatra, F a Zwanenburg, Mark Friesen, M a Eriksson, and Michelle Y Simmons. Spectroscopy of few-electron single-crystal silicon quantum dots. *Nature nanotechnology*, 5(7):502–5, July 2010. pages 16, 17

[FYPM54] R. C. Fletcher, W. A. Yager, G. L. Pearson, and F. R. Merritt. Hyperfine Splitting in Spin Resonance of Group V Donors in Silicon. *Physical Review*, 95:844, 1954. pages 41

[GB58] J P Gordon and K D Bowers. Microwave Spin Echoes from Donor Electrons in Silicon. *Phys. Rev. Lett.*, 1(10):368–370, November 1958. pages 9, 11

[GJE+81] H. G. Grimmeiss, E. JanzeÌĄn, H Ennen, O Schirmer, J Schneider, R Worner, C Holm, E Sirtl, and P Wagner. Tellurium donors in Silicon. *Physical Review B*, 24(8):4571, 1981. pages 27, 30, 41, 97

[GJL82] H. G. Grimmeiss, E. JanzeÌĄn, and K. Larsson. Multivalley spin splitting of ls states for sulfur, selenium, and tellurium donors in silicon. *Physical Review B*, 25(4):2627, 1982. pages 3, 27, 29

[GJS80] H. G. Grimmeiss, E. JanzeÌĄn, and B. Skarstam. Electronic properties of selenium-doped silicon. *Journal of Applied Physics*, 51(7):3740, 1980. pages 27

[GWR+10] Richard George, Wayne Witzel, H. Riemann, N. Abrosimov, N. Nötzel, Mike Thewalt, and John J. L. Morton. Electron Spin Coherence and Electron Nuclear Double Resonance of Bi Donors in Natural Si. *Physical Review Letters*, 105(6):067601, August 2010. pages 10, 11

[HAGD00] P. Huy, C. Ammerlaan, T. Gregorkiewicz, and D. Don. Hydrogen passivation of the selenium double donor in silicon:âĂĆA study by magnetic resonance. *Physical Review B*, 61(11):7448–7458, March 2000. pages 27, 97, 103

[HS60] A Honig and E Stupp. Electron Spin-Lattice Relaxation in Phosphorus-Doped Silicon. *Physical Review*, 117:69, 1960. pages 50, 107

[HSM06] J. Harrison, M.J. Sellars, and N.B. Manson. Measurement of the optically induced spin polarisation of N-V centres in diamond. *Diamond and Related Materials*, 15(4-8):586–588, April 2006. pages 8

[Igo66] T Igo. Spin-Lattice Relaxation in Compensated n-Type Silicon. *Journal of the Physical Society of Japan*, 21:874, 1966. pages 50

[JSGG84] E Janzen, R Stedman, G Grossmann, and H G Grimmeiss. High-resolution studies of sulfur- and selenium-related donor center in silicon. *Physical Review B*, 29(4):1904, 1984. pages 27, 28, 29, 91, 97

[JYH+05] D. N. Jamieson, C. Yang, T. Hopf, S. M. Hearne, C. I. Pakes, S. Prawer, M. Mitic, E. Gauja, S. E. Andresen, F. E. Hudson, a. S. Dzurak, and R. G. Clark. Controlled shallow single-ion implantation in silicon using an active substrate for sub-20-keV ions. *Applied Physics Letters*, 86(20):202101, 2005. pages 15

[Kan98] BE Kane. A silicon-based nuclear spin quantum computer. *Nature*, 393:133–137, 1998. pages 3, 14, 18, 19, 67, 82, 88

[KMD+00] B. Kane, N. McAlpine, A. Dzurak, R. Clark, G. Milburn, H. Sun, and H. Wiseman. Single-spin measurement using single-electron transistors to probe two-electron systems. *Physical Review B*, 61(4):2961–2972, January 2000. pages 2, 89, 107

[KOB+10] Y. Kubo, F. Ong, P. Bertet, D. Vion, V. Jacques, D. Zheng, a. Dréau, J.-F. Roch, a. Auffeves, F. Jelezko, J. Wrachtrup, M. Barthe, P. Bergonzo, and D. Esteve. Strong Coupling of a Spin Ensemble to a Superconducting Resonator. *Physical Review Letters*, 105(14):1–4, September 2010. pages 20

[KTR+01] D. Karaiskaj, M. Thewalt, T. Ruf, M. Cardona, H.-J. Pohl, G. Deviatych, P. Sennikov, and H. Riemann. Photoluminescence of Isotopically Purified Silicon: How Sharp are Bound Exciton Transitions? *Physical Review Letters*, 86(26):6010–6013, June 2001. pages 12

[KYK00] M. Koizuka and H. Yamada-Kaneta. Electron spin resonance centers associated with oxygen precipitates in Czochralski silicon crystals. *Journal of Applied Physics*, 88(4):1784, 2000. pages 76

[LBS+07] C. Lo, J. Bokor, T. Schenkel, a. M. Tyryshkin, and S. a. Lyon. Spin-dependent scattering off neutral antimony donors in [sup 28]Si field-effect transistors. *Applied Physics Letters*, 91(24):242106, 2007. pages 11

[LFKV00] A A Larionov, L E Fedichkin, A A Kokin, and K A Valiev. The nuclear magnetic resonance spectrum of 31 P donors in a silicon. *Nanotechnology*, 392(11), 2000. pages 18, 47

[LJL+10] T D Ladd, F Jelezko, R Laflamme, Y Nakamura, C Monroe, and J L O'Brien. Quantum computers. *Nature*, 464(7285):45–53, March 2010. pages 1

[LLG+11] C. Lo, V. Lang, R. George, J. Morton, a. Tyryshkin, S. Lyon, J. Bokor, and T. Schenkel. Electrically Detected Magnetic Resonance of Neutral Donors Interacting with a Two-Dimensional Electron Gas. *Physical Review Letters*, 106(20):1–4, May 2011. pages 11

[LPD+09] Cheuk Chi Lo, Arun Persaud, Scott Dhuey, Deirdre Olynick, Ferenc Borondics, Michael C Martin, Hans a Bechtel, Jeffrey Bokor, and Thomas Schenkel. Device fabrication and transport measurements of FinFETs built with 28 Si SOI wafers toward donor qubits in silicon. *Semiconductor Science and Technology*, 24(10):105022, October 2009. pages 16

[LRW+08] G. P. Lansbergen, R. Rahman, C. J. Wellard, I. Woo, J. Caro, N. Collaert, S. Biesemans, G. Klimeck, L. C. L. Hollenberg, and S. Rogge. Gate-induced quantum-confinement transition of a single dopant atom in a siliconÂăFinFET. *Nature Physics*, 4(8):656–661, June 2008. pages 16

[LSH+94] J. W. Lyding, T.-C. Shen, J. S. Hubacek, J. R. Tucker, and G. C. Abeln. Nanoscale patterning and oxidation of H-passivated Si(100)-2ÃŮ1 surfaces with an ultrahigh vacuum scanning tunneling microscope. *Applied Physics Letters*, 64(15):2010, 1994. pages 17

[LSL+14] C C Lo, S Simmons, R Lo Nardo, C D Weis, A M Tyryshkin, J Meijer, D Rogalla, S A Lyon, J Bokor, T Schenkel, and J. J. L. Morton. Stark shift and field ionization of arsenic donors in 28 Si-silicon-on-insulator structures. *Applied Physics Letters*, 104:193502, 2014. pages 68

[Lud65] G. W. Ludwig. Paramagnetic Resonance Study of a Deep Donor in Silicon. *Physical Review*, 137(5A):1520, 1965. pages 50, 91, 106

[LWS+15] Roberto Lo Nardo, Gary Wolfowicz, Stephanie Simmons, Alexei M. Tyryshkin, Helge Riemann, Nikolai V. Abrosimov, Peter Becker, Hans-Joachim Pohl, Michael Steger, Stephen A. Lyon, Mike L. W. Thewalt, and John J. L. Morton. Spin relaxation and donor-acceptor recombination of Se+ in 28-silicon. *arXiv: 1503.05811*, March 2015. pages 90, 116

[MBKK05] a. Martins, Timothy Boykin, Gerhard Klimeck, and Belita Koiller. Conduction-band tight-binding description for Si applied to P donors. *Physical Review B*, 72(19):3–6, November 2005. pages 18, 47

[MCK04] a. Martins, R. Capaz, and Belita Koiller. Electric-field control and adiabatic evolution of shallow donor impurities in silicon. *Physical Review B*, 69(8):1–7, February 2004. pages 18, 47

[MDL+14] Juha T Muhonen, Juan P Dehollain, Arne Laucht, Fay E Hudson, Rachpon Kalra, Takeharu Sekiguchi, Kohei M Itoh, David N Jamieson, Jeffrey C McCallum, Andrew S Dzurak, and Andrea Morello. Storing quantum information for 30 seconds in a nanoelectronic device. *Nature nanotechnology*, 9(October), October 2014. pages 10

[MEH+09] a. Morello, C. Escott, H. Huebl, L. Willems van Beveren, L. Hollenberg, D. Jamieson, a. Dzurak, and R. Clark. Architecture for high-sensitivity single-shot readout and control of the electron spin of individual donors in silicon. *Physical Review B*, 80(8):1–4, August 2009. pages 10

[MMEL11] John J L Morton, Dane R McCamey, Mark A Eriksson, and Stephen A Lyon. Embracing the quantum limit in silicon computing. *Nature*, 479(7373):345–53, November 2011. pages 2, 10

[MMS+08] G. Morley, D. McCamey, H. Seipel, L.-C. Brunel, J. van Tol, and C. Boehme. Long-Lived Spin Coherence in Silicon with an Electrical Spin Trap Readout. *Physical Review Letters*, 101(20):3–6, November 2008. pages 10

[Mor09] John J L Morton. A silicon-based cluster state quantum computer. *arXiv:0905.4008v1*, 2009. pages 14

[MPZ+10] Andrea Morello, Jarryd J Pla, Floris A Zwanenburg, Kok W Chan, Kuan Y Tan, Hans Huebl, Mikko Möttönen, Christopher D Nugroho, Changyi Yang, Jessica A van Donkelaar, Andrew D C Alves, David N Jamieson, Christopher C Escott, Lloyd C L Hollenberg, Robert G Clark, and Andrew S Dzurak. Single-shot readout of an electron spin in silicon. *Nature*, 467(7316):687–91, October 2010. pages 2, 19, 20, 83, 88

[MTA+05a] John J L Morton, Alexei Tyryshkin, Arzhang Ardavan, Kyriakos Porfyrakis, S. Lyon, and G. Briggs. High Fidelity Single Qubit Operations Using Pulsed Electron Paramagnetic Resonance. *Physical Review Letters*, 95(20):1–4, November 2005. pages 9

[MTA+05b] John J. L. Morton, Alexei M. Tyryshkin, Arzhang Ardavan, Simon C. Benjamin, Kyriakos Porfyrakis, S. a. Lyon, and G. Andrew D. Briggs. BangâĂŞbang control of fullerene qubits using ultrafast phase gates. *Nature Physics*, 2(1):40–43, December 2005. pages 8

[MTB+08] John J. L. Morton, Alexei M. Tyryshkin, Richard M. Brown, Shyam Shankar, Brendon W. Lovett, Arzhang Ardavan, Thomas Schenkel, Eugene E. Haller, Joel W. Ager, and S. a. Lyon. Solid-state quantum memory using the 31P nuclear spin. *Nature*, 455(7216):1085–1088, October 2008. pages 8, 11, 12, 21, 110

[MVMB10] D R McCamey, J Van Tol, G W Morley, and C Boehme. Electronic spin storage in an electrically readable nuclear spin memory with a lifetime >100 seconds. *Science (New York, N.Y.)*, 330(6011):1652–6, December 2010. pages 10, 83

[MWS+10] Gavin W Morley, Marc Warner, a Marshall Stoneham, P Thornton Greenland, Johan van Tol, Christopher W M Kay, and Gabriel Aeppli. The initialization and manipulation of quantum information stored in silicon by bismuth dopants. *Nature materials*, 9(9):725–729, September 2010. pages 10

[NKNV07] K C Nowack, F H L Koppens, Yu V Nazarov, and L M K Vandersypen. Coherent control of a single electron spin with electric fields. *Science (New York, N.Y.)*, 318(5855):1430–3, November 2007. pages 8

[Orb61] R Orbach. On the theory of spin-lattice relaxation in paramagnetic salts. *Proc. Phys. Soc.*, 77:821, 1961. pages 11, 51, 104

[PMSH88] R. E. Peale, K. Muro, A. J. Sievers, and F. S. Ham. Zeeman splitting of double-donor spin-triplet levels in silicon. *Physical Review B*, 37:10829, 1988. pages 27

[PTD+12] Jarryd J Pla, Kuan Yen Tan, Juan P Dehollain, W H Lim, John J L Morton, David N Jemieson, Andrew S Dzurak, and Andrea Morello. A single-atom electron spin qubit in silicon. *Nature*, 489:541–545, 2012. pages 2, 21, 83, 88

[PTD+13] Jarryd J Pla, Kuan Y Tan, Juan P Dehollain, Wee H Lim, John J L Morton, Floris A Zwanenburg, David N Jamieson, Andrew S Dzurak, and Andrea Morello. High-fidelity readout and control of a nuclear spin qubit in silicon. *Nature*, 496(7445):334–8, April 2013. pages 2, 83, 88

[PWU+14] Giuseppe Pica, Gary Wolfowicz, Matias Urdampilleta, Mike L. W. Thewalt, Helge Riemann, Nikolai V. Abrosimov, Peter Becker, Hans-Joachim Pohl, John J. L. Morton, R. N. Bhatt, S. A. Lyon, and Brendon W. Lovett. Hyperfine Stark effect of shallow donors in silicon. *Physical Review B*, 90(19):195204, November 2014. pages 18, 25, 42, 47, 49, 69, 78, 84, 107, 113, 114

[RDFV+12] B. Roche, E. Dupont-Ferrier, B. Voisin, M. Cobian, X. Jehl, R. Wacquez, M. Vinet, Y.-M. Niquet, and M. Sanquer. Detection of a Large Valley-Orbit Splitting in Silicon with Two-Donor Spectroscopy. *Physical Review Letters*, 108(20):18–22, May 2012. pages 16

[ROG+05] F J Ruess, L Oberbeck, K E J Goh, M J Butcher, E Gauja, a R Hamilton, and M Y Simmons. The use of etched registration markers to make four-terminal electrical contacts to STM-patterned nanostructures. *Nanotechnology*, 16(10):2446–2449, October 2005. pages 17

[ROS+04] Frank J Ruess, Lars Oberbeck, Michelle Y Simmons, Kuan Eng J Goh, Alex R Hamilton, Toby Hallam, Steven R Schofield, Neil J Curson, and Robert G Clark. Toward Atomic-Scale Device Fabrication in Silicon Using Scanning Probe Microscopy. *Nano Letters*, 4(10):1969, 2004. pages 17

[RWB+07] Rajib Rahman, Cameron Wellard, Forrest Bradbury, Marta Prada, Jared Cole, Gerhard Klimeck, and Lloyd Hollenberg. High Precision Quantum Control of Single Donor Spins in Silicon. *Physical Review Letters*, 99(3):3–6, July 2007. pages 18, 47, 78, 81

[SBCC08] J. a. Seamons, E. Bielejec, M. S. Carroll, and K. D. Childs. Room temperature single ion detection with Geiger mode avalanche diode detectors. *Applied Physics Letters*, 93(4):043124, 2008. pages 15

[SBH+06] Andre R. Stegner, Christoph Boehme, Hans Huebl, Martin Stutzmann, Klaus Lips, and Martin S. Brandt. Electrical detection of coherent 31P spin quantum states. *Nature Physics*, 2(12):835–838, November 2006. pages 115

[SBR+11] Stephanie Simmons, Richard M Brown, Helge Riemann, Nikolai V Abrosimov, Peter Becker, Hans-Joachim Pohl, Mike L W Thewalt, Kohei M Itoh, and John J L Morton. Entanglement in a solid-state spin ensemble. *Nature*, 470(7332):69–72, February 2011. pages 12

[SDK03] A. Skinner, M. Davenport, and B. Kane. Hydrogenic Spin Quantum Computing in Silicon: A Digital Approach. *Physical Review Letters*, 90(8):087901, February 2003. pages 14, 20

[Shr83] K N Shriyastava. Theory of Spin-Lattice Relaxation. *Physica Status Solidi (b)*, 117:437, 1983. pages 50

[SJ01] Arthur Schweiger and Gunnar Jeschke. *Principles of Pulse Electron Paramagnetic Resonance*. Oxford University Press, 2001. pages 52, 55, 108, 109

[SLP+06] T. Schenkel, J. a. Liddle, a. Persaud, a. M. Tyryshkin, S. a. Lyon, R. de Sousa, K. B. Whaley, J. Bokor, J. Shangkuan, and I. Chakarov. Electrical activation and electron spin coherence of ultralow dose antimony implants in silicon. *Applied Physics Letters*, 88(11):112101, 2006. pages 10

[SLT80] J C Swartz, D H Lemmon, and R N Thomas. Optical Excitation Spectra of Selenium-doped Silicon. *Solid State Commun.*, 36:331, 1980. pages 27, 28

[SLW+11] Thomas Schenkel, Cheuk Chi Lo, C. D. Weis, J. Bokor, Alexei M. Tyryshkin, and Stephen A. Lyon. A spin quantum bit architecture with coupled donors and quantum dots in silicon. *arXiv:1110.2228v1*, 2011. pages 14, 20

[SPP+03] T. Schenkel, a. Persaud, S. J. Park, J. Nilsson, J. Bokor, J. a. Liddle, R. Keller, D. H. Schneider, D. W. Cheng, and D. E. Humphries. Solid state quantum computer development in silicon with single ion implantation. *Journal of Applied Physics*, 94(11):7017, 2003. pages 15

[SPV+11] C. Simmons, J. Prance, B. Van Bael, Teck Koh, Zhan Shi, D. Savage, M. Lagally, R. Joynt, Mark Friesen, S. Coppersmith, and M. Eriksson. Tunable Spin Loading and T_{1} of a Silicon Spin Qubit Measured by Single-Shot Readout. *Physical Review Letters*, 106(15):1–4, April 2011. pages 10

[SSS+13] K. Saeedi, S. Simmons, J. Z. Salvail, P. Dluhy, H. Riemann, N. V. Abrosimov, P. Becker, H.-J. Pohl, J. J. L. Morton, and M. L. W. Thewalt. Room-Temperature Quantum Bit Storage Exceeding 39 Minutes Using Ionized Donors in Silicon-28. *Science*, 342(6160):830–833, November 2013. pages 2, 3, 10, 13, 21, 67, 128

[SST+12] M Steger, K Saeedi, M L W Thewalt, J J L Morton, H Riemann, N V Abrosimov, P Becker, and H-J Pohl. Quantum information storage for over 180 s using donor spins in a 28Si "semiconductor vacuum". *Science (New York, N.Y.)*, 336(6086):1280–1283, June 2012. pages 10

[SSY+11] M. Steger, T. Sekiguchi, a. Yang, K. Saeedi, M. E. Hayden, M. L. W. Thewalt, K. M. Itoh, H. Riemann, N. V. Abrosimov, P. Becker, and H.-J. Pohl. Optically-detected NMR of optically-hyperpolarized 31P neutral donors in 28Si. *Journal of Applied Physics*, 109(10):102411, 2011. pages 13

[Sug63] K Sugihara. Spin-Lattice Relaxation of Shallow Donors in Heavily Doped Si. *Journal of the Physical Society of Japan*, 18:961, 1963. pages 50, 106

[SYT+09] M. Steger, A. Yang, M. Thewalt, M. Cardona, H. Riemann, N. Abrosimov, M. Churbanov, A. Gusev, A. Bulanov, I. Kovalev, A. Kaliteevskii, O. Godisov, P. Becker, H. J. Pohl, E. Haller, and J. Ager. High-resolution absorption spectroscopy of the deep impurities S and Se in 28Si revealing the 77Se hyperfine splitting. *Physical Review B*, 80(11):115204, September 2009. pages 27, 29, 30, 31, 91

[TCM+10] Kuan Yen Tan, Kok Wai Chan, Mikko Möttönen, Andrea Morello, Changyi Yang, Jessica van Donkelaar, Andrew Alves, Juha-Matti Pirkkalainen, David N Jamieson, Robert G Clark, and Andrew S Dzurak. Transport spectroscopy of single phosphorus donors in a silicon nanoscale transistor. *Nano letters*, 10(1):11–5, January 2010. pages 15, 16

[THA65] D. G. Thomas, J. J. Hopfield, and W. M. Augustyniak. Kinetics of Radiative Recombination at Ramdomly Distributed Donor and Acceptors. *Physical Review*, 140(1A):202, 1965. pages 118, 139

[TLAR03] A. Tyryshkin, S. Lyon, A. Astashkin, and A. Raitsimring. Electron spin relaxation times of phosphorus donors in silicon. *Physical Review B*, 68(19):193207, November 2003. pages 10, 11, 41, 115

[TML+10] Michiharu Tabe, Daniel Moraru, Maciej Ligowski, Miftahul Anwar, Ryszard Jablonski, Yukinori Ono, and Takeshi Mizuno. Single-Electron Transport through Single Dopants in a Dopant-Rich Environment. *Physical Review Letters*, 105(1):1–4, July 2010. pages 16

[TTM+12] Alexei M Tyryshkin, Shinichi Tojo, John J L Morton, Helge Riemann, Nikolai V Abrosimov, Peter Becker, Hans-Joachim Pohl, Thomas Schenkel, Michael L W Thewalt, Kohei M Itoh, and S A Lyon. Electron spin coherence exceeding seconds in high-purity silicon. *Nature Materials*, 11(2):143–7, February 2012. pages 9, 11, 52, 53, 54, 76, 108, 109

[Wil68] F. Williams. DonorâĂŤacceptor pairs in semiconductors. *Physica Status Solidi (b)*, 25(2):493–512, 1968. pages 106

[WST+12a] Gary Wolfowicz, Stephanie Simmons, Alexei M Tyryshkin, Richard E. George, Helge Riemann, Nikolai V Abrosimov, Peter Becker, Hans-Joachim Pohl, Stephen A Lyon, Mike L W Thewalt, and John J L Morton. Decoherence mechanisms of 209Bi donor electron spins in isotopically pure 28Si. *arXiv: 1207.3776*, July 2012. pages 10, 11, 12

[WST+12b] Gary Wolfowicz, Stephanie Simmons, Alexei M. Tyryshkin, Richard E. George, Helge Riemann, Nikolai V. Abrosimov, Peter Becker, Hans-Joachim Pohl, Stephen A. Lyon, Mike L. W. Thewalt, and John J. L. Morton. Decoherence mechanisms of ˆ{209}Bi donor electron spins in isotopically pure ˆ{28}Si. *Physical Review B*, 86(24):245301, December 2012. pages 41, 52, 106, 108

[WTG+13] Gary Wolfowicz, Alexei M Tyryshkin, Richard E George, Helge Riemann, Nikolai V Abrosimov, Peter Becker, Hans-Joachim Pohl, Mike L W Thewalt, Stephen A Lyon, and John J L Morton. Atomic clock transitions in silicon-based spin qubits. *Nature Nanotechnology*, 8(8):561–4, August 2013. pages 2, 10, 52

[WUT+14] Gary Wolfowicz, Matias Urdampilleta, Mike L.âĂŁW. Thewalt, Helge Riemann, Nikolai V. Abrosimov, Peter Becker, Hans-Joachim Pohl, and John J.âĂŁL. Morton. Conditional Control of Donor Nuclear Spins in Silicon Using Stark Shifts. *Physical Review Letters*, 113(15):157601, October 2014. pages 112

[XHJ10] M. Xiao, M. G. House, and H. W. Jiang. Measurement of the Spin Relaxation Time of Single Electrons in a Silicon Metal-Oxide-Semiconductor-Based Quantum Dot. *Physical Review Letters*, 104(9):096801, March 2010. pages 10

[YH68] G. Yang and A. Honig. Concentration- and Compensation-Dependent Spin-Lattice Relaxation in n-Type Silicon. *Physical Review*, 168:271, 1968. pages 50, 104, 106

[YSK+06] A. Yang, M. Steger, D. Karaiskaj, M. Thewalt, M. Cardona, K. Itoh, H. Riemann, N. Abrosimov, M. Churbanov, A. Gusev, A. Bulanov, A. Kaliteevskii, O. Godisov, P. Becker, H.-J. Pohl, J. Ager, and E. Haller. Optical Detection and Ionization of Donors in Specific Electronic and Nuclear Spin States. *Physical Review Letters*, 97(22):227401, November 2006. pages 12

[YSS+09] A. Yang, M. Steger, T. Sekiguchi, M. Thewalt, T. Ladd, K. Itoh, H. Riemann, N. Abrosimov, P. Becker, and H.-J. Pohl. Simultaneous Subsecond Hyperpolarization of the Nuclear and Electron Spins of Phosphorus

in Silicon by Optical Pumping of Exciton Transitions. *Physical Review Letters*, 102(25):257401, June 2009. pages 13

[Zav45] E Zavoisky. Paramagnetic relaxation of siquid for perpendicular field. *J. Phys. USSR*, 9:211, 1945. pages 55